

國立交通大學

電機與控制工程學系

博士論文

運用決策樹於腦部核磁共振影像之監督式腦組織分割研究

A Supervised Segmentation of Brain MRI Tissue Using Decision Trees

研究生：趙文鴻

指導教授：陳右穎 博士

中華民國九十七年九月

運用決策樹於腦部核磁共振影像之監督式腦組織分割研究

A Supervised Segmentation of Brain MRI Tissue Using Decision Trees

研究生：趙文鴻

Student : Wen-Hung Chao

指導教授：陳右穎 博士

Advisor : Dr. You-Yin Chen

國立交通大學

電機與控制工程學系

博士論文

A Dissertation

Submitted to Department of Electrical and Control Engineering

College of Electrical Engineering

National Chiao Tung University

in partial Fulfillment of the Requirements

for the Degree of

Doctor of Philosophy

in

Electrical and Control Engineering

September 2008

Hsinchu, Taiwan, Republic of China

中華民國九十七年九月

# 運用決策樹於腦部核磁共振影像之監督式腦組織分割研究

學生：趙文鴻

指導教授：陳右穎 博士

國立交通大學電機與控制工程學系 博士班

## 摘 要

本文研究之目的主要是運用決策樹以增進腦部核磁共振影像於組織分割的準確度達到一個高品質的腦部組織分割為目標，首先，此研究提出用一個多階層仿視覺 (Multiscale retinex) 演算法來校準核磁共振影像之不均勻度 (Inhomogeneity)，此實驗之核磁共振影像含有假體核磁共振影像與老鼠之腦部核磁共振影像，經此演算法校準後可獲得較好的影像品質與清晰的深層腦部結構影像，此外也用訊號峰值對雜訊比 (Peak-signal-to-noise) 與 (Contrast-to-noise) 對比度對雜訊比來評估校準後的影像品質。進一步實驗為得到腦部不同組織解剖結構，我們提出用分類與迴歸決策樹 (CART) 來分割模擬之假體核磁共振影像與模擬之腦部核磁共振影像，進行組織分割實驗後得到良好的腦部解剖組織影像。接下來更進一步實驗為增加腦部組織分割的準確度以提供神經解剖應用性，我們提出用一個促進式之決策樹 (Boosted decision tree) 分割模擬之假體核磁共振影像與模擬之腦部核磁共振影像與人體實體之腦部核磁共振影像，進行組織分割實驗後得到更準確之腦部解剖組織影像。以上兩個實驗之分割結果並且都用準確率 (Accuracy rate) 與  $k$  指標 ( $k$  index) 來量化評估其影像分割之表現。最後一個實驗是要得到腦部核磁共振影像之高品質分割影像，我們提出用一個促進式之決策樹為基礎結合以一個多階層仿視覺演算法為影像前處理之不均勻度校準分析，接著用促進式之決策樹來分割模擬之腦部核磁共振影像進行組織分割，除了能成功地對模擬之腦部核磁共振影像進行組織分割之外，經實驗分析後得到非常準確之腦部解剖組織影像，大大地改善了核磁共振影像之不均勻度與雜訊對影像分割之準確度所造成之影響，更加提高了組織分割的準確率，最後結果得到高品質的腦部組織分割，結果將對於腦部神經解剖之應用性有很大的幫助。

# A Supervised Segmentation of Brain MRI Tissue Using Decision Trees

Student : Wen-Hung Chao

Advisor : Dr. You-Yin Chen

Department of Electrical and Control Engineering  
National Chiao Tung University

## ABSTRACT

The purpose of this research is to achieve the high quality of brain tissue segmentation by using decision trees from magnetic resonance (MR) images. First, we proposed a multiscale retinex algorithm to correct the intensity inhomogeneity of brain MR images which include phantom data and animal data to obtain better image quality and clearer deep brain structures. The intensity inhomogeneity often occurs in MR images which are received by surface coils. The peak-signal-to noise (PSNR) and contrast-to- noise (CNR) were both used to evaluate the correction performance. Second, we used a classification and regression tree (CART) to segment brain MR images, including simulated phantom MR (SPMR) images and simulated brain MR (SBMR) images, to successfully segment brain tissues. Third, we proposed a boosted decision tree combined with fuzzy threshold to segment brain MR images, including SPMR images, SBMR images, and a real data, to achieve higher accuracy rate of brain tissue segmentation. The accuracy rate and  $k$  index were better when we used the boosted decision tree algorithm combined with a fuzzy threshold to classify gray matter (GM), white matter (WM), or cerebral-spinal fluid (CSF) in brain. Finally, we used the boosted decision tree through preprocessing procedure by the multiscale retinex algorithm to greatly improve the brain tissue segmentation from SBMR images. The accuracy rate was the best when we used the boosted decision tree algorithm combined with a multiscale retinex algorithm as a preprocessing procedure to classify GM, WM, or CSF in brain MR images.

The results shows that a boosted decision tree combined with preprocessing by the multiscale retinex algorithm can successfully improve the accuracy rate of MR brain tissue segmentation and can achieve a high quality of tissue segmentation in brain MR images.



## 誌 謝

首先感謝我的指導教授陳右穎博士在我研究方面的細心指導，使我的研究得以完整與周詳呈現與實現，使我在研究方法、研究思維學習到很多，對我未來的研究幫助很大，也拓展我的研究視野。在口試階段，感謝所有口試委員提供寶貴之意見使本論文得以更完備呈現，也感謝實驗室的同學、學弟與學妹們的幫忙協助使我能順利完成最後口試過程。在工作上，感謝長官們與同事們的幫忙與支持，在生活上，感謝我摯愛的雙親與我的家人在生活方面的支持、包容與鼓勵。

博士班進修階段求學歷程總會遇到許多的困難與挫折，然而除了需要體力以外更需要有健康與正向的想法與心態來面對這一切過程，我感謝我的師父太極門掌門人洪道子博士 ([www.taijimen.org](http://www.taijimen.org)) 收我為徒，我的師父教導我如何練好身體培養好體力、涵養武德與修改心性使我能夠以一個學習與感恩的心來接受這所有的經歷，也感謝太極門師兄師姊們真誠的關心與鼓勵，這一切使我在心情起伏時調適自己的精神良方，面臨事情能歡喜以對。

於此，謹以此論文獻給我的師父、師母、我的父親、母親、師兄師姊、我的師長、我所有的家人與朋友，感謝你們。

# Contents

<b>Chapter 1 Introduction .....</b>	<b>1</b>
1.1. The overview of the magnetic resonance imaging .....	1
1.2. Brain MR image quality and segmentation problem .....	5
1.3. Literature reviews .....	5
1.3.1. Reviews of the MR image inhomogeneity correction approaches .....	6
1.3.2. Reviews of the brain MR image segmentation approaches .....	7
1.3.3. Reviews of the MR brain image inhomogeneity correction prior to segmentation .....	9
1.4. Motivations .....	11
1.5. The goals of this research .....	12
1.6. The main contributions .....	13
1.7. The organization of this dissertation .....	15
<b>Chapter 2 Correction of Inhomogeneous MR Images Using Multiscale Retinex (MSR).....</b>	<b>16</b>
.....	16
2.1. Introduction .....	16
2.2. Materials and methods .....	17
2.2.1. Retinex algorithm .....	17
2.2.2. Single-scale retinex .....	18
2.2.3. The surround function .....	19
2.2.4. Adjustment of single-scale retinex output .....	20
2.2.5. Multiscale retinex .....	22
2.2.6. Phantom and animal magnetic resonance imaging .....	23
2.2.7. Peak signal-to-noise ratio and contrast-to-noise ratio analysis .....	24
2.3. Experimental results .....	25
2.3.1. Results of phantom image .....	25

2.3.2. Results of animal image.....	27
2.3.3. Comparisons of histogram equalization, local histogram equalization, and a wavelet-based algorithm with multiscale retinex.....	30
2.3.4. Results of peak signal-to-noise ratio and contrast-to-noise ratio analysis.....	34
2.4. Discussions.....	38
<b>Chapter 3 Segmentation of Brain MR Images Using a Classification and Regression Tree (CART) .....</b>	<b>40</b>
3.1. Introduction.....	40
3.2. Materials and methods.....	41
3.2.1. Image preprocessing.....	41
3.2.2. Segmentation.....	43
3.2.3. Decision tree classification.....	43
3.2.4. Decision tree construction.....	43
3.2.5. Simulated data.....	43
3.2.6. Accuracy rate of segmentation.....	50
3.3. Experimental results.....	51
3.3.1. Results of phantom image.....	51
3.3.2. Results of simulated brain MR image.....	54
3.4. Discussions.....	63
<b>Chapter 4 Segmentation of Brain MR Images Using a Boosted Decision Tree (BDT) .....</b>	<b>67</b>
4.1. Introduction.....	67
4.2. Materials and methods.....	68
4.2.1. MR data.....	68
4.2.2. Image preprocessing.....	69
4.2.3. Segmentation.....	69
4.2.4. Decision tree classification.....	70



4.2.5. Decision tree construction with gain ratio .....	71
4.2.6. Boosting.....	72
4.2.7. Fuzzy threshold.....	74
4.2.8. Pruning .....	74
4.2.9. Three-dimensional reconstruction .....	75
4.2.10. The evaluation index of segmentation .....	75
4.3. Experimental results .....	76
4.3.1. Segmentation of SPMR images.....	76
4.3.2. Segmentation of SBMR images.....	79
4.3.3. Comparison of segmentation with the other algorithms .....	84
4.3.4. Segmentation of real data in brain MR images.....	88
4.4. Discussions .....	91
<b>Chapter 5 Improving Segmentation of Brain MR Images Based on a Boosted Decision Tree through Preprocessing by the Multiscale Retinex Algorithm .....</b>	<b>96</b>
5.1. Introduction .....	96
5.2. Materials and methods.....	96
5.2.1. MR data in this experiment.....	96
5.3.2. Methods.....	97
5.3. Experimental results .....	98
5.3.1. Results of SBMR images.....	98
5.3.2. Segmentation of SBMR images.....	100
5.4. Discussions .....	107
<b>Chapter 6 The Summary and Future Works.....</b>	<b>109</b>
<b>References .....</b>	<b>111</b>

## List of Figure

Figure 1.1	Three axes systems and the directions of magnetic field ( $B_0$ , $B_1$ , and $M$ ) in MR imaging systems. ....	3
Figure 1.2	An example of MRI system. ....	4
Figure 1.3	The whole image processing procedures of this research. ....	13
Figure 2.1	A histogram distribution plot that illustrated the gain and offset values of an MR image. ....	21
Figure 2.2	Corrected MR images of a phantom demonstrating the performance of retinex. ....	26
Figure 2.3	Performance of the retinex was demonstrated with adjusted MR images of a coronal section of the rat brain. ....	29
Figure 2.4	Corrected MR images of a phantom, obtained via four methods. ....	32
Figure 2.5	Corrected MR images of a rat brain obtained from four algorithms. ....	34
Figure 3.1	Local area of each spatial feature. ....	43
Figure 3.2	Decision tree configuration. ....	46
Figure 3.3	Segmentation of phantom images from IBSR. ....	53
Figure 3.4	Average accuracy rates of segmentation obtained using a decision tree with different spatial information from original phantom images with different noise variations and inhomogeneities. ....	54
Figure 3.5	Results of segmentation using a decision tree for simulated MR images obtained from BrainWeb. ....	55
Figure 3.6	Average accuracy rates of segmentation with different spatial information from the original MR images with noise levels of T1n3, T1n5, T1n7, T1n9, and T1n15. ....	56
Figure 3.7	Results of segmentation using a decision tree for simulated MR images. ....	57
Figure 3.8	Average accuracy rates of segmentation with different spatial information from MR images with noise parameters of T1n3RF20, T1n5RF20, T1n7RF20, T1n9RF20, and T1n15RF20. ....	58
Figure 3.9	Results of segmentation using a decision tree for simulated MR images. ....	60
Figure 3.10	Average accuracy rates of segmentation with different spatial information from MR images with noise parameters of T1n3RF40, T1n5RF40, T1n7RF40, T1n9RF40, and T1n15RF40. ....	61
Figure 3.11	Accuracy rates of GM, WM, and CSF in simulated MR images segmented using a decision tree with spatial information ( $G, x, y, r, \theta$ ) for T1n3, T1n5, T1n7, T1n9, and T1n15. ....	62
Figure 4.1	A flow diagram of image processing procedures for MR image segmentation. ....	70
Figure 4.2	Schematic diagram of the decision tree structure. ....	71
Figure 4.3	Accuracy rates of region segmentation obtained using different spatial features from simulated phantom MR images. ....	78
Figure 4.4	Images segmented from simulated phantom MR images with different spatial features and various noise and inhomogeneity levels. ....	79
Figure 4.5	Mean accuracy rates of tissue segmentation from simulated brain MR images. ....	81
Figure 4.6	Accuracy rates of tissue segmentation using a boosted decision tree algorithm on simulated brain MR images. ....	82
Figure 4.7	Segmentation of simulated brain MR images from BrainWeb. ....	83

Figure 4.8	A 3D reconstruction of segmented brain image data in axial view. ....	84
Figure 4.9	Segmentation of real brain MR imaging data.....	91
Figure 5.1	Image processing procedures in this experiment.....	97
Figure 5.2	Average accuracy rates of all brain tissues segmented using BDT with spatial feature $(G x, y, r, \theta)$ and $(S x, y, r, \theta)$ for different boost trial numbers. ....	99
Figure 5.3	Images from original, corrected using MSR, and segmented using BDT from SBMR with T1n3RF20 and T1n9RF40.....	100
Figure 5.4	Accuracy rates of tissue segmentation using a BDT algorithm on SBMR images with T1n3RF20, T1n5RF20, T1n7RF20, and T1n9RF20.....	102
Figure 5.5	Accuracy rates of tissue segmentation using a BDT algorithm on SBMR images with T1n3RF40, T1n5RF40, T1n7RF40, and T1n9RF40.....	105



## List of Table

Table 2.1	Comparisons of PSNR and CNR for phantom images obtained from retinex algorithms with those obtained from histogram equalization, local histogram equalization, and the wavelet-based algorithm.	36
Table 2.2	Comparisons of PSNR and CNR for animal images obtained from retinex algorithms with those obtained from histogram equalization, local histogram equalization, and the wavelet-based algorithm.	37
Table 3.1	Designations of the original phantom images obtained by combining the noise levels and inhomogeneities parameters.	49
Table 3.2	Designations of the original simulated MR images obtained by combining the noise levels and inhomogeneities parameters.	50
Table 4.1	Segmentation accuracy rates from SBMR images using the boosted decision tree, the SRG, and the AS algorithm.	86
Table 4.2	The segmentation $k$ indexes from SBMR images using the boosted decision tree, the SRG, and the AS algorithm.	87
Table 4.3	Segmentation of MR images from two real subjects using the boosted decision tree, the SRG, and the AS method.	90

# Chapter 1 Introduction

## 1.1. The overview of the magnetic resonance imaging

Magnetic resonance imaging (MRI) has been used to diagnose various diseases for a long time and represented an important diagnostic technique in medicine for the effective and noninvasive detection of objects such as cancers, tumors, edema, infarctions, organs, blood vessels, and brain tissues. MRI can also obtain soft anatomical tissues of high quality in medical image application. It has become a well-known medical image equipment and well-used technique in neurological diagnosis and clinical applications. The advantages of MRI are more obvious than other medical image equipments such as CT, ultrasound, and X-ray.

Bloch *et al.* has discovered the phenomenon of nuclear magnetic resonance (NMR) through a nuclear induction experiment in 1946 [1–3]. Purcell *et al.* also independently discovered the NMR in liquids and in solids in 1946 [4]. Many discoveries and developments about NMR founded the MRI technique. Magnetic resonance (MR) image is constructed with the bases of the NMR phenomenon. The principles of NMR are described as below. In general, nuclei consist of protons and neutrons. In quantum mechanical property, the particles (electrons, protons, and neutrons) of atom rotates around their own axis and the rotating motion is called spin. The phenomena of spin exist in all the charged particles which are similar to small magnets. The magnetic dipole exists in all of the particles. The phenomenon of spin is more exhibited in nuclei with odd number of protons and neutrons. One of these is hydrogen. Hydrogen which has only one proton and is contained in water or fat can create the strongest magnetic moment. More than 63% of the human body is composed of water or fat. Thus, magnetic dipole variations of the hydrogen are widely applied in imaging for human body. In MRI procedure, the directions of magnetic field ( $B_0$ ,  $B_1$ , and  $M$ ) and three axes are

shown in Figure 1.1. Three axes are defined in MR imaging domain which are x axis (from back to front), y axis (from left arm to right arm), and z axis (from head to feet). The spin of proton in hydrogen can also create a tiny magnet. A collection of the magnetic dipole directions of spin of protons in hydrogen are arranged in the same direction of the magnetic field when all of them are located in a high external static magnet ( $B_0$ ). The magnetic dipole directions of them are random orientations in the absence of an external magnetic field. The direction of the high external static magnet is usually called z direction (z axis). The units used to measure the strength of magnetic field are Tesla and gauss. An example to evaluate the magnetic strength is that the strength of the earth is 0.5 gauss. One Tesla equals to 10,000 gauss.

The protons with spin axes in a high external static magnet also has precession phenomenon whose direction is parallel or anti-parallel to the magnetic field ( $B_0$ ). The precession orientation which is a collection component ( $M$ ) of magnetic dipole of all protons is around the magnetic field  $B_0$ . The precession phenomenon also exist frequency. The frequency of precession is called Larmor frequency which is the product of the gyromagnetic ratio and the magnetic field ( $B_0$ ). The precession frequency is linearly proportional to the strength of the high external magnetic field ( $B_0$ ). The gyromagnetic ratio of Hydrogen nucleus is 42.58 MHz/Tesla. Larmor frequency of hydrogen nucleus is 63.86 MHz when in a 1.5 Tesla of an external magnetic field ( $B_0$ ). Larmor frequency of Hydrogen nucleus is 127.74 MHz when in a 3 Tesla of an external magnetic field ( $B_0$ ).

The precession direction of proton of hydrogen in human body is along z axis and its precession frequency also exists in a strong external magnetic field ( $B_0$ ) for aligning the protons. In order to acquire the signals of magnetic dipole variations from hydrogen nuclei, the energy of a radio frequency (RF) pulse must be used to generate the signals and then the RF pulse coil transmitter will be turned off. When the same precession frequency of a RF pulse emits to protons, the nuclear magnetic resonance (NMR) phenomenon is generated. The

RF pulse is created from RF coils to construct a RF magnetic field (called  $B_1$  field). The strength of  $B_1$  field is smaller than that of external magnetic field ( $B_0$ ) along the x-y plane. The energy transmitted from the RF pulse and  $B_1$  field is absorbed into protons of hydrogen in human body to force the proton precession with a perpendicular direction ( $M_{x-y}$ ) to z axis. The energy of protons absorbed from  $B_1$  field begins to release and the direction of the component  $M_{x-y}$  will realign to the z direction (direction of  $B_0$  field) after the RF pulse is turned off. The protons will release the energy absorbed from the RF pulse in the original direction of a collection component of magnetic dipole of all protons ( $M$ ) during the realigning time. The realigning time is called relaxation time and the realigning procedure is called free induce decay (FID). The released energy (radio frequency energy) can be received by a RF receiver coil to obtain the RF signals which can be transmitted to a computer to construct the MR images.

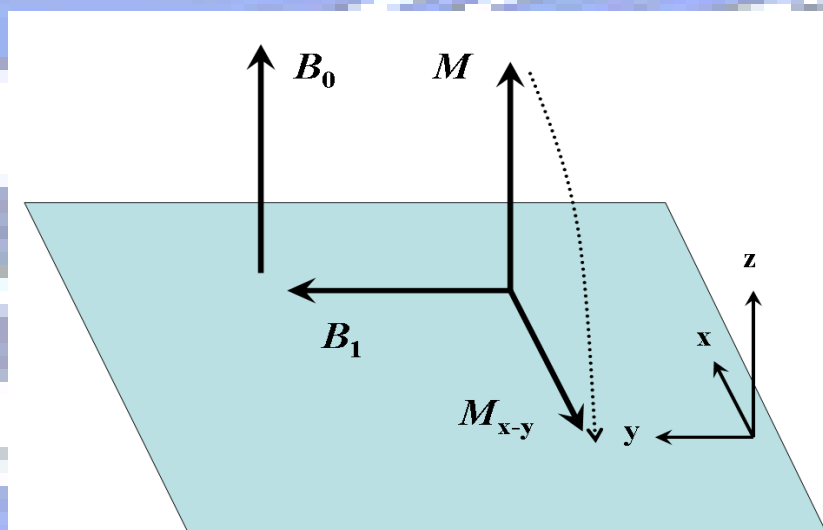


**Figure 1.1** Three axes systems and the directions of magnetic field ( $B_0$ ,  $B_1$ , and  $M$ ) in MR imaging systems.

Two important parameters existing in FID procedure are T1 and T2. Two kinds of relaxation processes are: T1 relaxation time (longitudinal relaxation time) and T2 relaxation

time (transverse relaxation time). T1 relaxation time is the period while the protons release the energy absorbed from the RF pulse as heat to their surrounding environment (lattice) and the direction of a collection of magnetic dipole of all protons return to their equilibrium position (the original direction of component  $M_z$ , z direction, or longitudinal plane). T1 relaxation time is also called spin-lattice relaxation time. T2 relaxation time is the period while the protons release the energy absorbed from the RF pulse to their surrounding protons (spin) and the procedure causes a decrease in transverse magnetization ( $M_{x-y}$  in x-y plane). T2 relaxation time is also called spin-spin relaxation time. Three types of MRI image are: T1-weighted image, T2-weighted image and PD-weighted image. T1-weighted image is constructed with the measurement of the T1 relaxation times for different tissues. T2-weighted image is obtained with calculation of the measured T2 relaxation times in different tissues. PD-weighted image which is the proton density image is acquired with the evaluation of the number of protons in a unit for different tissues. An example of MRI system is shown in Figure 1.2.



**Figure 1.2** An example of MRI system (MRI/MRS Lab, National Taiwan University).



## **1.2. Brain MR image quality and segmentation problem**

In this dissertation, we investigate some problems about MR image inhomogeneity and noise that might affect the image quality and decrease the accuracy of segmentation for diagnosis application. We address these problems to improve the brain MR image quality, to increase the segmentation accuracy of brain MR image, and to achieve the high quality of segmentation for brain MR anatomical structure.

MR image intensities acquired from homogeneous tissue are often inhomogeneities due to bad radio frequency coil uniformity, gradient-driven eddy currents, and human anatomy both inside and outside the field of view. The noise existing in MR image also decreases the image quality due to the body movements, acquiring procedure, and receiver coils.

Several factors make brain MR image segmentation difficult, including similar imaging intensities in different regions of the brain, overlapping intensity distributions, background noises, and radio-frequency (RF) inhomogeneities. The accuracy of segmenting the cortical surface for analyzing the volumes of different tissues such as gray matter (GM) and white matter (WM) significantly affects clinical diagnoses, but this is difficult to be achieved due to the presence of imaging noise and inhomogeneities. Furthermore, it is more difficult to improve the segmentation accuracy of brain MR image to achieve high quality of segmentation for anatomical structure.

## **1.3. Literature reviews**

For MR image anatomical structure quality, the image intensity inhomogeneity and segmentation are two main problems. In this Section, we will review the literatures about inhomogeneity correction, segmentation approaches, and inhomogeneity correction prior to segmentation approaches for MR images.

### 1.3.1. Reviews of the MR image inhomogeneity correction approaches

One of these factors is RF inhomogeneities of MR images. It often occurs in MR images obtained by receiving with surface coils during scanning on MR imaging. Several techniques were urged on improvements of surface coils to increase the MR image quality to help the clinical diagnosis [5–11]. It is more expensive to decrease effects of RF inhomogeneities by improving surface coils through the hardware technique. Therefore, an easy way through software methodology with low cost is helpful to decrease the effects of RF inhomogeneities. Many approaches have been recently proposed to correct MR image to improve the detection and diagnosis capabilities [12–20]. Haiguang *et al.* addressed the performances of enhancing hybrid MR images that were decreased by T2-weighted effects and measurement noise [11]. They reduce the imaging time using hybrid imaging sequences such that the T2 effects act as a distortion filter which will damage image quality and detection and which can be estimated and used in Wiener filter for global T2 amplitude restoration. The linear prediction was also used to predict the local signal and phase to estimate the frequency response of the T2 filter. These combined techniques successfully correct T2 distortion and reduce the measurement noise to demonstrate both phantoms and human data.

Sled *et al.* corrected the MR image intensity inhomogeneity to achieve high performance without requiring a model of tissue classes present [13]. They used a nonparametric nonuniform intensity normalization to estimate both the multiplicative bias field and the distribution of true tissue intensity. They successfully corrected the simulated and real data to reduce intensity nonuniform and tissue intensity variation to obtain uniform image. The relative segmentation approaches are to correct the inhomogeneous image prior to the segmentation. Ahn *et al.* [14] proposed a method of local adaptive template filtering for enhancing the signal-to-noise ratio (SNR) in MRI without reducing the resolution. Moreover, Styner *et al.* [15] showed that a parametric bias-field correction method could correct bias distortions that are much larger than the image contrast. Likar *et al.* [16] proposed a

model-based correction method to adjust inhomogeneity in the intensity of an MR image. They applied an inverse image-degradation model where parameters were optimized by minimizing the information content of simulated and real MR data. Lin *et al.* [17] used a wavelet-based algorithm to approximate surface-coil sensitivity profiles. They corrected image intensity inhomogeneities acquired by surface coils, and used a parallel MRI method to verify the spatial sensitivity profile of surface coils from the images captured without using a body coil. It has also been shown [18, 19] that contrast enhancement can be used to improve the quality of MR images. More researches [20–25] were also urged to correct the RF inhomogeneity and to model bias field of MR images to improve the image quality. These proposed researches exhibit the importance of MR image inhomogeneity correction. In addition, the study of brain structure through MR image correction is very important for neurological applications. However, the correction of MR image intensity inhomogeneity is also a problem to improve the image quality with better visualization.

### **1.3.2. Reviews of the brain MR image segmentation approaches**

Segmentation is one of the techniques used to classify the brain tissues in MR images, which is a basic problem for identifying anatomical structures in MR image processing. Several segmentation methods have been applied in the analysis of anatomical structures involving three-dimensional (3D) reconstruction, tissue-type contour definition, and clinical diagnosis [26, 27], and in cortical surface segmentation, volume assessment of brain tissue, tissue classification, tumor segmentation, and characterization of various brain diseases such as sclerosis, epilepsy, stroke, cancer, and Alzheimer's disease [28, 29]. The accuracy of segmenting the cortical surface for analyzing the volumes of different tissues such as gray matter (GM) and white matter (WM) significantly affects clinical diagnoses, but this is difficult to be achieved due to the presence of imaging noise and inhomogeneities. Several segmentation techniques have been proposed for improving the detection of brain structures

in MR images in diagnostic and neuroanatomical applications. Both manual and automatic segmentation methods are used to segment brain MR images. Manual segmentation such as thresholding is a traditional method used to distinguish different tissues in MR brain images [30–32], but this is difficult in the presence of a low contrast-to-noise ratio, low signal-to-noise ratio (SNR), and overlapping of tissues in the gray-level distributions, and it is also very labor-intensive and time-consuming [33]. Therefore, several studies have investigated automatic segmentation methods for distinguishing brain MR images structures and improving the efficiency of segmentation and tissue classification [27, 34–41]. Marroquin *et al.* presented an automatic segmentation method based on an accurate and efficient Bayesian algorithm [42]. Automatic segmentation based on a constrained Gaussian mixture model framework employed an expectation-maximization algorithm to determine parameters and segment both simulated and real three-dimensional, T1-weighted noisy MR images [43]. Some of these automatic segmentation methods were used to classify the tissues (GM, WM, and cerebrospinal fluid (CSF)) in brain MR images. An automatic segmentation method has also been used to segment WM lesions in brain MR images [44]. Zoroofi *et al.* [27] demonstrated favorable segmentation performance using an automatic segmentation technique combined with region growing, gray morphological dilation, filtering, and thresholding to assess the necrotic formal head area. Admiraal-Behloul *et al.* [39] used a fully automatic segmentation method combined with adaptive and reasoning levels to perform white matter hyperintensity (WMH) segmentation for volume qualification and similarity on older MR images. Dou *et al.* [45] proposed a framework of fuzzy information fusion combined with registration operation, feature extraction, fuzzy feature fusion operation, and fuzzy region growing to automatically segment brain tumor tissues on MR images. Xia *et al.* [41] proposed a knowledge-driven algorithm for automatically delineating the caudate nucleus (CN) region in MR-imaged human brains. MR image tissue segmentation is important to accurately distinguish gray matter (GM), white matter (WM), and cerebral-spinal

fluid (CSF) in the brain [34, 35, 42, 46, 47], while automatic MR image segmentation is often used to classify brain tissue. Many automatic segmentation techniques use probabilistic classification to segment brain tissues [34, 43, 44, 48], while others use wavelet coefficients as spatial features of voxels in three-dimensional (3D) imaging for clustering the GM, WM, and CSF with fuzzy theory. Fuzzy logical models have been used to test phantom, normal, and Alzheimer's brain MR images in order to reduce the difference of partial volume averaging on the boundary of the ventricles [49]. Another wavelet application has been used to design attribute vectors as spatial features of voxels for determining correspondence in 3D brain MR images [50]. Segmentation applications include tissue volume quantification and 3D spatial structure reconstruction, which greatly aid in disease diagnosis [26, 27, 31, 33, 36, 51–56]. However, it remains necessary to increase the accuracy of automatic segmentation of the GM, WM, and CSF in brain MR images to obtain clearer anatomical structures.

Several studies have improved coil sensitivities and the performance of transmitter devices [57–60], but it remains difficult and expensive to reduce imaging noise and inhomogeneity through hardware improvements. Therefore, it is valuable to find an easy way with a low cost technique to obtain better MR brain structures. Furthermore, it is important to increase the ability through software improvements to discriminate different tissue characteristics of brain structures.

### **1.3.3. Reviews of MR image inhomogeneity correction prior to segmentation**

Although many studies on segmentation of MR images aimed to obtain the anatomical structures of human body, the more precise analysis of MR images is still a difficult problem. Therefore, many researches preprocessed intensity inhomogeneity correction and then segmented MR images to achieve the better image quality. Zhou *et al.* presented a method of RF inhomogeneity correction for brain tissue segmentation in MRI [46]. They proposed a correction method to model image intensity variation to correct inhomogeneity of MR images

from both phantom and physical data to improve the segmentation. The results showed a significant improvement of MR image segmentation through preprocessing by this inhomogeneity correction. Andersen *et al.* proposed a robust and comprehensive approach for automatic segmentation and quantitative tissue volume measure of normal brain composition [34]. They used statistical recognition methods based on a finite mixture model to partition GM, WM, and CSF of MR *in vivo* data. RF inhomogeneity effects on the images were also removed using a recursive method to support heterogeneous data with multispectral MR images. They segmented T1-weighted, T2-weighted, and PD-weighted MR images from non-human and human data. Therefore, several studies have been investigated on automatic segmentation methods for distinguishing brain MR images structures and improving the efficiency of segmentation and tissue classification [2, 9–16]. Chard *et al.* [61] used reproducibility and sensitivity of brain tissue volume measurement to correct low spatial frequency image nonuniformity, which was assumed as artifacts. They used SPM99 to segment GM, WM, and CSF of brain MR images. Shufeng *et al.* [62] used a background removing method to correct MR image intensity nonuniformity. The MR images were filtered in advance. The MR images were then segmented by region growing method. Chen *et al.* [63] proposed a fuzzy c-means (FCM) algorithm based on intensity inhomogeneity correction and segmentation of MR images. Pan *et al.* [64] proposed an efficient automatic framework for segmentation of brain MR images. They removed the non-brain tissue and estimated bias field to correct intensity inhomogeneity for preprocessing. Other bias field methods [65] were also used to correct intensity inhomogeneity for MR image segmentation. More correction approaches of intensity variation in MR images for tissue segmentation were also studied [66–68]. These studies demonstrate the importance of segmentation for neurological applications. However, the increasing accuracy of segmentation is more important in classifying different brain tissues for improving anatomical structures in real applications.

## 1.4. Motivations

Although there were many researches of MR image inhomogeneity correction as mentioned in the literature review, the better image quality through image inhomogeneity correction still needs to be achieved. The image noise and intensity inhomogeneity are two main factors to affect brain MR images quality. Besides, the deep brain structures of MR images are difficult to be recognized and are very important in neuroanatomical applications. Therefore, we will improve the image quality with better visualized rendition by a proposed inhomogeneity correction method to correct the intensity inhomogeneity of brain MR image and to improve the detection and diagnosis capabilities.

Both the hardware improvement through coil sensitivities and the performance of transmitter devices to reduce imaging noise and inhomogeneity are more expensive. Furthermore, the studies of literature review showed that the clear anatomical structures also remain difficult to be obtained. However, a low cost technique to obtain better MR brain structures is worth studying. Thus, we will propose an easy implementation method through software technique of automatic segmentation algorithm for classifying the tissues (GM, WM, and CSF) of brain MR images to obtain clearer anatomical structures. Moreover, the increasing accuracy of segmentation demonstrated in the literature reviews is more important in classifying different brain tissues for improving anatomical structures in real applications. We will propose another automatic segmentation method to improve the segmentation accuracy of the GM, WM, and CSF in brain MR images to improve anatomical structures. Similarly, greatly increasing the segmentation accuracy of brain MR image and achieving high quality of segmentation are also very important. Consequently, we will combine the intensity inhomogeneity correction algorithm and the proposed segmentation method to increase the segmentation accuracy of the GM, WM, and CSF in brain MR images to achieve the high quality of segmentation for anatomical structures.

## 1.5. The goals of this research

The goals of this research address these problems described in Section 1.2, 1.3, and 1.4. The whole image processing procedures of this research is shown in Figure 1.3 which will match the goals of this research. According to the problems described in literature reviews and motivations, we will solve the problems with the whole image processing procedures of Figure 1.3. The goals of this research are: to obtain better image quality, to obtain better anatomical structures, to obtain more segmentation accuracy, and to achieve high quality of segmentation for brain MR images.

We first proposed a multiscale retinex algorithm to correct the intensity inhomogeneities of brain MR images which include phantom data and animal data to obtain clearer deep brain structures and better image quality. Secondly, we used an automatic segmentation of classification and regression tree (CART) to segment brain MR images and to obtain better brain anatomical structures. Thirdly, we proposed a boosted decision tree combined with fuzzy threshold to segment brain MR images which include simulated phantom MR (SPMR) images, simulated brain MR (SBMR) images, and a real data to obtain higher accuracy of segmentation and much better brain anatomical structures. Finally, we used the boosted decision tree combined with the multiscale retinex algorithm as a preprocessing procedure to greatly improve the segmentation accuracy from SPMR images and SBMR images.

The final objective of this dissertation is to propose a segmentation method based on a boosted decision tree through preprocessing by a multiscale retinex algorithm for correcting intensity inhomogeneity to achieve high quality of segmentation of GM, WM, and CSF from brain MR images for anatomical structures.



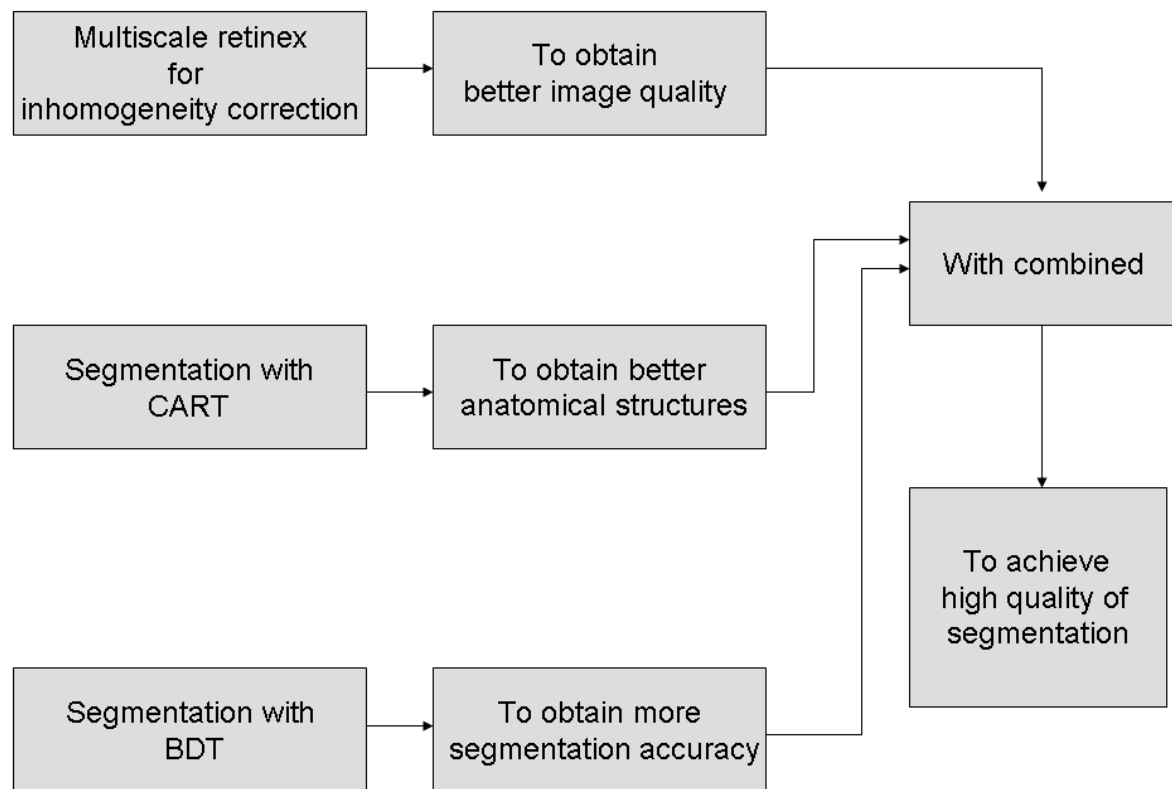


**Figure 1.3** The whole image processing procedures of this research.

## 1.6. The main contributions

In this dissertation, we address the MR image quality and segmentation problems to improve the quality of brain MR image segmentation by focusing on four experiments which are correction of inhomogeneous MR images using multiscale retinex algorithm, segmentation of brain MR images using a CART decision tree, segmentation of brain MR images using a boosted decision tree, and segmentation of brain MR images based on boosted decision tree through preprocessing by the multiscale retinex algorithm to achieve the goals of this research.

A new method for enhancing the contrast of magnetic resonance (MR) images by retinex algorithm was proposed. It can correct the blurring in deep anatomical structures and inhomogeneity of MRI. Multiscale retinex (MSR) employed single scale retinex (SSR) with

different weightings to correct inhomogeneities and enhance the contrast of MR images. An automatic segmentation method based on a CART decision tree was then proposed to classify the brain tissues of MR images. Next, a boosted decision tree segmentation algorithm combined with fuzzy threshold algorithm was proposed to improve the accuracy rate of brain tissue segmentation from brain MR images. Finally, the high segmentation quality of brain tissue (GM, WM, and CSF) from brain MR images were performed based on a boosted decision tree combined with a preprocessing by the multiscale retinex (MSR) algorithm.

The main contributions of this dissertation are:

1. A multiscale retinex (MSR) algorithm is used to successfully correct the intensity inhomogeneity of brain MR images that can adjust different weighting with combined three scale of single scale retinex (SSR) and to perform the best trade off between peak-signal-to-noise- ratio (PSNR) and contrast-to-noise-ratio (CNR).
2. A multiscale retinex (MSR) algorithm is used to clear the deep brain structures (medical forebrain bundle: MFB) of rat brain and to obtain better image quality.
3. An automatic segmentation of classification and regression tree (CART) with a supervised method is proposed to effectively segment the brain tissues of simulated phantom MR (SPMR) images and simulated brain MR (SBMR) images.
4. A boosted decision tree combined with fuzzy threshold and an appropriate boost trial number is also proposed to more accurately segment brain tissues of SPMR, SBMR images, and a real data. The segmentation performances are also successfully evaluated by a 3D reconstruction method.
5. Two kinds of evaluation index, accurate rate and  $k$  index, are effectively used to investigate the segmentation performance from brain MR images.
6. A high quality of segmentation of gray matter (GM), white matter (WM), and cerebral spinal fluid (CSF) from brain MR images is improved based on the boosted decision tree (BDT) through preprocessing by a MSR algorithm.

## **1.7. The organization of this dissertation**

The rest of this dissertation is organized as follows: Chapter 2 declares the proposed multiscale retinex algorithm to correct the brain MR image intensity inhomogeneity. Chapter 3 presents an automatic segmentation method with classification and regression tree (CART) to segment brain MR images. Chapter 4 presents a boosted decision tree combined with fuzzy threshold to segment brain MR images. Chapter 5 presented the boosted decision tree to segment brain MR images through preprocessing by multiscale retinex (MSR) algorithm. Finally, the conclusion and future works are discussed in Chapter 6.



## Chapter 2 Correction of Inhomogeneous MR Images Using Multiscale Retinex (MSR)

### 2.1. Introduction

Due to the importance of MR image inhomogeneity correction, it is a valuable to investigate how to reduce imaging noise and inhomogeneity and to improve the MR image quality. Therefore, we proposed a multiscale retinex (MSR) algorithm to correct the intensity inhomogeneity of MR image, to improve the image quality, and to help the detection and diagnosis capabilities.

Stretching the pixel dynamic range of certain objects in an image is a widely adopted approach for enhancing the contrast [69]. The image contrast-enhancement techniques can be divided into two types: global and local histogram enhancement [70, 71]. The (global) histogram equalization technique improves the uniformity of the intensity distribution of an image [70, 71] by equalizing the number of pixels at each gray level. The disadvantage of this method is that it is not effective in improving poor localized contrasts [72]. Local histogram enhancement [71, 73] used an equalization method to improve the detailed histogram distribution within small regions of an image, and also preserved the gray-level values of the image. The obtained histogram is updated in neighboring regions at each iteration, then local histogram equalization is applied. However, the visual perception quality of a processed image is subjective, and it is known that both global and local histogram equalization do not result in the best contrast enhancement [71–76].

For image processing, the presence of the nonuniformity of an MR image caused by the inhomogeneity of the magnetic intensity is very similar to that of a normal image resulted from bad illumination sources and environmental conditions. To address the nonuniformity problem of an image, Land [77], inspired by the psychological knowledge about the brain's

processing of image information from retinas, developed a concept named retinex as a model for describing the color constancy in human visual perception. His idea is that the perception of human is not completely defined by the spectral character of the light reaching the eye from scenes. It includes the processing of spatial-dependant color and intensity information of the retina of an eye, which can be realized by the computation of dynamic-range compression and color rendition [78–81]. Moreover, Jobson *et al.* [82] found in his study that the selection the parameters of surrounding function can greatly affect the performance of the retinex. He then balanced the dynamic compression and color rendition by using multi-scale retinex (MSR). Although hardware techniques can be utilized to correct the image inhomogeneity and to enhance image contrast, they are costly and inflexible. Hence, it is promising to develop easy and low-cost software-based techniques to address the inhomogeneity problem in MR images. In this Chapter, we introduced a software-based retinex algorithm for contrast enhancement and dynamic-range compression that improve image quality by decreasing image inhomogeneity.

## **2.2. Materials and methods**

### **2.2.1. Retinex algorithm**

In general, the human visual system is better than machines when processing images. Observed images of a real scene are processed based on brightness variations. The images captured by machines are easily affected by environmental lightening conditions, which tend to reduce its dynamic range. On the contrary, the human visual system can automatically compensate the image information by psychological mechanism of color constancy. Color constancy, an approximation process of human perception system, makes the perceived color of a scene or objects remain relatively constant even with varying illumination conditions. Land [77] proposed a concept of the retinex, formed from "retina" and "cortex", suggesting

that both the eye and the brain are involved, to explain the color constancy processing of human visual systems. After the human visual system obtain the approximate of the illuminating light, the illumination is then discounted such that the "true color" or reflectance can be determined. More details about subject color constancy can be found in [83–84].

Hurlbert and Poggio [80] and Hurlbert [81] applied the retinex properties and luminosity principles to derive a general mathematical function. Differences arose when images from various center/surround functions in three scales of gray-level variations were shown. Hurlbert [80, 81] applied a center/surround function to solve the brightness problem, using the learning mechanism of neural networks and a general solution to evaluate the relative brightness in arbitrary environments.

Although Jobson *et al.* proposed a single-scale retinex (SSR) algorithm that could support different dynamic-range compressions [82, 85], the multi-scale retinex (MSR) can better approximates human visual processing, verified by experiments [82, 85–87], by transforming recorded images into a rendering which is much closer to the human perception of the original scene.

### 2.2.2. Single-scale retinex

The basics of an SSR [77] were briefly described as follows. A logarithmic photoreceptor function that approximates the vision system was applied, based on a center/surround organization [77, 85]. The SSR was given by

$$R_i(x, y) = \log I_i(x, y) - \log[(I_i(x, y) * F(x, y))], \quad (2.1)$$

where  $R_i(x, y)$  was the retinex output,  $I_i(x, y)$  was the image distribution in the  $i$ th spectral band, and "\*" represented the convolution operator. In addition,  $F(x, y)$  was represented as

$$\iint F(x, y) dx dy = 1, \quad (2.2)$$

which was the normalized surround function. The purpose of the logarithmic manipulation was to transform a ratio at the pixel level to a mean value for a larger region. We selected MR images for our implementation with this form in Equation (2.5) proposed by Land [77].

This operation was applied to each spectral band to improve the luminosity, as suggested by Land [77]. It was independent from the spectral distribution of a single-source illumination since

$$I_i(x, y) = S_i(x, y)r_i(x, y), \quad (2.3)$$

where  $S_i(x, y)$  was the spatial distribution on an illumination source, and  $r_i(x, y)$  was the reflectance distribution in an image, so

$$R_i(x, y) = \log \frac{S_i(x, y)r_i(x, y)}{\overline{S_i(x, y)r_i(x, y)}}, \quad (2.4)$$

$$S_i(x, y) \approx \overline{S_i(x, y)}, \quad (2.5)$$

where  $\overline{S}$  represented the spatially weighted average value, as long as

$$R_i(x, y) \approx \log \frac{r_i(x, y)}{\overline{r_i(x, y)}}. \quad (2.6)$$

This approximate equation was the reflectance ratio, and was equivalent to illumination variations in many cases.

### 2.2.3. The surround function

Several types of surround function were implemented. First, an inverse-square spatial surround function proposed by Land [77] was formed as

$$F(x, y) = 1/r^2, \quad (2.7)$$

where

$$r = \sqrt{x^2 + y^2} \quad (2.8)$$

could be changed to another surround function as

$$F(x, y) = \frac{1}{1 + (r^2 / c_1^2)}, \quad (2.9)$$

where  $c_1$  was a space constant.

Moore *et al.* [78–79] used a surround function on an exponential function with the absolute value  $r$  as

$$F(x, y) = e^{-r/c_2} \quad (2.10)$$

to approximate the spatial response, where  $c_2$  was a space constant.

Hurlbert and Poggio [80] and Hurlbert [81] used the Gaussian surround function

$$F(x, y) = Ke^{-r^2/c_3^2} \quad (2.11)$$

to reconcile natural and human vision, where  $c_3$  was a space constant. For a given space constant, the inverse-square surround function accounted for a greater response from the neighboring pixels than the exponential and Gaussian functions. The spatial response of the exponential surround function was larger than that of the Gaussian function at distant pixels. Therefore, the inverse-square surround function was more commonly used in global dynamic-range compression, and the Gaussian surround function was generally used in regional dynamic-range compression [82].

The exponential and Gaussian surround functions were able to produce good dynamic-range compression over neighboring pixels [78, 81–82]. From the proposed surround functions [78–81], the Gaussian surround function exhibited good performance over a wider range of space constants, so it was used to enhance contrasts and to solve the inhomogeneity of MR images in the present study.

#### 2.2.4. Adjustment of single-scale retinex output

The final process output was not obvious from the center/surround retinex proposed by



Land [77]. Moore *et al.* [78] also offered an automatic gain and offset operation, in which the triplet retinex outputs were regulated by the absolute maximum and minimum values of all scales in a scene. In this study, a constant gain and offset technique (as shown in Figure 2.1) was used to select the best rendition.

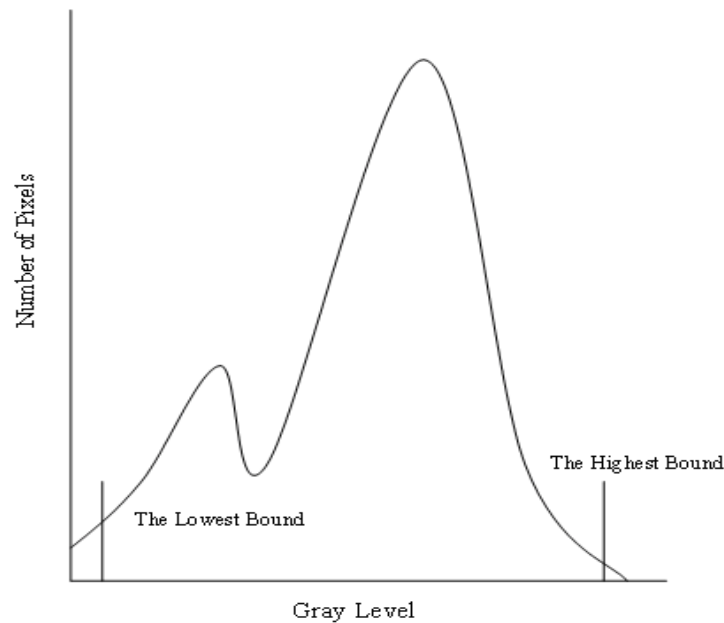


**Figure 2.1** A histogram distribution plot that illustrated the gain and offset values of an MR image, which underwent the single-scale retinex (SSR) to enhance its contrast.

Figure 2.1 described how to choose the transferred output interval of both the highest- and lowest-scale rendition scene for each SSR. The offset value can be directly determined by the lower bound. Furthermore, the gain can be computed according to the range between the upper and lower bounds. The selection of a larger upper bound led to minor contrast improvement but prevents heavy distortion caused by truncation. The lower bound functions in a similar way as explained previously. Adjustments to the gain and offset result in the retinex outputs caused little information lost, and the constant gain and offset of retinex was

independent of the image content. We evaluated the effects of variations in the histogram characteristics in a gray-level scene. The gain and offset were constant between images in accordance with the original algorithm proposed by Land [77], and also demonstrated that it can be applied as a common manipulation to most types of images.

### 2.2.5. Multiscale retinex

It was our intention to select the best value of scale factor  $c$  in the surround function  $F(x, y)$  based on the dynamic-range compression and brightness rendition for every SSR. We also intended to maximize the optimization of the dynamic-range compression and brightness rendition. MSR was a good method for summing a weighted SSR according to

$$R_{MSRi} = \sum_{n=1}^N \omega_n R_{ni}, \quad (2.12)$$

where  $N$  represented a scaling parameter,  $R_{ni}$  represented the  $i$ th component of the  $n$ th scale,  $R_{MSRi}$  was the  $n$ th spectral component of the MSR output, and  $\omega_n$  represented the multiplication weight for the  $n$ th scale. The differences between  $R(x, y)$  and  $R_n(x, y)$  resulted in surround function  $F_n(x, y)$  became

$$F_n(x, y) = Ke^{-r^2/c_n^2}. \quad (2.13)$$

MSR combined various SSR weightings [82, 85], selecting the number of scales used for the application and evaluating the number of scales that can be merged. Important issues to be concerned were the number of scales and scaling values in the surround function, and the weights in the MSR. MSR was implemented by a series of MR images, based on a trade-off between dynamic-range compression and brightness rendition. Also, we needed to choose the best weights in order to obtain suitable dynamic-range compression at the boundary between light and dark parts of the image, and to maximize the brightness rendition over the entire image. We verified the MSR performances on visual rendition with a series of MR images scanned by MR systems. Furthermore, we compared the efficacy of the MSR technique in

enhancing the contrast of these MR images with other image processing techniques.

An algorithm for MSR as applied to human vision has been described in past literature [82, 85]. The MSR worked by compensating for lighting variations to approximate the human perception of a real scene. There were two methods to achieve this: (1) compare the psychophysical mechanisms between the human visual perceptions of a real scene and a captured image, and (2) compare the captured image with the measured reflectance values of the real scene.

To summarize, our method involved combining specific features of MSR with processes of SSR, in which the center/surround operation was a Gaussian function. A narrow Gaussian distribution was used for the neighboring areas of a pixel (which was regarded as the center). Space constants for Gaussian functions with scales of 15, 80, and 250 pixels in the surrounding area, as proposed by Jobson *et al.* [82, 85], were adopted in this study. The logarithm was then applied after surround function processing (i.e., two-dimensional spatial convolution). Next, appropriate gain and offset values were determined according to the retinex output and the characteristics of the histogram. These values were constant for all the images. This procedure yielded the MSR function.

#### **2.2.6. Phantom and animal magnetic resonance imaging (MRI)**

All experiments were performed at the Nuclear Magnetic Resonance (NMR) Center, and were carried out in accordance with the guidelines established by the Animal Care and Utilization Committee.

A single adult male Wistar rat weighing 275 g (National Laboratory Animal Center, Taiwan) was anesthetized using 2 % isoflurane and positioned on a stereotaxic holder. The body temperature of the animal was maintained using a warm-water circulation system.

For MR experiments, images were captured on a Bruker BIOSPEC BMT 47/40 spectrometer (Bruker GmbH, Ettlingen, Germany), operating at 4.7 Tesla (200 MHz),

equipped with an actively shielded gradient system (0 ~ 5.9 G/cm in 500 ms). A 20-cm volume coil was used as the RF transmitter, and a 2-cm linear surface coil and the above volume coil were used separately as the receiver. Coronal T2-weighted images of the phantom – comprising a 50-ml plastic centrifuge tube filled with water and an acrylic rod – and the rat brain were acquired using RARE sequences with a repetition time of 4000 ms, an echo time of 80 ms, a field of view of 3 cm, a slice thickness of 1.5 mm, 2 repetitions, and an acquisition matrix of  $256 \times 256$  pixels.

### 2.2.7. Peak Signal-to-Noise Ratio and Contrast-to-Noise Ratio Analysis

The PSNR [88] and contrast-to-noise ratio (CNR) were commonly used performance indices in image processing [12, 14]. The PSNR was given by

$$PSNR = 20 \log \frac{I_{peak}}{\sqrt{\sum_{k,l} \{y(k,l) - m(k,l)\}^2 / (K \cdot L)}}, \quad (2.14)$$

where  $y(k, l)$  and  $m(k, l)$  were the enhanced and original images of size  $K$  and  $L$  respectively, and  $I_{peak}$  was the maximum magnitude of images [88]. The CNR was given by

$$CNR = \frac{E[P_{jk}^d] - E[P_{jk}^u]}{\sqrt{\frac{Var(P_{jk}^d) + Var(P_{jk}^u)}{2}}}, \quad (2.15)$$

where  $P_{jk}^d$  and  $P_{jk}^u$  were the gray levels,  $E[P_{jk}^d]$  and  $E[P_{jk}^u]$  were the means, and  $Var(P_{jk}^d)$  and  $Var(P_{jk}^u)$  were the variances of the  $(j, k)$ th pixel in the enhanced and original images, respectively [12, 14].

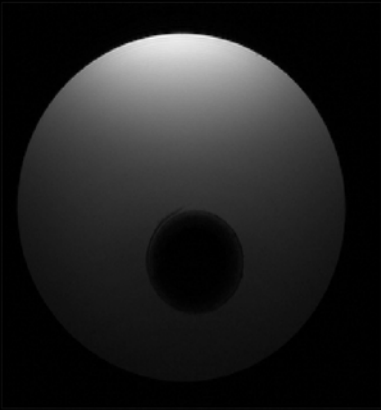
## 2.3. Experimental results

### 2.3.1. Results of phantom image

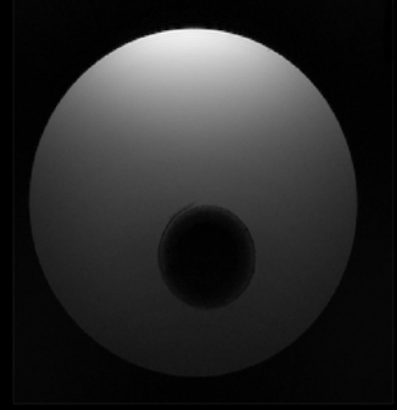
The performance of our retinex algorithm was assessed by determining the parameters for a test series of MR images of the phantom, with dimensions of  $256 \times 256$  pixels and 16-bit quantization. The dynamic-range compression and brightness constancy were determined in the MR images of the test series, based on postprocessing by the retinex method.

Figure 2.2 showed the results of using SSR and MSR to correct for the inhomogeneity of an MR image of the phantom. The original MR image was shown in Figure 2.2(a), which exhibited inhomogeneity, nonuniformity, low brightness, and a large dynamic range. SSR with a scale of every 10 pixels between 0 and 255 was used to analyze the series of phantom images. SSR with a scale of 15 pixels was also applied in this test. Figure 2.2(b), (c), and (d) illustrated the successful reductions in intensity inhomogeneity of the phantom images using SSR with scales of 15, 80, and 250 pixels respectively. The images in Figure 2.2(b), (c), and (d) showed dynamic-range compressions and brightness were large, moderate, and small, respectively, which indicated the dynamic-range compression increased when the SSR scale decreased. Figure 2.2(e) showed the image obtained from MSR by combining three scales of SSR weightings ( $\omega_n = 1/3$ ,  $n = 1, 2, \text{ and } 3$ ), where the three scales of SSR were 15, 80, and 250 pixels as used by Jobson *et al.* [82, 85]. The images obtained from the retinex algorithms were of higher quality than the original phantom image. Also, Figure 2.2(f) showed an MR image captured by a volume coil as a receiver with the same MR imaging procedures and parameters. Comparison of Figure 2.2(e) and (f) revealed that MSR successfully corrected the original MR phantom image.

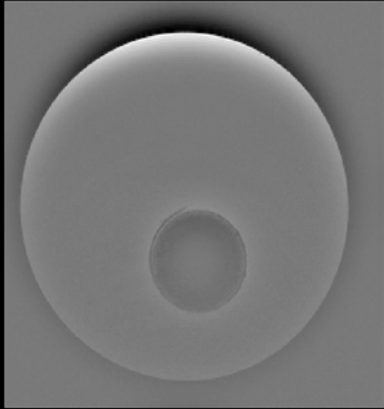
**(a)**



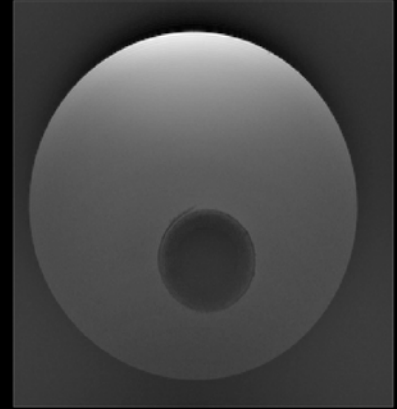
**(d)**



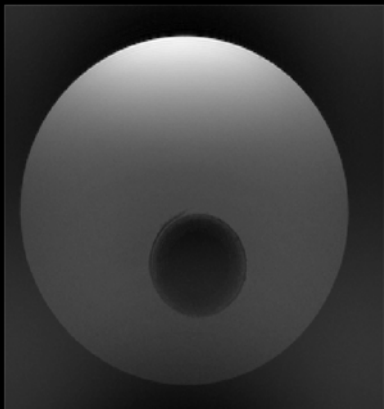
**(b)**



**(e)**



**(c)**



**(f)**

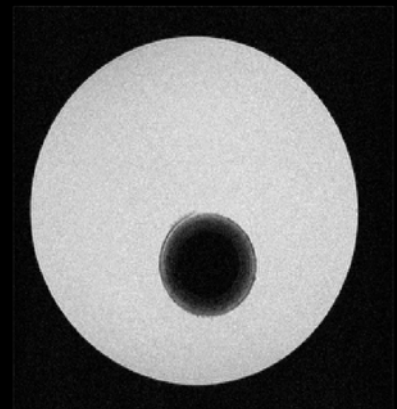


**Figure 2.2** Corrected MR images of a phantom demonstrating the performance of retinex. (a) The original MR image. (b) Image obtained from SSR with scale of 15 pixels. (c) Image obtained from SSR with scale of 80 pixels. (d) Image obtained from SSR with scale of 250 pixels. (e) Image obtained from MSR with three combined scales of SSR weightings ( $\omega_n = 1/3$ ,  $n = 1, 2$ , and  $3$ ). (f) MR image captured by a volume coil.

### 2.3.2. Results of animal image

In Figure 2.3, results of applying SSR and MSR to adjust a rat brain MR image were shown. Figure 2.3(a) showed the original MR image, which was one of 28 coronal brain slices. Figure 2.3(b), (c), and (e) showed the images obtained from SSR with scales of 15, 80, and 250 pixels respectively, with dynamic-range compressions that are large, moderate, and small; and brightness variations that are small, moderate, and large respectively. The images obtained from retinex demonstrated better visual rendition than that of the original MR image in Figure 2.3(a). The background of the original brain MR image was blurred, and its brightness contrast and dynamic range were poor. Figure 2.3(d) was the image obtained from MSR, displaying its strength of combining small, moderate, and large scales of SSR with the same weightings of  $\omega_n = 1/3$  ( $n = 1, 2$ , and  $3$ ). Figure 2.3(f) showed an MR image captured by a volume coil with the same MR imaging procedure, it had better homogeneity than the image obtained by surface coils, yet the resolution was lower. Figure 2.3(g) was enlarged ( $\times 5$ ) from dotted-line block of the original image in Figure 2.3(a), showing the deep brain structure subimage, the details in the medial forebrain bundle (MFB) and mammillothalamic tract (MT) regions were not clear and inhomogeneous. Figure 2.3(h) shows the MR image enlarged ( $\times 5$ ) from dotted-line block of Figure 2.3(d) from MSR, regions (MFB and MT) circled with dotted-curve demonstrated better homogeneity and clarity. Figure 2.3(h) exhibits clearer deep

anatomical structures from MSR than Figure 2.3(g) from original image.

The MSR clearly improved the quality, relative to that of the original MR image. Comparing among the original MR image, the image captured by a volume coil and the image obtained from the retinex algorithm revealed that the last method showed the best performance in terms of brightness, dynamic-range compression, and overall visual rendition.





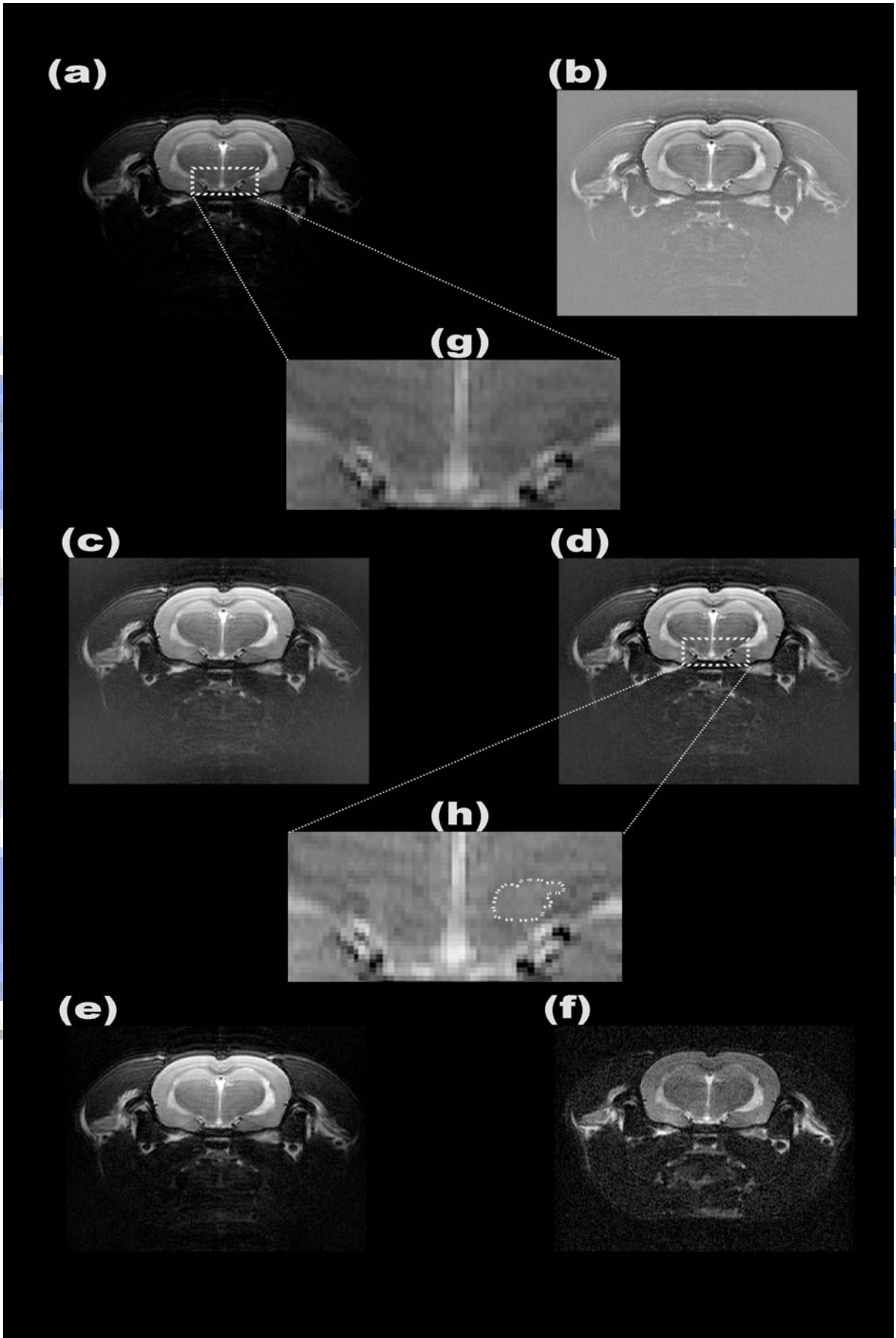


**Figure 2.3** Performance of the retinex was demonstrated with adjusted MR images of a coronal section of the rat brain. (a) The original MR image. (b) Image obtained from SSR with scale of 15 pixels. (c) Image obtained from SSR with scale of 80 pixels. (d) Image obtained from MSR with three combined scales of SSR weightings ( $\omega_n = 1/3$ ,  $n = 1, 2$ , and 3). (e) Image obtained from SSR with scale of 250 pixels. (f) MR image captured by a volume coil. (g) A 500% enlargement from the dotted-line block area in (a). The enlargement exhibits areas of tissue inhomogeneity within the deep brain structures. (h) The enlarged medical forebrain bundle (MFB), from dotted-line block of (d). The MFB was more clearly differentiated from other structures and the homogeneity of the circled region can be guaranteed.

### **2.3.3. Comparisons of histogram equalization, local histogram equalization, and a wavelet-based algorithm with multiscale retinex**

The effectiveness of the retinex algorithm was compared with a phantom image captured by MR imaging systems, using histogram equalization, local histogram equalization, and a wavelet-based algorithm.

In Figure 2.4(a), the image was obtained with histogram equalization, and Figure 2.4(b) showed the image obtained from local histogram equalization with a local region of 128×128 pixels. Both techniques resulted in blurred edges and poor contrast. A large amount of noise was still present in Figure 2.4(a) and (b), with the performance of local histogram equalization being worse than that of histogram equalization. Figure 2.4(c) showed the image processed by the wavelet-based algorithm [17, 18], indicating the presence of some noise. In Figure 2.4(d) and (e), the images were obtained from MSR with combined 15-pixel small-scale SSR weightings of  $\omega_1 = 3/5$  and  $4/6$ ; 80-pixel moderate-scale SSR weightings of  $\omega_2 = 1/5$  and  $1/6$ ; and 250-pixel large-scale SSR weightings of  $\omega_3 = 1/5$  and  $1/6$  respectively. Figure 2.4(f)

showed the image obtained from MSR with combined 10-pixel small-scale SSR weightings of  $\omega_1 = 3/5$ ; 60-pixel moderate-scale SSR weightings of  $\omega_2 = 1/5$ ; and 220-pixel large-scale SSR weightings of  $\omega_3 = 1/5$ . All phantom figures in Figure 2.4 displayed clear deep structures and edges. The MSR algorithm exhibited better visual rendition than histogram equalization, local histogram equalization, and the wavelet-based algorithm. The performance of MSR was also compared with those of histogram equalization, local histogram equalization, and the wavelet-based algorithm on an MR image of rat brain.



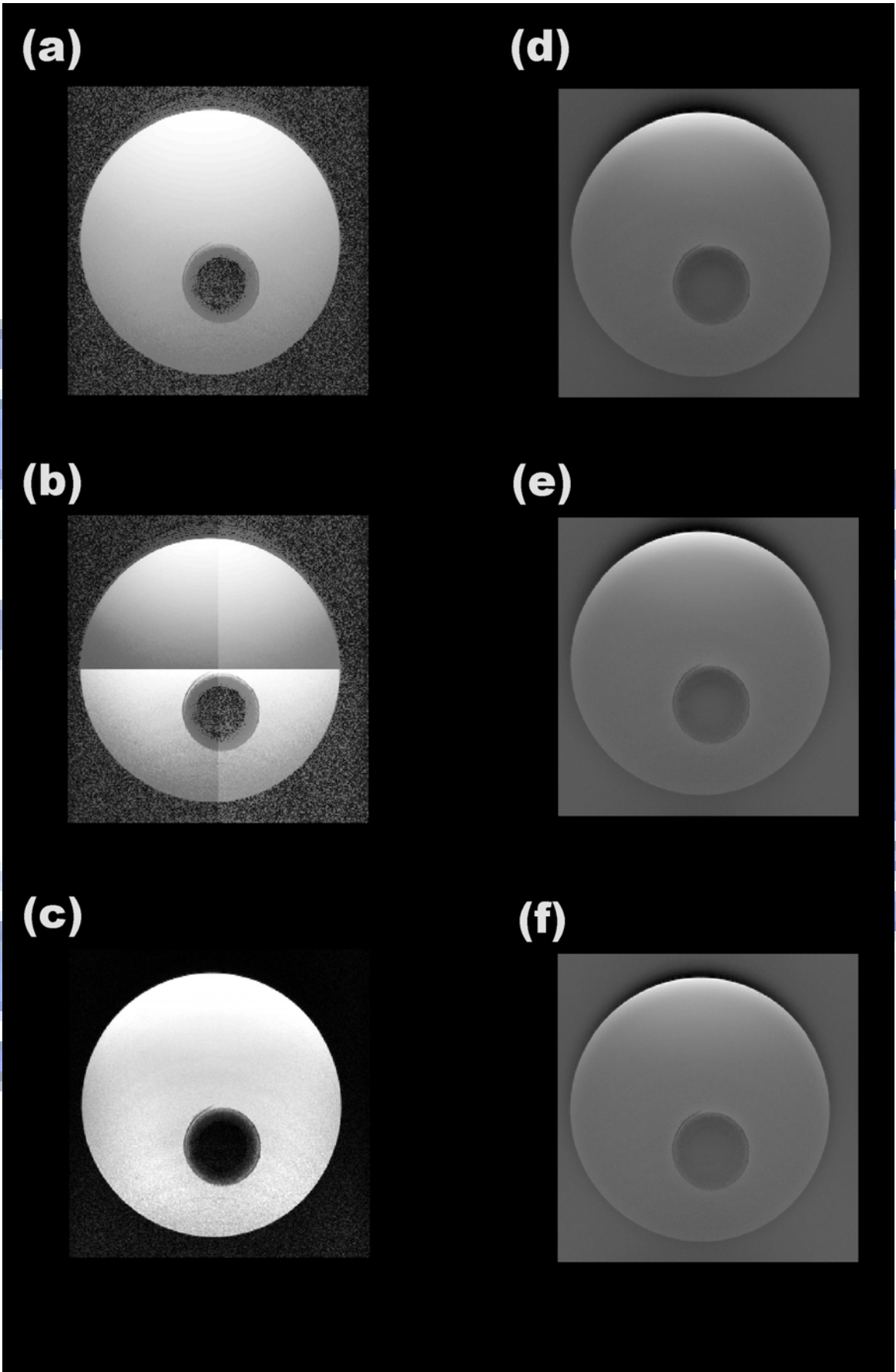


**Figure 2.4** Corrected MR images of a phantom, obtained via four methods. (a) MR image obtained from histogram equalization. (b) MR image obtained from local histogram equalization. (c) MR image obtained with the wavelet-based algorithm. (d) and (e) MR images from MSR with 15-pixel, 80-pixel, and 250-pixel;  $\omega_1 = 3/5$  and  $4/6$ ,  $\omega_2 = 1/5$  and  $1/6$ , and  $\omega_3 = 1/5$  and  $1/6$  respectively. (f) MR image from MSR with 10-pixel, 60-pixel, and 220-pixel;  $\omega_1 = 3/5$ ,  $\omega_2 = 1/5$ , and  $\omega_3 = 1/5$  respectively.

Figure 2.5(a) showed the corrected image obtained with histogram equalization, and Figure 2.5(b) showed the image obtained from local histogram equalization with a local region of  $128 \times 128$  pixels. Both techniques resulted in blurred edges and poor contrast. A large amount of noise was still present in Figure 2.5(a) and (b), with the performance of local histogram equalization being worse than that of histogram equalization. In Figure 2.5(c), the image was processed by the wavelet-based algorithm [17, 18], resulting in many artifacts. Figure 2.5(d) showed the image corrected by MRS with configuration of 15-pixel small-scale SSR weightings of  $\omega_1 = 2/4$  (high brightness), 80-pixel moderate-scale SSR weightings of  $\omega_2 = 1/4$  (moderate brightness), and 250-pixel large-scale SSR weightings of  $\omega_3 = 1/4$  (low brightness). Figure 2.5(e) showed the image corrected by MRS with configuration of 10-pixel small-scale SSR weightings of  $\omega_1 = 1/3$  (high brightness), 60-pixel moderate-scale SSR weightings of  $\omega_2 = 1/3$  (moderate brightness), and 220-pixel large-scale SSR weightings of  $\omega_3 = 1/3$  (low brightness). Figure 2.5(f) showed the image corrected by MRS with configuration of 10-pixel small-scale SSR weightings of  $\omega_1 = 2/6$  (high brightness), 60-pixel moderate-scale SSR weightings of  $\omega_2 = 3/6$  (moderate brightness), and 220-pixel large-scale SSR weightings of  $\omega_3 = 1/6$  (low brightness). The dynamic compression, brightness variation, and overall rendition were better for MSR that combined three scales of SSR weightings than those for histogram equalization, local histogram equalization, or the wavelet-based algorithm alone. All rat brain figures in Figure 3.5 displayed clear deep anatomy structures and edges.

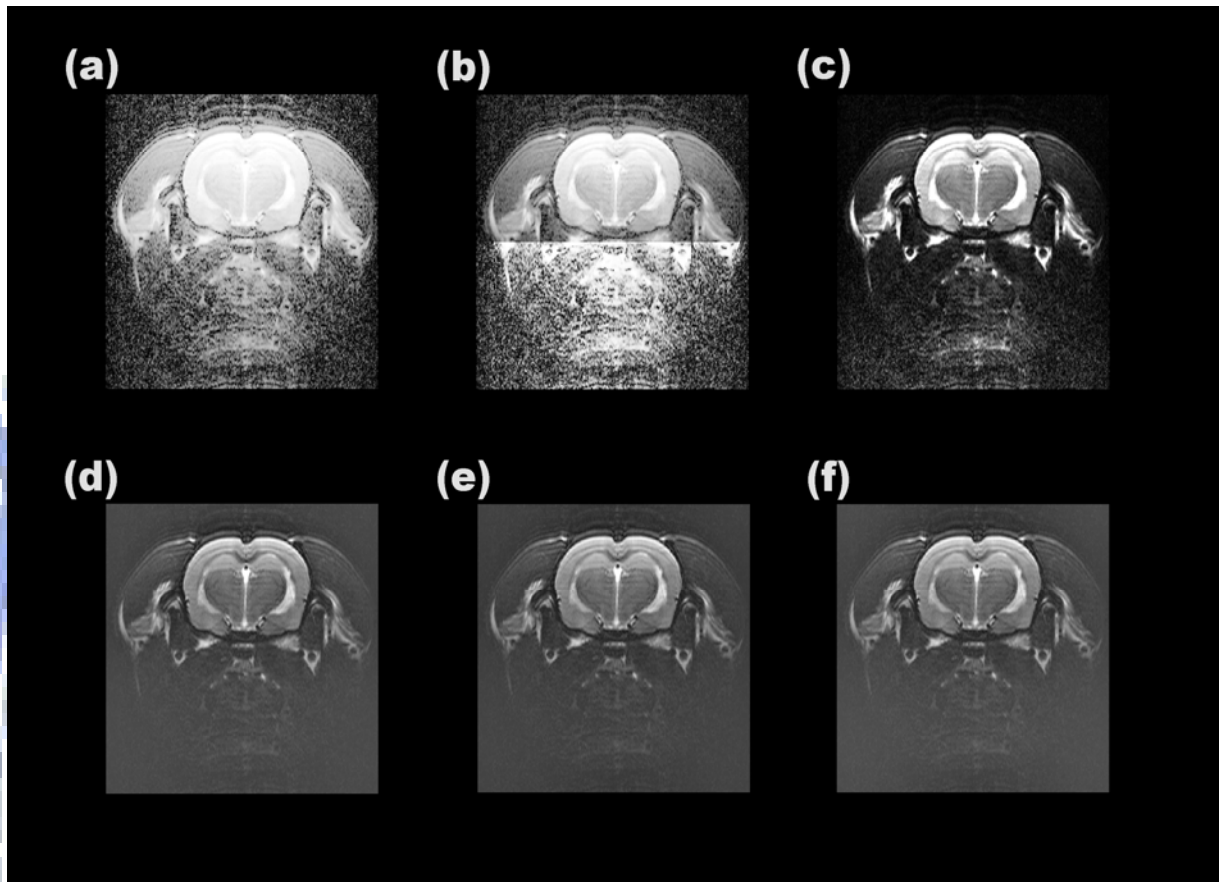


**Figure 2.5** Corrected MR images of a rat brain obtained from four algorithms. (a) MR image obtained from histogram equalization. (b) MR image obtained from local histogram equalization. (c) MR image obtained from the wavelet-based algorithm. (d) MR image obtained from MSR, with 15-pixel, 80-pixel, and 250-pixel;  $\omega_1 = 2/4$ ,  $\omega_2 = 1/4$ , and  $\omega_3 = 1/4$  respectively. (e) and (f) MR images obtained from MSR with 10-pixel, 60-pixel, and 220-pixel;  $\omega_1 = 1/3$  and  $2/6$ ,  $\omega_2 = 1/3$  and  $3/6$ , and  $\omega_3 = 1/3$  and  $1/6$  respectively.

#### 2.3.4. Results of peak signal-to-noise ratio and contrast-to-noise ratio analysis

Obtaining MR images of the highest possible clarity is crucial to effective structural brain imaging. The quality of images obtained from histogram equalization, local histogram equalization, the wavelet-based algorithm, and retinex can be quantified using appropriate

indices. The values of PSNR and CNR for the phantom images obtained in the present study with the four correction methods were listed in Table 2.1, where higher values indicate images of higher quality. As shown on the table, the use of SSR increased PSNR but decreased CNR. In Tables 2.1 and 2.2, MSR showed combined small-, moderate-, and large-scale weightings of 15, 80, and 250 pixels respectively, and MSR<sub>2</sub> indicated combined small-, moderate-, and large-scale weightings of 10, 60, and 220 pixels respectively. In Table 1, MSR with  $\omega_1 = 3/5$ ,  $\omega_2 = 1/5$ , and  $\omega_3 = 1/5$ ; MSR with  $\omega_1 = 4/6$ ,  $\omega_2 = 1/6$ , and  $\omega_3 = 1/6$ ; and MSR<sub>2</sub> with  $\omega_1 = 2/4$ ,  $\omega_2 = 1/4$ , and  $\omega_3 = 1/4$ , and MSR<sub>2</sub> with  $\omega_1 = 3/5$ ,  $\omega_2 = 1/5$ , and  $\omega_3 = 1/5$  resulted in higher values of PSNR and CNR than histogram equalization, local histogram equalization, and the wavelet-based algorithm.

The values of PSNR and CNR for animal images were listed in Table 2.2. Whilst histogram equalization and local histogram equalization resulted in high CNR values, the low PSNR values resulted in many noise artifacts. The wavelet-based algorithm resulted in some noise, as indicated by the lower CNR value. MSR with  $\omega_1 = 1/3$ ,  $\omega_2 = 1/3$ , and  $\omega_3 = 1/3$ ; MSR with  $\omega_1 = 2/4$ ,  $\omega_2 = 1/4$ , and  $\omega_3 = 1/4$ ; MSR with  $\omega_1 = 1/4$ ,  $\omega_2 = 2/4$ , and  $\omega_3 = 1/4$ ; MSR with  $\omega_1 = 1/5$ ,  $\omega_2 = 3/5$ , and  $\omega_3 = 1/5$ ; MSR<sub>2</sub> with  $\omega_1 = 1/3$ ,  $\omega_2 = 1/3$ , and  $\omega_3 = 1/3$ ; MSR<sub>2</sub> with  $\omega_1 = 1/4$ ,  $\omega_2 = 2/4$ , and  $\omega_3 = 1/4$ ; and MSR<sub>2</sub> with  $\omega_1 = 2/6$ ,  $\omega_2 = 3/6$ , and  $\omega_3 = 1/6$  resulted in higher values of PSNR and CNR than histogram equalization, local histogram equalization, and the wavelet-based algorithm.

**Table 2.1** Comparisons of PSNR and CNR for phantom images obtained from retinex algorithms with those obtained from histogram equalization, local histogram equalization, and the wavelet-based algorithm.

Algorithm	PSNR (dB)	CNR
SSR (scale = 15 pixels)	8.4850	2.4007
SSR (scale = 80 pixels)	17.7173	0.6783
SSR (scale = 250 pixels)	27.1259	0.1848
MSR ( $\omega_1 = 1/3, \omega_2 = 1/3, \omega_3 = 1/3$ )	15.0569	1.0086
MSR ( $\omega_1 = 2/4, \omega_2 = 1/4, \omega_3 = 1/4$ )	12.9146	1.3437
MSR ( $\omega_1 = 1/4, \omega_2 = 2/4, \omega_3 = 1/4$ )	15.6836	0.9224
MSR ( $\omega_1 = 1/4, \omega_2 = 1/4, \omega_3 = 2/4$ )	17.0583	0.7798
MSR ( $\omega_1 = 3/5, \omega_2 = 1/5, \omega_3 = 1/5$ )	11.8356	1.5544
MSR ( $\omega_1 = 4/6, \omega_2 = 1/6, \omega_3 = 1/6$ )	11.1821	1.6973
SSR (scale = 10 pixels)	7.7921	2.6780
SSR (scale = 50 pixels)	14.1465	1.0492
SSR (scale = 60 pixels)	14.6290	1.0056
SSR (scale = 120 pixels)	22.4192	0.3782
SSR (scale = 200 pixels)	26.5111	0.2121
SSR (scale = 220 pixels)	26.8245	0.1987
MSR <sub>2</sub> ( $\omega_1 = 1/3, \omega_2 = 1/3, \omega_3 = 1/3$ )	13.7010	1.2132
MSR <sub>2</sub> ( $\omega_1 = 2/4, \omega_2 = 1/4, \omega_3 = 1/4$ )	11.8239	1.5718
MSR <sub>2</sub> ( $\omega_1 = 3/5, \omega_2 = 1/5, \omega_3 = 1/5$ )	10.8591	1.7957
Histogram equalization	7.7978	1.5199
Local histogram equalization	7.4683	1.5236
Wavelet-based algorithm	6.0785	1.1225



**Table 2.2** Comparisons of PSNR and CNR for animal images obtained from retinex algorithms with those obtained from histogram equalization, local histogram equalization, and the wavelet-based algorithm.

Algorithm	PSNR (dB)	CNR
SSR (scale = 15 pixels)	7.5729	3.8213
SSR (scale = 80 pixels)	16.7675	0.9751
SSR (scale = 250 pixels)	21.3775	0.3568
MSR ( $\omega_1 = 1/3, \omega_2 = 1/3, \omega_3 = 1/3$ )	13.8641	1.5566
MSR ( $\omega_1 = 2/4, \omega_2 = 1/4, \omega_3 = 1/4$ )	11.8648	2.0922
MSR ( $\omega_1 = 1/4, \omega_2 = 2/4, \omega_3 = 1/4$ )	14.5375	1.4031
MSR ( $\omega_1 = 1/4, \omega_2 = 1/4, \omega_3 = 2/4$ )	15.5348	1.2157
MSR ( $\omega_1 = 1/5, \omega_2 = 3/5, \omega_3 = 1/5$ )	14.9590	1.3135
SSR (scale = 10 pixels)	7.0382	4.2851
SSR (scale = 60 pixels)	13.6414	1.5104
SSR (scale = 220 pixels)	21.2816	0.3752
MSR <sub>2</sub> ( $\omega_1 = 1/3, \omega_2 = 1/3, \omega_3 = 1/3$ )	12.6385	1.8747
MSR <sub>2</sub> ( $\omega_1 = 1/4, \omega_2 = 2/4, \omega_3 = 1/4$ )	12.8957	1.7817
MSR <sub>2</sub> ( $\omega_1 = 1/4, \omega_2 = 1/4, \omega_3 = 2/4$ )	14.4219	1.4399
MSR <sub>2</sub> ( $\omega_1 = 2/6, \omega_2 = 3/6, \omega_3 = 1/6$ )	11.7580	2.1157
Histogram equalization	6.4478	1.8631
Local histogram equalization	6.3042	1.8807
Wavelet-based algorithm	11.8304	0.8571

## 2.4. Discussions

The inhomogeneity and anatomic-structure blurring found in images captured by surface receiving coils was due to variations in image brightness. The inhomogeneities of MR images were very low frequency components in frequency domain of images. The retinex algorithm [82, 85] especially performed to remove the very low frequency components of images by an estimator constructed with a similar lowpass filter from a Gaussian surround function as described in Equation (2.11) for the purpose of correction of the inhomogeneous MR images. The variations of inhomogeneity in MR images received with surface coils were shown in Figure 2.2(a) and Figure 2.3(a). Hence, MR postprocessing techniques were crucial in improving the structural details and homogeneity of such brain images. In the present study, we proposed an easy, low-cost software-based method to solve these problems, also avoiding expensive charges to the imaging hardware. Our retinex algorithm successfully corrected a nonuniform grayscale, enhanced contrast, corrected inhomogeneity, and clarified the MFB and MT areas in deep brain structures of MR images captured by surface coils (see Figure 2.3).

For evaluating the performance of correction of inhomogeneous MR images, the two indices, PSNR and CNR [12, 14, 88], were proposed to compare the performance of correction of inhomogeneous MR images using retinex algorithm with other correction algorithms. The retinex algorithm improved the quality of phantom images in terms of visual rendition and dynamic range compression, with reduced errors and noise, and correspondingly higher PSNR and CNR values. Similar results were found for animal images, except that PSNR increased whereas CNR decreased (see Table 2.1 and Table 2.2). This may indicate that retinex processing of animal data should combine with appropriate reference objects.

For comparison, consider the approach proposed by Jobson *et al.* [82, 85]. The MR images obtained with the retinex algorithm were also better than those obtained with histogram equalization, local histogram equalization, and the wavelet-based algorithm, in

terms of dynamic-range compression, brightness constancy, and overall visual rendition. The PSNR and CNR values were also higher for retinex than for the other correction algorithms. Furthermore, the advantages of the retinex were that the weightings of MSR and scales of SSR could be modulated to improve image correction and contrast enhancement performance. The optimal weightings of MSR and the best combination between weightings of MSR and scales of SSR may be further studied in the future.



## Chapter 3 Segmentation of Brain MR images Using a Classification and Regression Tree (CART)

### 3.1. Introduction

Since the hardware improvement through coil sensitivities and the performance of transmitter devices to reduce imaging noise and inhomogeneity are more expensive and clear anatomical structures remain difficult to be obtained, a low cost technique to obtain better MR brain structures is worth studying. In this Chapter, we will therefore propose an easy implementation of automatic segmentation of the GM, WM, and CSF in brain MR images to obtain clearly anatomical structures. The brain tissue segmentation method in this experiment is a classification and regression tree (CART).

In image processing, spatial features (also called spatial information) defined as the combination of image intensities and in-plane information in two coordinate systems (Euclidean coordinates  $(x, y)$  or polar coordinates  $(r, \theta)$ ) in images have generally been used to extract the spatial features of MR images [43, 44]. The spatial gray information was defined in the present study by combining neighboring pixel intensities, as described in Section 3.2.1. The wavelet-transform spatial information obtained from each local area was also used in the present study. The performances of the three types of spatial information were compared by using decision tree algorithms in this study. Decision trees are easily implemented according to the attributes of a subset in the entire data set, and provide rapid analysis. Decision trees have been widely used in the analysis of symbolic data sets, and also to classify EEG spatial patterns [89] and the different regions of digital images sensed remotely [90]. The present study compared with the performance of segmentation based on an automatic decision tree with different types of spatial information– the general gray level ( $G$ ), spatial gray level ( $S$ ), and two-dimensional wavelet transform ( $W$ ) – to improve the accuracy

of segmentation in MR images.

Several studies have improved coil sensitivities and the performance of transmitter devices [57–60], but it remains difficult and expensive to reduce imaging noise and inhomogeneity through hardware improvements. For the purpose of these studies was to obtain better anatomical structures of MR images. A low cost technique to obtain MR brain structures is valuable to study. Thus, the ability through software improvements to discriminate different tissue characteristics of brain structures is increasing in importance.

## **3.2. Materials and methods**

### **3.2.1. Image preprocessing for spatial information**

Noise and RF inhomogeneities often reduce the quality of MR images, and so their bad effects need to be reduced by image preprocessing manipulation to increase the segmentation accuracy.

Spatial information (Spatial features) were extracted from every MR image pixel location and used as the input for the segmentation algorithm for image preprocessing. The spatial features used in the present study were:  $G$ ,  $S$ ,  $W$ ,  $x$ ,  $y$ ,  $r$ , and  $\theta$ , where  $G$  represents the gray level intensity of every pixel,  $S$  the spatial gray level of every pixel,  $W$  the coefficients of the wavelet transform,  $(x, y)$  Euclidean coordinates, and  $(r, \theta)$  polar coordinates. The spatial features of the general gray level, spatial gray level, and wavelet transform were combined in Euclidean coordinates  $(x, y)$  or polar coordinates  $(r, \theta)$  by image preprocessing. Noise and RF inhomogeneities often reduced the quality of MR images, such that their impact on segmentation accuracy needed to be reduced by image manipulation.

The general gray level represents the intensity of each pixel for MR image segmentation. The use of more spatial features in an image is considered to improve the accuracy of image segmentation. The spatial gray ( $S$ ) level is given as

$$S(x, y) = \sum_{i=1}^n \omega_i g_i(x, y), \quad (3.1)$$

which is the sum of combined weighting  $\omega_i$  and gray level  $g_i(x, y)$  of pixel  $i$  on the neighboring area. The neighboring area is shown in Figure 3.1(a), which depicts the five neighbor systems used in this study, wherein the gray level weighting at the center pixel with the nearest four pixels produced  $n = 5$  and  $\omega_i = \frac{1}{5}$ .

The wavelet transform ( $W$ ) of the spatial features used in this study was the coefficient of the wavelet transform transferred from nine gray levels of each local area to represent the wavelet spatial features of the center pixel for every location. The scaled and translated basis functions are defined as

$$\varphi_{j,m,n}(x, y) = 2^{j/2} \varphi(2^j x - m, 2^j y - n), \quad (3.2)$$

$$\psi_{j,m,n}(x, y) = 2^{j/2} \psi(2^j x - m, 2^j y - n), \quad i = \{H, V, D\}, \quad (3.3)$$

where the index  $i$  identifies the directional wavelets in  $\psi^H(x, y) = \psi(x)\varphi(y)$ ,  $\psi^V(x, y) = \varphi(x)\psi(y)$ , and  $\psi^D(x, y) = \psi(x)\psi(y)$ . The discrete wavelet transform of function  $g(x, y)$  of size  $M \times N$  is then

$$W_\varphi(j_0, m, n) = \frac{1}{\sqrt{MN}} \sum_{x=0}^{M-1} \sum_{y=0}^{N-1} g(x, y) \varphi_{j_0, m, n}(x, y), \quad (3.4)$$

$$W_\psi^i(j_0, m, n) = \frac{1}{\sqrt{MN}} \sum_{x=0}^{M-1} \sum_{y=0}^{N-1} g(x, y) \psi_{j_0, m, n}^i(x, y), \quad i = \{H, V, D\}, \quad (3.5)$$

where the  $W_\varphi(j_0, m, n)$  coefficients define an approximation of  $g(x, y)$  at scale  $j_0$ .

The  $W_\psi^i(j_0, m, n)$  coefficients add horizontal, vertical, and diagonal details for scales  $j \geq j_0$  [72]. The obtained coefficients were transferred by wavelet from the local area to represent

the spatial features of the central pixel. Local areas were generated from every nine pixels in each MR image, as shown in Figure 3.1(b).

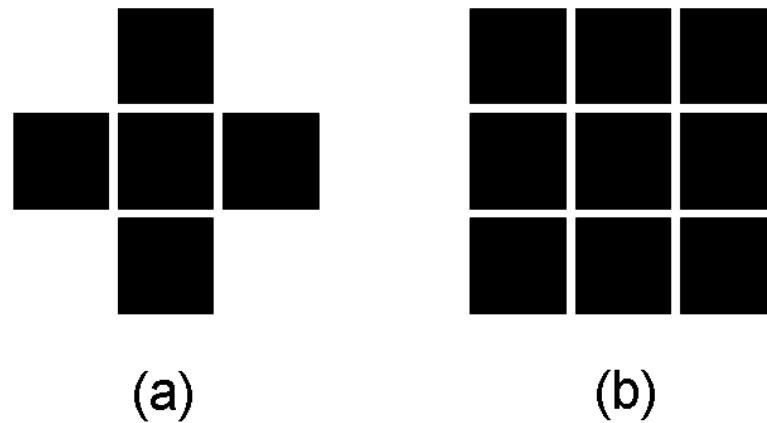


**Figure 3.1** Local area of each spatial feature. (a) Local area of the spatial gray level. (b) Local area of the wavelet transforms.

### 3.2.2. Segmentation

The proposed automatic decision-tree segmentation method used in this study was the classification and regression tree (CART) presented by Breiman *et al.* [91] to model the prediction tree by statistical analysis, considering outcome variables and decision questions to assess the prediction accuracy. The method protocol is described below.

### 3.2.3. Decision tree classification

In a classification tree, the decision tree classification structure is constructed so as to

distinguish different classes through statistical analysis [89, 92]. Decision trees can classify multidimensional spatial data through recursive partitioning steps. Each vector consisting of  $N$  sampled data in an  $M$ -dimensional space is given by

$$\{x_m\}, \quad m=1, \dots, M, \quad (3.6)$$

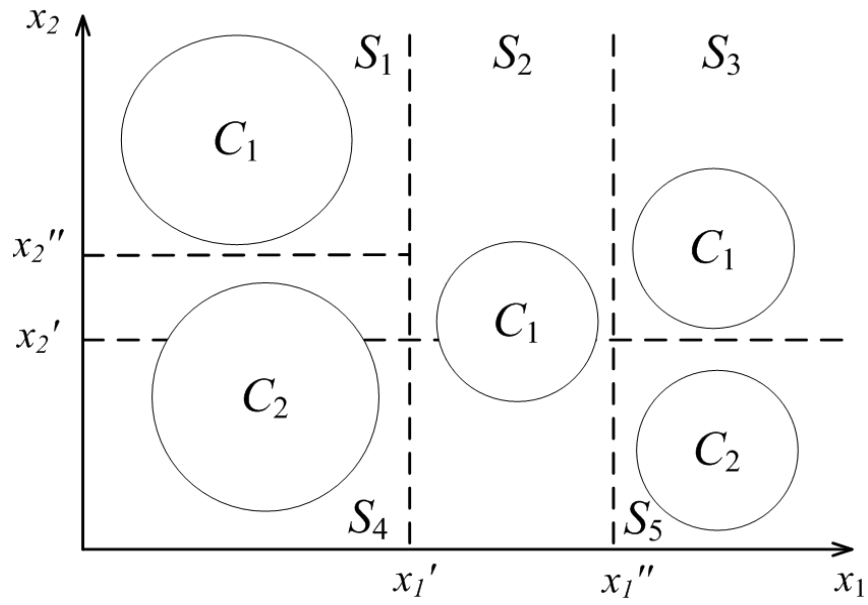
where  $M$  represents the dimension of the data space, and the class label in the data space is

$$j \in \{1, \dots, J\}. \quad (3.7)$$

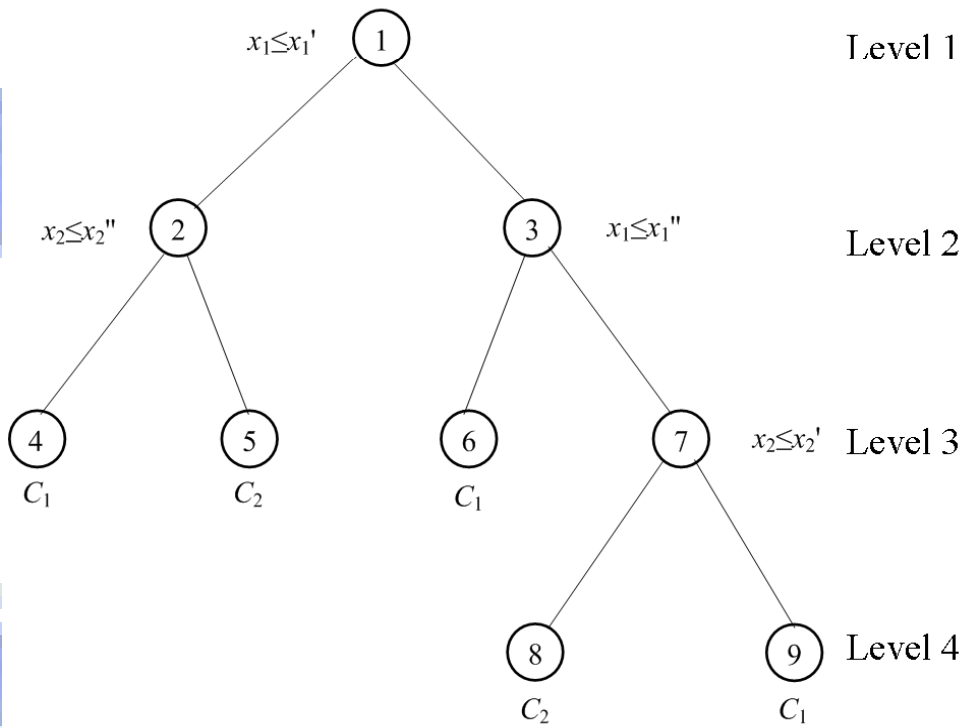
The subspaces can be illustrated easily to maximize the overall class separation for the  $M$ -dimensional spatial data set. The class separation is maximized during the partitioning step, and can be subsequently processed as the basis for further partitioning to the  $M$ -dimensional spatial data set. A two-space and two-class example is described as follows for decision-tree classification. The distributions of the two spatial data sets are shown in Figure 2.2. The first partitioning step can perfectly partition the entire data set along horizontal line  $x_1$  with vertical dashed line  $x_1 = x_1'$  into the first two subspaces: subspace 1 is  $S_1 \cup S_4$ , and subspace 2 is  $(S_2 \cup S_3 \cup S_5)$ . Subspace 1 can also be partitioned along vertical line  $x_2$  with horizontal dashed line  $x_2 = x_2''$  into two subspaces  $S_1$  and  $S_4$ . Data set classes 1 and 2 can be maximally segmented from subspaces  $S_1$  and  $S_4$ . Subspace 2 can then be partitioned along horizontal line  $x_1$  with vertical dashed line  $x_1 = x_1''$  into two subspaces  $S_2$  and  $S_3 \cup S_5$ . Next, data set class 1 can be maximally segmented from subspace  $S_2$  with vertical dashed lines  $x_1 = x_1'$  and  $x_1 = x_1''$ . Finally, subspace  $S_3 \cup S_5$  can be partitioned along vertical line  $x_2$  with horizontal dashed line  $x_2 = x_2'$  into two subspaces  $S_3$  and  $S_5$ . Data set classes 1 and 2 can be maximally segmented from subspaces  $S_3$  and  $S_5$ . Figure 3.2(a) clearly shows the entire partition of the two spatial data sets. The partitioning procedure can be displayed as a decision-tree structure of a binary tree due to the maximal class separation of the partitioning



steps. The decision-tree structures of the two spatial data sets are shown in Figure 3.2(b). A root node is displayed at the top of the tree graph for the first level, and is connected to other leaf nodes and branches. The root node of the decision tree corresponds to the entire data space, and the two spatial data sets are decided with a condition  $x_1 \leq x_1'$  that is similar to a binary or “yes/no” question for partitioning, which yields subspace 1 ( $S_1 \cup S_4$ ) and subspace 2 ( $S_2 \cup S_3 \cup S_5$ ). Next, partitions of the space are associated with descendant nodes of the root node in level 1. Subspace 1 in node 2 is partitioned by applying condition  $x_2 \leq x_2''$  to decide terminal node 4 for class 1 and node 5 with condition  $x_2 > x_2''$  for class 2. Next, partitioning for subspace  $S_2 \cup S_3 \cup S_5$  is decided by the condition  $x_1 > x_1'$ , which yields leaf node 3. Terminal node 6 for subspace  $S_2$  is decided by the condition  $x_1 > x_1''$ . The next partition for subspace  $S_3 \cup S_5$  in leaf node 7 is applied with condition  $x_2 \leq x_2'$  to decide terminal node 8 for class 2 in subspace  $S_5$  and terminal node 9 with condition  $x_2 > x_2'$  for class 1 in subspace  $S_3$ .



(a)



(b)

**Figure 3.2** Decision tree configuration: (a) example of the distribution of two subspaces from an entire space, and (b) structure of the corresponding decision-tree graph.

The connection mechanism is constructed using a Gini impurity function from the root node until the tree reaches the terminal nodes. Classification of decision-tree processes determines the condition of attributes in a top-down manner in the tree structure. The classification of a pattern begins at the root node, deciding the condition of the main attribute of the pattern. The connection mechanism then follows a similar link mechanism to the descendent nodes. All of these linking mechanisms are binary, and together they form the tree graph. This connection mechanism proceeds continuously until all the nodes are determined, when the class of each terminal node of the test pattern is decided.

### 3.2.4. Decision tree construction

Descendant nodes of greater purity are desired when constructing a decision tree, which is achieved by maximizing an impurity function. Descendant nodes have greater purity than ancestor nodes, and an impurity function  $\phi$  is defined based on a node  $N$  defined as [89]

$$i(N) = \phi(p(\omega_1 | N), \dots, p(\omega_j | N)), \quad (3.8)$$

where  $p(\omega_j | N)$  is the conditional probability for class  $\omega_j$  of node  $N$ . Impurity  $i(N)$  is maximal when a node  $N$  has an equal number of cases for all classes. In other words, a node is maximally pure when the node comprises a single category. The impurity function [91, 92] can be interpreted as a general variance impurity for two or more classes, which is the Gini impurity given by

$$i(N) = \sum_{i \neq j} p(\omega_i | N)p(\omega_j | N) = 1 - \sum_j p(\omega_j | N)p(\omega_j | N), \quad (3.9)$$

where  $p(\omega_i | N)$  and  $p(\omega_j | N)$  are the proportions of patterns for classes  $\omega_i$  and  $\omega_j$  at node  $N$ , respectively. The Gini impurity is 0 if all the patterns are of the same class. At the beginning of the root node, the CART calculates the node impurity with the Gini impurity function. All decision-tree nodes are decided by determining the best change in the impurity from the root node down to the terminal node, as shown in Figure 2.2. A node consisting of a

single class has the largest purity. Thus, the terminal node is then selected when the impurity of the node is 0. The largest impurity value is 1. The best change in impurity [28] is the difference between  $i(N)$  and a sum of the impurities of  $N_L$  and  $N_R$  that is given by

$$\Delta i(N) = i(N) - p_L i(N_L) - p_R i(N_R), \quad (3.10)$$

where  $N_L$  and  $N_R$  are the left and right descent nodes,  $i(N_L)$  and  $i(N_R)$  are their impurities, and  $p_L$  and  $p_R$  are their fractions of patterns at node  $N$ , respectively. The CART employs an iterative approach to decide the split at node  $N$  based on the best numerical change in the Gini impurity, which corresponds to the maximal class separation. At the beginning from the root node, the CART estimates the node impurity using the Gini impurity function of Equation (3.9). Each of these nodes is decided by maximizing  $\Delta i(N)$  and minimizing  $i(N)$ . This iterative approach produces the partitioning step with the highest purity at the terminal nodes. In other words, maximal class separation is equivalent to minimizing the misclassification of classes in the decision tree at node  $N$  [91, 92]. The Gini impurity function of Equation (3.9) evaluates the probability of misclassification at node  $N$ . A class in node  $N$  can be estimated through the rule of Equation (3.9) with conditional probability  $p(\omega_i | N)$  and  $p(\omega_j | N)$ . The conditional probability of node  $N$  can also be quantified using the rules of Equation (3.9). Finally, the entire decision-tree structures can be decided from the data set of the entire space by algorithmically applying these rules for constructing the decision tree.

### 3.2.5. Simulated data

Two types of simulated data were used in this study were: phantom MR images and simulated brain MR images. The phantom MR images were obtained from IBSR (<http://www.cma.mgh.harvard.edu/ibsr>). The phantom MR images comprised the circle center, circle ring, and background region, as shown in row 1 of Figure 3.3, with noise variations of

15 or 30 gray levels. We also added RF inhomogeneities of 20% and 40% to the two SNR phantom images. The variations in the gray levels due to noise and inhomogeneities that were added to a gold-standard phantom image are designated in Table 3.1. The simulated MR images obtained from BrainWeb were T1-weighted 3-mm-thick images with noise levels of 3%, 5%, 7%, 9%, and 15%. Furthermore, images with these noise levels combined with RF inhomogeneities of 20% and 40% were also obtained from BrainWeb to examine the performance of segmentation with spatial information of different qualities. An expert manually derived a gold-standard brain MR image with no noise or inhomogeneity from the original image. All of the simulated data were preprocessed to extract the spatial information and then segmented using the automatic decision-tree algorithm.

**Table 3.1** Designations of the original phantom images obtained by combining the noise levels and inhomogeneities parameters.

Designation	Combined noise level and inhomogeneities parameter
Var15	Noise variation = 15 gray levels
Var30	Noise variation = 30 gray levels
Var15RF20	Noise variation = 15 gray levels and 20% RF inhomogeneities
Var30RF20	Noise variation = 30 gray levels and 20% RF inhomogeneities
Var15RF40	Noise variation = 15 gray levels and 40% RF inhomogeneities
Var30RF40	Noise variation = 30 gray levels and 40% RF inhomogeneities

**Table 3.2** Designations of the original simulated MR images obtained by combining the noise levels and inhomogeneities parameters.

Designation	Combined noise level and inhomogeneities parameter
T1n3	Noise level = 3%
T1n5	Noise level = 5%
T1n7	Noise level = 7%
T1n9	Noise level = 9%
T1n15	Noise level = 15%
T1n3RF20	Noise level = 3% and 40% RF inhomogeneities
T1n5RF20	Noise level = 5% and 20% RF inhomogeneities
T1n7RF20	Noise level = 7% and 20% RF inhomogeneities
T1n9RF20	Noise level = 9% and 20% RF inhomogeneities
T1n15RF20	Noise level = 15% and 20% RF inhomogeneities
T1n3RF40	Noise level = 3% and 40% RF inhomogeneities
T1n5RF40	Noise level = 5% and 40% RF inhomogeneities
T1n7RF40	Noise level = 7% and 40% RF inhomogeneities
T1n9RF40	Noise level = 9% and 40% RF inhomogeneities
T1n15RF40	Noise level = 15% and 40% RF inhomogeneities

### 3.2.6. Accuracy rate of segmentation

The accuracy rate was used to evaluate the performance of segmentation in the present study and was calculated based on the overlap of the standard reference image (manually labeled by an expert) and a collection of segmentation results obtained with the proposed method. The accuracy rate was quantified as the overlap fraction [28, 44, 57, 55] and is defined as:

$$Accuracy \text{ rate} = \frac{Ref(k) \cap Seg(k)}{Ref(k)}, \quad (3.11)$$

which represents the accuracy rate of the segmented area in class  $k$  relative to the area in the standard reference image [44, 57]. Three classes of phantom MR images (circle center, circle ring, and background) and four classes of simulated brain MR images (GM, WM, CSF, and background) were segmented in this study. The numerator in Equation (3.11) represents the number of classified or intersection areas of voxels of class  $k$  between the segmented image and the standard image, while the denominator represents the area of voxels in class  $k$  in the standard image.

### 3.3. Experimental results

#### 3.3.1. Results of phantom image

All simulated phantom MR images with different SNRs and inhomogeneities (see Table 3.1) obtained from the IBSR website were segmented with spatial information  $(G, x, y)$ ,  $(S, x, y)$ ,  $(G, x, y, r, \theta)$ ,  $(S, x, y, r, \theta)$ ,  $(G, x, y, S, r, \theta)$ ,  $(W, x, y, G, r, \theta)$ , and  $(W, x, y, G, r, \theta, S)$ . Figure 3.3 shows the original phantom images with different SNRs and inhomogeneities, and the segmentation results obtained using a decision tree algorithm. The images in row 1 of Figure 3.3 are the original phantom images with noise variations and RF inhomogeneities of Var15, Var30, Var15RF20, Var15RF40, Var30RF20, and Var30RF40 (in columns 1 to 6, respectively), as listed in Table 3.1. The images in row 2 of Figure 3.3 correspond to those in row 1 segmented using the automatic decision tree with spatial information  $(S, x, y)$ . Euclidean coordinates  $(x, y)$  and polar coordinates  $(r, \theta)$  were also used for spatial information in this study. The images in row 3 of Figure 3.3 correspond to those in row 1 segmented using automatic decision tree with spatial information  $(S, x, y, r, \theta)$ . The images in row 4 of Figure

3.3 correspond to those in row 1 segmented using a decision tree with spatial information  $(G, x, y)$ .

The images segmented with spatial information  $(S, x, y)$  and  $(S, x, y, r, \theta)$  (rows 2 and 3 of Figure 3.3) show better performance than those segmented with spatial information  $(G, x, y)$ . Images with a noise variation of 30 gray levels and 40% RF inhomogeneities constituted a very large fraction of the source phantom images. The performance for images with Var30, Var30RF20, and Var30RF40 (row 4 of Figure 3.3) segmented with spatial information  $(G, x, y)$  is not clear. The segmentation of phantom MR images with Var15, Var30, Var15RF20, Var15RF40, Var30RF20, and Var30RF40 using a decision tree with spatial information  $(G, x, y, r, \theta)$ ,  $(G, x, y)$ ,  $(G, x, y, r, \theta)$ ,  $(G, x, y, S, r, \theta)$ ,  $(S, x, y)$ ,  $(W, x, y, G, r, \theta)$ , and  $(W, x, y, G, r, \theta, S)$  produced better performance. Figure 3.4 shows the average accuracy rate of phantom images with different SNRs and inhomogeneities segmented by a decision-tree algorithm with different spatial information. The average accuracy rates were averaged across all phantom image regions (circle ring, circle center, and background). The accuracy rate was evaluated by the OF index as described in Section 3.2.6. The average accuracy rates of segmentation for phantom images with Var15, Var30, Var15RF20, Var15RF40, Var30RF20, and Var30RF40 and segmentation spatial information  $(G, x, y, r, \theta)$ ,  $(G, x, y)$ ,  $(G, x, y, r, \theta)$ ,  $(G, x, y, S, r, \theta)$ ,  $(S, x, y)$ ,  $(W, x, y, G, r, \theta)$ , and  $(W, x, y, G, r, \theta, S)$ , are shown in Figure 3.4. The highest average accuracy rates of segmentation are in the range 0.9819–0.9999 for phantom images with Var15 and Var15RF20 segmented using a decision tree for all of the used spatial information. The higher average accuracy rates of segmentation are shown in Figure 3.4 for phantom images with Var15RF40 for all of the used spatial information. The accuracy rates of phantom images with Var30 and Var30RF20 segmented by a decision tree for spatial information  $(G, x, y, r, \theta)$ ,  $(G, x, y)$ ,  $(G, x, y, S, r, \theta)$ ,  $(S, x, y)$ ,  $(W, x, y, G, r, \theta)$ , and  $(W, x, y, G, r, \theta, S)$  were moderate, ranging from 0.9164 to 0.9872. The average accuracy rates of phantom images with Var30 and Var30RF20 segmented by a decision tree for spatial information  $(S, x, y, r, \theta)$  and



$(S, x, y)$  were also near to the highest values. Segmenting images with Var30RF40 with spatial information  $(G, x, y, r, \theta)$ ,  $(G, x, y)$ ,  $(G, x, y, S, r, \theta)$ ,  $(W, x, y, G, r, \theta)$ , and  $(W, x, y, G, r, \theta, S)$  produced the lowest average accuracy rates, although segmentation with spatial information  $(S, x, y, r, \theta)$  and  $(S, x, y)$  produced a higher average accuracy rate of 0.9461. The segmentation results shown in Figure 3.3 indicate that the automatic decision tree successfully segmented phantom images with different noise variations and RF inhomogeneities.

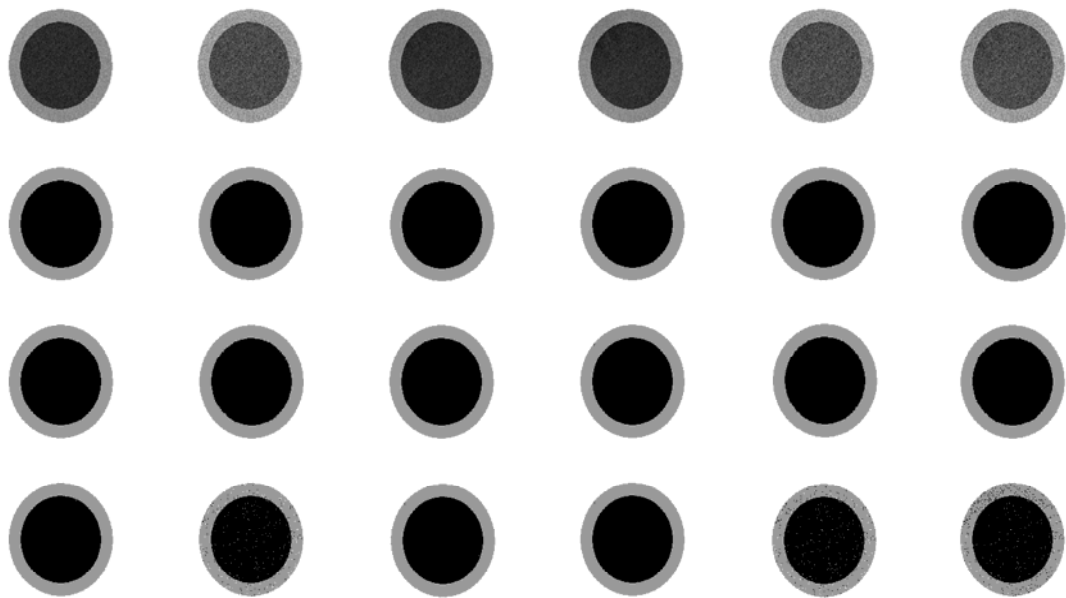


**Figure 3.3** Segmentation of phantom images from IBSR. Row 1 contains the original phantom images with Var15, Var30, Var15RF20, Var15RF40, Var30RF20, and Var30RF40. Images in rows 2, 3, and 4 represent the corresponding results of segmentation with spatial information  $(S, x, y)$ ,  $(S, x, y, r, \theta)$ , and  $(G, x, y)$ , respectively.

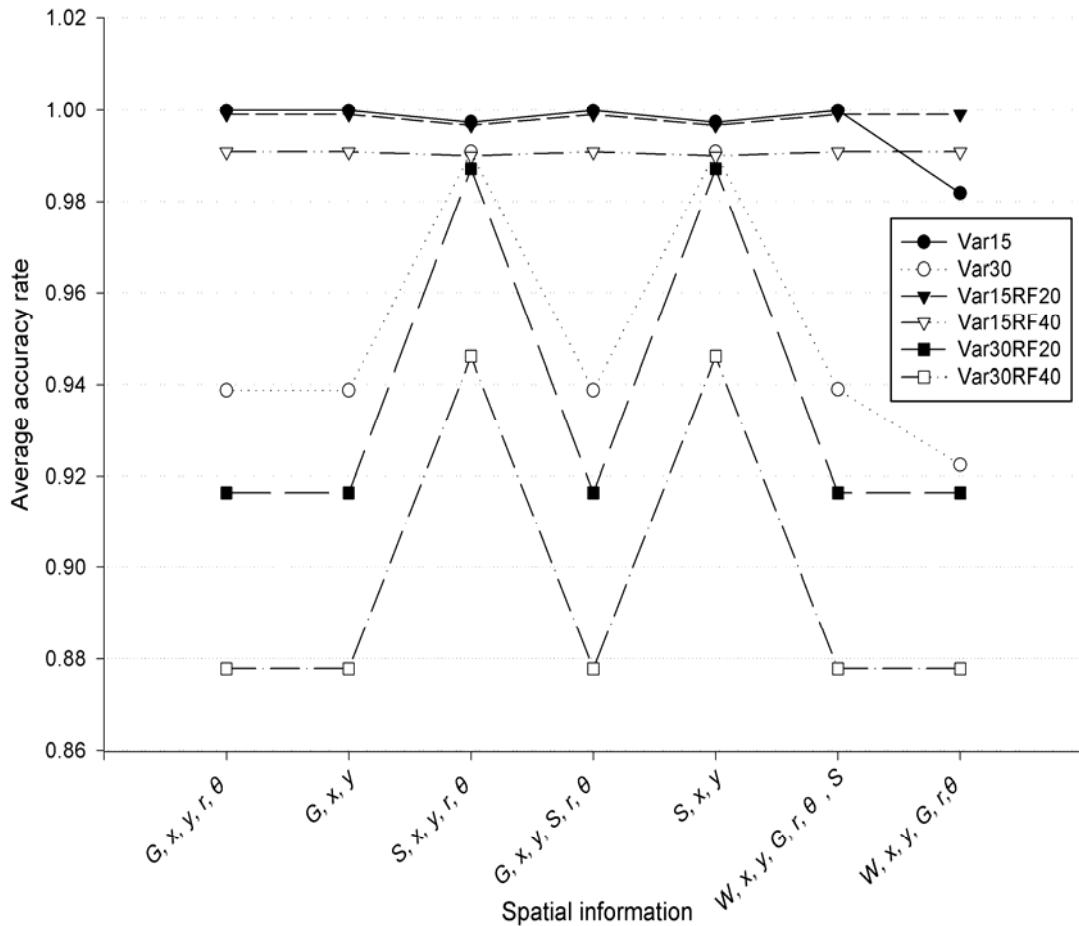
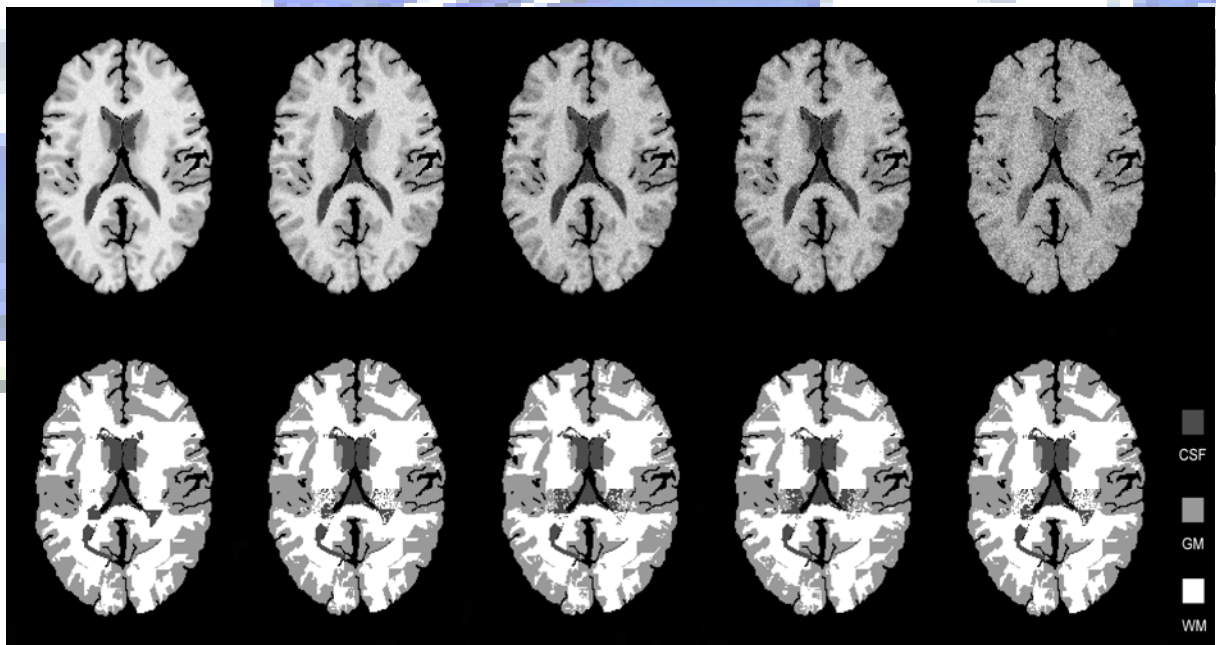


**Figure 3.4** Average accuracy rates of segmentation obtained using a decision tree with different spatial information from original phantom images with different noise variations and inhomogeneities.

### 3.3.2. Results of simulated brain MR image

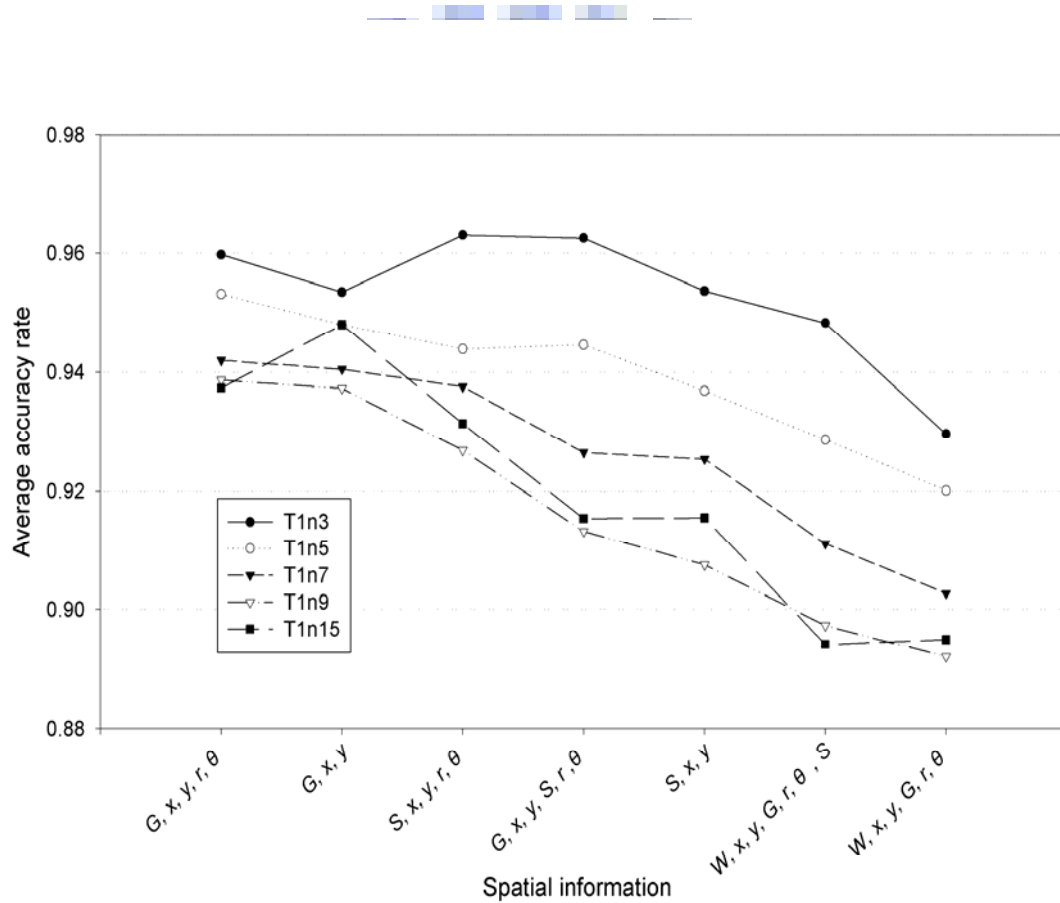
All simulated MR brain images with different noise levels and inhomogeneities (see Table 3.2) as described in Section 2 were also segmented using the automatic decision tree with different spatial information ( $G, x, y$ ), ( $S, x, y$ ), ( $G, x, y, r, \theta$ ), ( $S, x, y, r, \theta$ ), ( $G, x, y, S, r, \theta$ ), ( $W, x, y, G, r, \theta$ ), and ( $W, x, y, G, r, \theta, S$ ). Figure 3.5 shows the original simulated MR images obtained from BrainWeb (upper row) and the images resulting from segmentation with spatial information ( $G, x, y, r, \theta$ ) (lower row). The OF index was used to assess the performance of segmentation using the automatic decision tree with different spatial

information. Figure 3.6 shows the average accuracy rates of segmentation with different spatial information for simulated MR images with noise levels of T1n3, T1n5, T1n7, T1n9, and T1n15. All of the average accuracy rates were calculated for the GM, WM, CSF, and background of simulated brain MR images. The average accuracy rates decreased as the noise levels increased from T1n3 to T1n15 for most of the segmentations with this spatial information. Figure 3.6 shows that segmenting these MR images with spatial information  $(G, x, y, r, \theta)$  produced the highest average accuracy rates (0.9374–0.9598), with the resulting images shown in Figure 3.5. Segmenting these MR images with spatial information  $(G, x, y, S, r, \theta)$  and  $(W, x, y, G, r, \theta)$  produced moderate and low average accuracy rates of 0.9132–0.9626 and 0.8920–0.9297, respectively. Figure 3.5 shows that all of the simulated brain MR images with these noise levels were successfully segmented with the automatic decision tree with spatial information  $(G, x, y, r, \theta)$ ,  $(G, x, y)$ ,  $(S, x, y, r, \theta)$ ,  $(G, x, y, S, r, \theta)$ ,  $(S, x, y)$ ,  $(W, x, y, G, r, \theta, S)$ , and  $(W, x, y, G, r, \theta)$ .



**Figure 3.5** Results of segmentation using a decision tree for simulated MR images obtained from BrainWeb. Upper row contains the original MR images with noise levels of T1n3, T1n5,

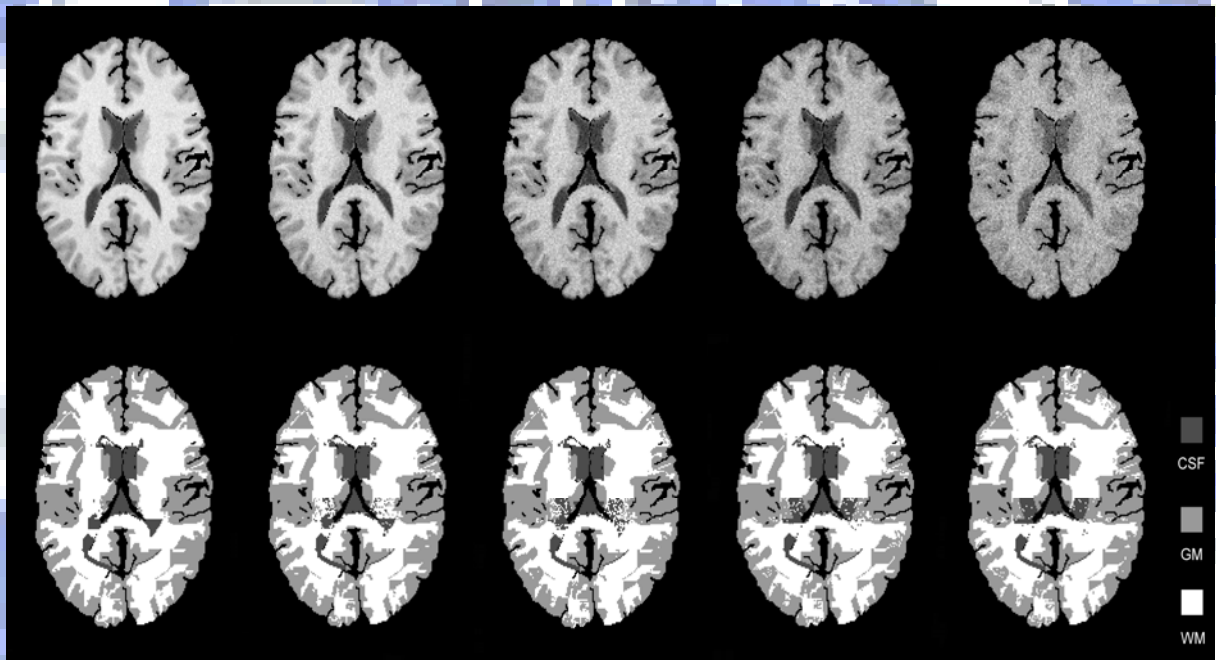
T1n7, T1n9, and T1n15. Lower row contains the corresponding images resulting from segmentation with spatial information ( $G, x, y, r, \theta$ ).



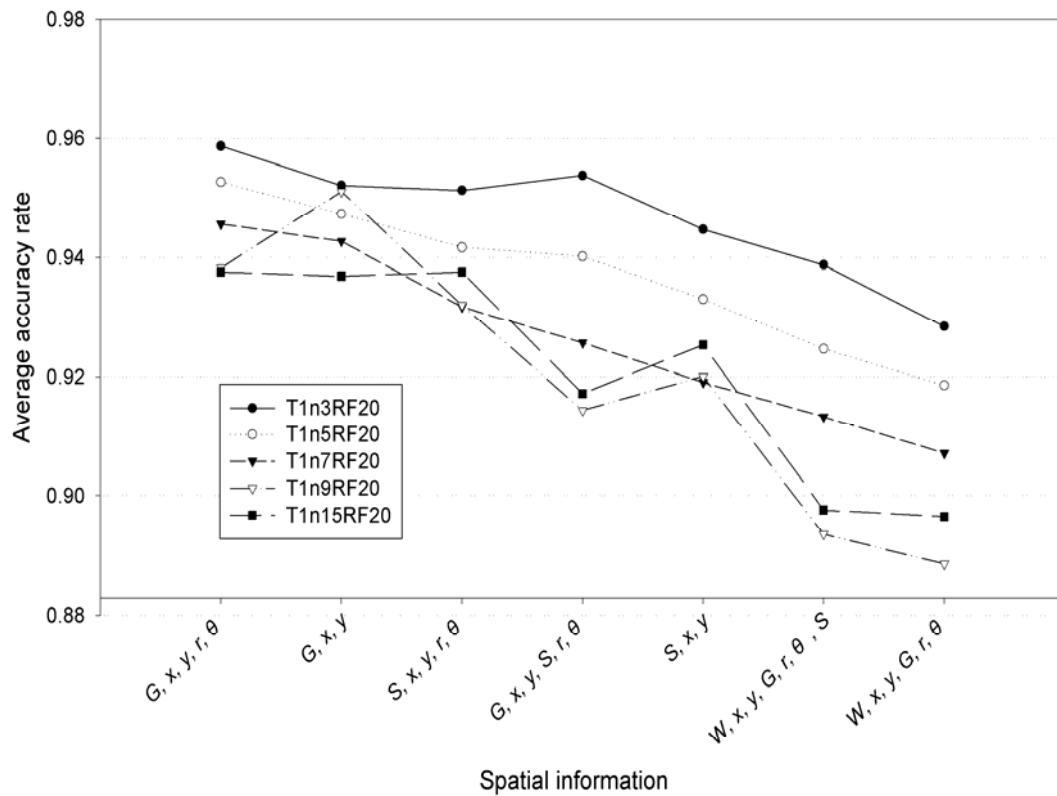
**Figure 3.6** Average accuracy rates of segmentation with different spatial information from the original MR images with noise levels of T1n3, T1n5, T1n7, T1n9, and T1n15.

Figure 3.7 shows original simulated brain MR images with different noise levels and an RF inhomogeneity of 20% obtained from BrainWeb (upper row) and the images resulting from segmentation with spatial information ( $G, x, y, r, \theta$ ) (lower row). The segmented images show better visual rendition. Figure 3.8 shows the average accuracy rates of segmentation with different spatial information from the simulated brain MR images shown in Figure 3.7. The average accuracy rates decreased as the noise level increased from T1n3RF20 to

T1n15RF20 for most of the segmentations with this spatial information. The average accuracy rates do not differ greatly between Figure 3.6 and 3.8, ranging from 0.96 to 0.89. The presence of 20% RF inhomogeneities had little effect on segmentation of these simulated brain MR images. The average accuracy rates of segmentation of these brain MR images (Figure 3.8) with spatial information  $(G, x, y, r, \theta)$ ,  $(G, x, y, S, r, \theta)$ , and  $(W, x, y, G, r, \theta)$  were 0.9376–0.9587, 0.9144–0.9538, and 0.8865–0.9285, respectively. All of the simulated brain MR images with these noise levels and inhomogeneities were successfully segmented with this spatial information for all of the accuracy rates of automatic decision-tree segmentation.



**Figure 3.7** Results of segmentation using a decision tree for simulated MR images. Upper row contains the original MR images with noise parameters of T1n3RF20, T1n5RF20, T1n7RF20, T1n9RF20, and T1n15RF20. Lower row contains the corresponding images resulting from segmentation with spatial information  $(G, x, y, r, \theta)$ .



**Figure 3.8** Average accuracy rates of segmentation with different spatial information from MR images with noise parameters of T1n3RF20, T1n5RF20, T1n7RF20, T1n9RF20, and T1n15RF20.

Figure 3.9 shows original simulated brain MR images with different noise levels and an RF inhomogeneity of 40% from BrainWeb (upper row) and the images resulting from segmentation with spatial information ( $G, x, y, r, \theta$ ) (lower row). The segmented images show better visual rendition. Figure 3.10 shows the average accuracy rates of segmentation with different spatial information from the simulated brain MR images shown in Figure 3.9. The average accuracy rates decreased as the noise level increased from T1n3RF40 to T1n15RF40 for most of the segmentations with this spatial information. The average accuracy rates do not differ greatly between Figure 3.8 and 3.10 except in lower values of the range. The 40% RF

inhomogeneities have a greater effect on the segmentation than that shown for the 20% RF inhomogeneities in Figure 3.7 and 3.8. The average accuracy rates of segmentation of these MR images with spatial information  $(W, x, y, G, r, \theta)$  as shown in Figure 3.10 changed from 0.8810 to 0.9261, and were also lower than that in brain MR images with T1n3RF20 to T1n15RF20 because of the larger fraction of the combined inhomogeneities. A higher average accuracy rate of segmentation with spatial information  $(G, x, y, r, \theta)$  for simulated brain MR images made it easier to classify the GM, WM, and CSF in simulated MR brain images with different noise levels and inhomogeneities, as shown in Figure 3.11. Figure 3.11(a) shows the accuracy rates of segmentation with spatial information  $(G, x, y, r, \theta)$  for simulated brain MR images with T1n3, T1n5, T1n7, T1n9, and T1n15; Figure 3.11(b) shows the rates for T1n3RF20, T1n5RF20, T1n7RF20, T1n9RF20, and T1n15RF20; and Figure 3.11(c) shows the rates for T1n3RF40, T1n5RF40, T1n7RF40, T1n9RF40, and T1n15RF40. Figure 3.11 shows that the accuracy rates of segmentation with spatial information  $(G, x, y, r, \theta)$  decreased with increasing noise level, but were not affected by RF inhomogeneities. The accuracy rates were higher, moderate, and lower for segmentation with spatial information  $(G, x, y, r, \theta)$  of GM, WM, and CSF in brain MR images, respectively. The higher and lower accuracy rates for CSF in Figure 3.10 and 3.11 were attributable to it representing larger and smaller regions, respectively, in brain MR images for training and testing. Together our results indicated that GM, WM, and CSF in simulated brain MR images with the investigated noise levels and inhomogeneities were all successfully segmented using this proposed automatic decision-tree algorithm, irrespective of the accuracy rates, with the described spatial information.

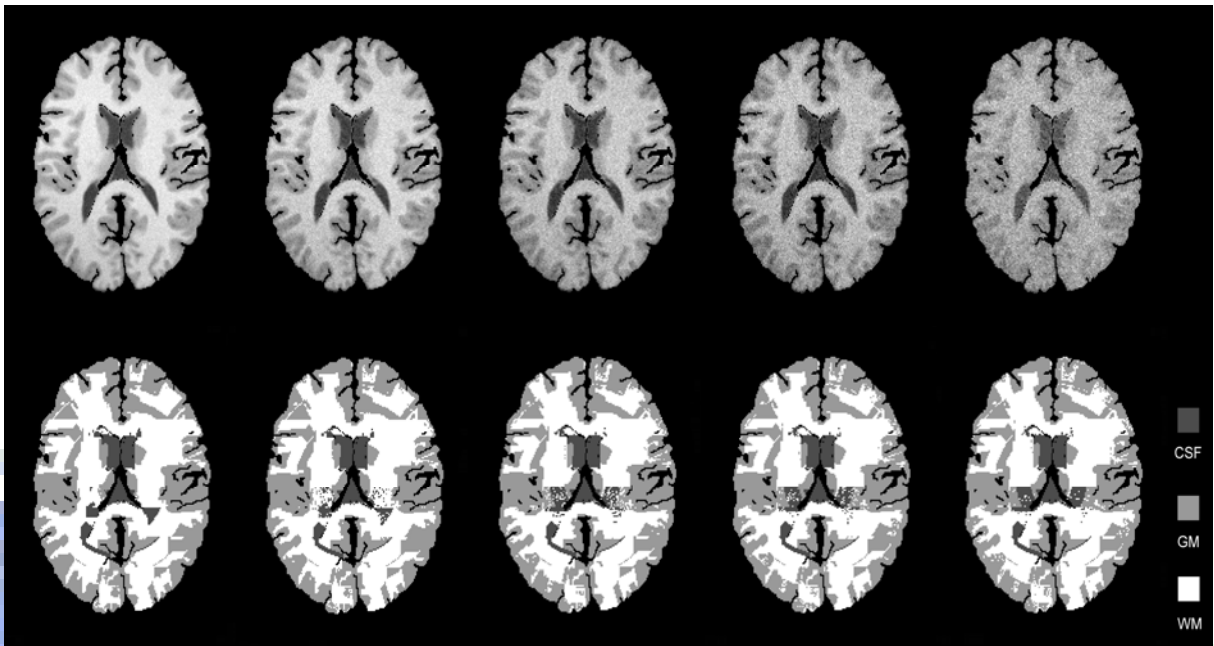


**Figure 3.9** Results of segmentation using a decision tree for simulated MR images. Upper row contains the original MR images with noise parameters of T1n3RF40, T1n5RF40, T1n7RF40, T1n9RF40, and T1n15RF40. Lower row contains the corresponding images resulting from segmentation with spatial information  $(G, x, y, r, \theta)$ .



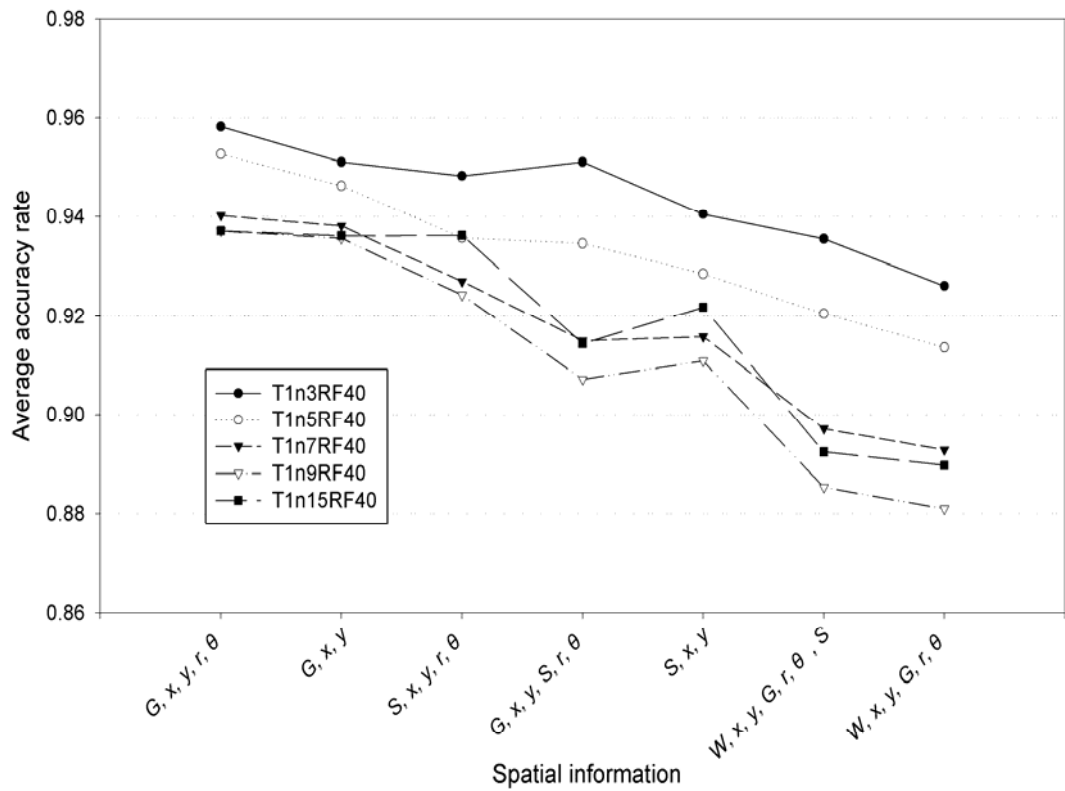


**Figure 3.10** Average accuracy rates of segmentation with different spatial information from MR images with noise parameters of T1n3RF40, T1n5RF40, T1n7RF40, T1n9RF40, and T1n15RF40.

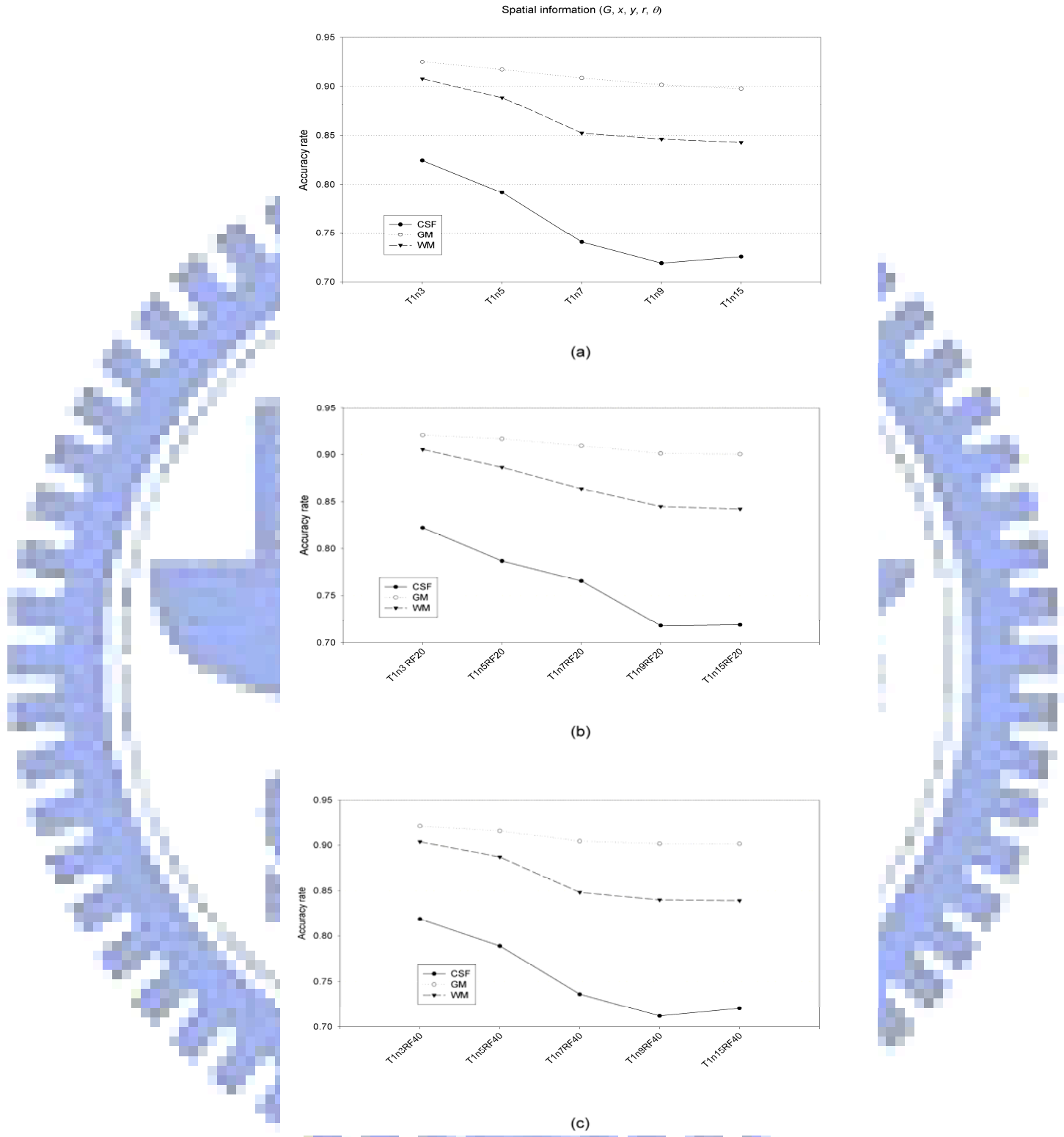


**Figure 3.11** Accuracy rates of GM, WM, and CSF in simulated MR images segmented using a decision tree with spatial information ( $G, x, y, r, \theta$ ) for T1n3, T1n5, T1n7, T1n9, and T1n15 (a); T1n3RF20, T1n5RF20, T1n7RF20, T1n9RF20, and T1n15RF20 (b); and T1n3RF40, T1n5RF40, T1n7RF40, T1n9RF40, and T1n15RF40.

### 3.4. Discussions

A proposed automatic segmentation method using a decision tree was used in the present study to classify different tissue types in brain MR images. The phantom and simulated MR images obtained from IBSR and BrainWeb, respectively, were both successfully segmented by the proposed decision-tree algorithm. The performance of the proposed segmentation technique was evaluated using a previously described index [44, 93]. The gray-level distributions in the phantom MR images differed more between the various regions. The spatial gray-level information had a greater effect on the performance of phantom image segmentation. The gray-level distributions of each tissue overlapped more in different regions in simulated brain MR images than in the phantom MR images. Therefore, the spatial gray-level information is useful for assessing the performance of segmentation, with local features of the spatial information being more suitable for assessing the accuracy of segmentation by a decision tree of a simulated MR image. The average accuracy rates were higher with spatial information  $(S, x, y, r, \theta)$  and  $(S, x, y)$  for the simulated phantom MR images with all the used noise levels and inhomogeneities, which was due to the gray levels of the spatial information being the main factor affecting segmentation of the phantom images. The average accuracy rates were lower for all the used spatial information when the simulated phantom MR images were combined with a noise variation of 30 gray levels. Furthermore, the average accuracy rates were highest with spatial information  $(G, x, y, r, \theta)$  for simulated brain MR images with all the used noise levels and inhomogeneities due to the location attribute of the spatial information being more important than the gray-level information. The average accuracy rates were lowest for all the used spatial information when the simulated brain MR images contained 15% noise, which represented the largest fraction of images. The best results of segmentation were obtained in this study for simulated and brain MR images with the lowest noise levels.

The noise level is the main factor responsible for overlapping of the gray-level

distribution in MR images. Also, the gray level is the main spatial feature that affects the performance of segmentation in phantom MR images, and hence it is the main decision attribute of tree structures. These characteristics were confirmed in both phantom and simulated MR images. The average accuracy rates of segmentation with spatial information ( $G, x, y, r, \theta$ ) were highest for phantom images with Var15, Var15RF20, and Var15RF40 (0.9999, 0.9990, and 0.9908, respectively), and were lowest for phantom images with Var30, Var30RF20, and Var30RF40 (0.9388, 0.9164, and 0.8778). The decrease (0.06) in the average accuracy rate for phantom images with Var15 and Var30 was more than that (0.0009) for phantom images with Var15 and Var15RF20 (see Figure 3.4). The noise variation was the main factor affecting the accuracy rate of phantom image segmentation. In simulated MR images, the average accuracy rates of segmentation with spatial information ( $G, x, y, r, \theta$ ) were highest for simulated MR images with T1n3 and T1n15 (0.9598 and 0.9374, respectively) (Figure 3.6), and lowest for simulated MR images with T1n3RF40 and T1n15RF40 (0.9582 and 0.9371, respectively). The decrease (0.0224) in the average accuracy rate for simulated images with T1n3 and T1n15 was more than that (0.0016) for phantom images with T1n3 and T1n3RF40 (see Figure 3.10). The noise level was also the main factor affecting the accuracy rate of simulated MR image segmentation. Noise had similar effects on the trends in the performance of tissue (GM, WM, and CSF) segmentation of simulated MR images (see Figure 3.11), and those on GM and WM segmentation were similar to those of previously reported approaches [42, 43, 53]. The accuracy rates of our segmentation method increased with decreasing noise level, which is consistent with previous results for tissues or the overall cortical surface [42, 43, 53, 94]. Our method was also suitable for segmenting MR images, although its performance decreased as the noise level in the images increased.

For comparison, consider the spatial information approach proposed by Anbeek *et al.* [44]. In phantom images (see Figure 3.4), the average accuracy rates of segmentation for phantom images with Var15 were 0.9999 and 0.9973 with spatial information ( $G, x, y, r, \theta$ )

and  $(S, x, y, r, \theta)$ , respectively, 0.9999 and 0.9973 with spatial information  $(G, x, y)$  and  $(S, x, y)$ , and 0.9999 and 0.9819 with spatial information  $(G, x, y, S, r, \theta)$  and  $(W, x, y, G, r, \theta)$ . In simulated MR images (see Figure 3.6), the average accuracy rates of segmentation for simulated MR images with T1n5 were 0.9532 and 0.9439 with spatial information  $(G, x, y, r, \theta)$  and  $(S, x, y, r, \theta)$ , respectively, 0.9480 and 0.9369 with spatial information  $(G, x, y)$  and  $(S, x, y)$ , and 0.9446 and 0.9287 with spatial information  $(G, x, y, S, r, \theta)$  and  $(W, x, y, G, r, \theta)$ . The overlapping of gray levels of noise was greater for spatial information  $(S)$  obtained from five neighboring pixels (see Figure 3.1(a)) in a local region than for spatial information  $(G)$  obtained from a single gray-level intensity. Therefore, the accuracy rates of segmentation with spatial information  $(S, x, y)$  and  $(S, x, y, r, \theta)$  were lower than those of segmentation with spatial information  $(G, x, y)$  and  $(G, x, y, r, \theta)$ . The overlapping of gray levels of noise was greater for spatial information  $(W)$  obtained from nine neighboring pixels (see Figure 3.1(b)) in a local region than for spatial information  $(G)$  obtained from a single gray-level intensity. Thus, the accuracy rates of segmentation with spatial information  $(W, x, y, G, r, \theta)$  were lower than those of segmentation with spatial information  $(G, x, y, S, r, \theta)$ .

A comparison of inhomogeneity revealed that the average accuracy rates of segmentation with spatial information  $(G, x, y, r, \theta)$  from phantom MR images with Var15, Var15RF20, and Var15RF40 were 0.9999, 0.9990, and 0.9908, respectively (see Figure 3.4), indicating the absence of large differences in the accuracy rates of segmentation of phantom MR images with inhomogeneity. The average accuracy rates of segmentation with spatial information  $(G, x, y, r, \theta)$  for simulated MR images with T1n5, T1n5RF20, and T1n5RF40 were 0.9532, 0.9527, and 0.9527, respectively (see Figure 3.6, 3.8, and 3.10). The accuracy rates of segmentation with spatial information  $(G, x, y, r, \theta)$  of CSF of simulated MR images with T1n3, T1n3RF20, and T1n3RF40 were 0.8241, 0.8222, and 0.8185, respectively (see Figure 3.11). The accuracy rates of segmentation with spatial information  $(G, x, y, r, \theta)$  of GM of simulated MR images with T1n3, T1n3RF20, and T1n3RF40 were 0.9251, 0.9211, and

0.9214, respectively (see Figure 3.11). The accuracy rates of segmentation with spatial information ( $G, x, y, r, \theta$ ) of WM of simulated MR images with T1n3, T1n3RF20, and T1n3RF40 were 0.9077, 0.9054, and 0.9038, respectively (see Figure 3.11). These data indicated the large differences were also absent in the accuracy rates of segmentation of tissues in MR images with inhomogeneity. Thus, the presence of inhomogeneity in MR images might not decrease the accuracy rates of segmentation for both phantom MR images and simulated MR images.

The performance of segmentation in the present study might have been affected by the gold standard being segmented by an expert as a standard reference. Other approaches could also be used to determine the gold-standard reference image. A more sophisticated method [95] is for a group of experts to construct the reference gold-standard image, which might improve the accuracy of segmentation.

In conclusion, our segmentation method based on a decision-tree algorithm represents a useful way to perform automatic segmentation for both phantom and tissue (GM, WM, and CSF) regions in brain MR images. The accuracy rates of segmentation were highest for both simulated phantom and brain MR images with the lowest noise levels, due to this reducing the amount of overlap in gray levels in the images. The accuracies of segmentation were higher when the spatial information included the general gray level ( $G$ ) than when it included the spatial gray level ( $S$ ), which in turn were higher than when it included the wavelet transform ( $W$ ). Finally, the accuracy rate of our segmentation method was not affected by inhomogeneity in MR images.

## Chapter 4 Segmentation of Brain MR images Using a Boosted Decision Tree (BDT)

### 4.1. Introduction

The studies of literature review demonstrated that the increasing accuracy of segmentation is more important in classifying different brain tissues for improving anatomical structures in real applications. In this Chapter, we will propose another automatic segmentation method of decision tree to improve the segmentation accuracy of the GM, WM, and CSF in brain MR images and to obtain clear anatomical structures. The segmentation method is a boosted decision tree combined with fuzzy threshold.

Decision trees can be constructed from many specific algorithms. A classification and regression tree (CART) can be applied for classification analysis while also acting as a regression tree. CART is a binary tree that has been utilized in many studies [89, 90, 96]. The C4.5 learning method proposed by Quinlan *et al.* in 1993 is another decision tree that was reformed from the ID3 learning system proposed by Quinlan in 1986 [97] and used in a supervised classification problem. The C4.5 was advanced to the See5/C5.0 to improve decision tree performance [98–100]. The ID3, C4.5, and C5.0 have been used for classification in many studies. The C4.5 learning system was used to determine the optimal subset of a control system for selecting attributes among continuous attributes, noise data, and alternative measures [101]. The C5.0 was used to classify electrocardiograms (ECG) in a healthy control subject and in a subject with a heart disorder, wherein three experiments were conducted including classifications based on 2, 3, and 7 classes. This system was successfully used to classify bundle branch block, cardiomyopathy, arrhythmia, healthy control, hypertrophy, myocarditis, and myocardial infraction with good accuracy [102]. We used a decision tree in our study because it has several advantages in biomedical applications. Specifically, it can be

effectively used to classify any data structure, it can perform with good prediction accuracy for non-linear problems, it is easy to interpret rules in a rule set of the decision tree, and it effectively eliminates outliers [96]. Therefore, we propose a boosted decision tree algorithm combined with fuzzy threshold for the classification of brain tissues, such as GM, WM, and CSF, with the goal of improving accuracy rates of brain MR image segmentation.

## **4.2. Materials and methods**

### **4.2.1. MR data**

Two types of simulated data were used in this study, including simulated phantom MR (SPMR) images and simulated brain MR (SBMR) images. The SPMR images were the same as described in Table 3.1. The SBMR images obtained from BrainWeb were T1-weighted 3-mm-thick images with noise levels of 3%, 5%, 7%, and 9% and the same as described in Table 3.2. Furthermore, RF inhomogeneities of either 20% or 40% were also added to the images with each noise level as described in Table 3.2. An expert manually labeled an exemplar brain MR image from the original image with no noise and inhomogeneities; this was used as our standard image. All of the simulated data were preprocessed to obtain spatial features and then segmented using the decision tree algorithm.

Real data of brain MR images were also used for this experiment. Healthy participants were scanned with a 1.5T MRI system (Signa NV/i, GE Medical Systems, Waukesha, WI) using a standard head coil and an adjustable padded head holder to minimize head motion. The 3D T<sub>1</sub>-weighted time-of-flight fast spoiled gradient recalled acquisition in steady state (FSPGR, TR/TE = 13.4/2.7 msec, NEX=1, FOV = 260 mm; 512 × 256 matrix, slice thickness = 2 mm) pulse sequence was used. 144 axial slices were acquired encompassing the whole brain.



#### 4.2.2. Image preprocessing

Spatial features were extracted from every MR image pixel location and used as the input for the segmentation algorithm for image preprocessing which were the same as in Chapter 3. The spatial features used in the present study were:  $G$ ,  $S$ ,  $W$ ,  $x$ ,  $y$ ,  $r$ , and  $\theta$ , where  $G$  represents the gray level intensity of every pixel,  $S$  the spatial gray level of every pixel,  $W$  the coefficients of the wavelet transform,  $(x, y)$  Euclidean coordinates, and  $(r, \theta)$  polar coordinates. The spatial features were preprocessed from the same procedure described in Section 3.2.1.

#### 4.2.3. Segmentation

A decision tree combined with boost trials and a fuzzy threshold was used in this study. This method was shown by Quinlan to model the prediction tree using a statistical analysis that considered outcome variables to make an accurate prediction [100]. The image segmentation processing procedures are summarized in Figure 4.1. A standard image was trained using the boosted decision tree with a fuzzy threshold, while images with noise levels and RF inhomogeneities were then tested by the decision tree constructed from the trained structures. The operation is described as follows.

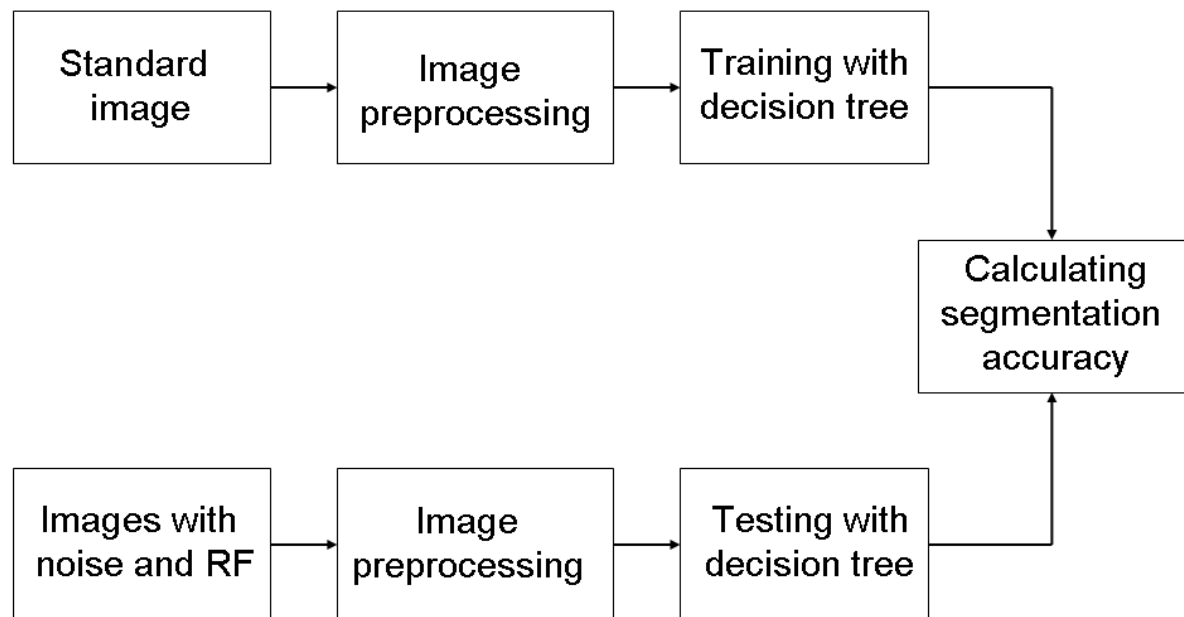


**Figure 4.1** A flow diagram of image processing procedures for MR image segmentation.

#### 4.2.4. Decision tree classification

The decision tree builds a classifier form that can be integrated using boosting and a fuzzy threshold [98, 100, 103]. Regions and tissues in the SPMR images were divided into three and four classes of the decision tree, respectively. A schematic diagram of the decision tree structure is shown in Figure 4.2. A decision tree is a tree structure that grows from a root node, flows outward toward internal nodes, and terminates at leaf nodes. The leaf nodes represent the class, wherein the classifier is a model derived from the training dataset and is applied to predict class values in a test dataset. In the tree structure, each internal node is divided by a condition related to a feature, and each branch denotes the outcome of attribute splitting. Each node (root node and internal node) is split into two or more branch nodes. Examples of splitting conditions include “ $A > a$ ,” “ $B > b$ ,” or “ $C > c$ ” for each node in every

attribute, as shown in Figure 4.2. Branch splitting is determined by the condition of each node. The leaf nodes depict classification by these splitting conditions, and the class is labeled on the leaf node. The decision tree structure can be transferred into a set of rules.

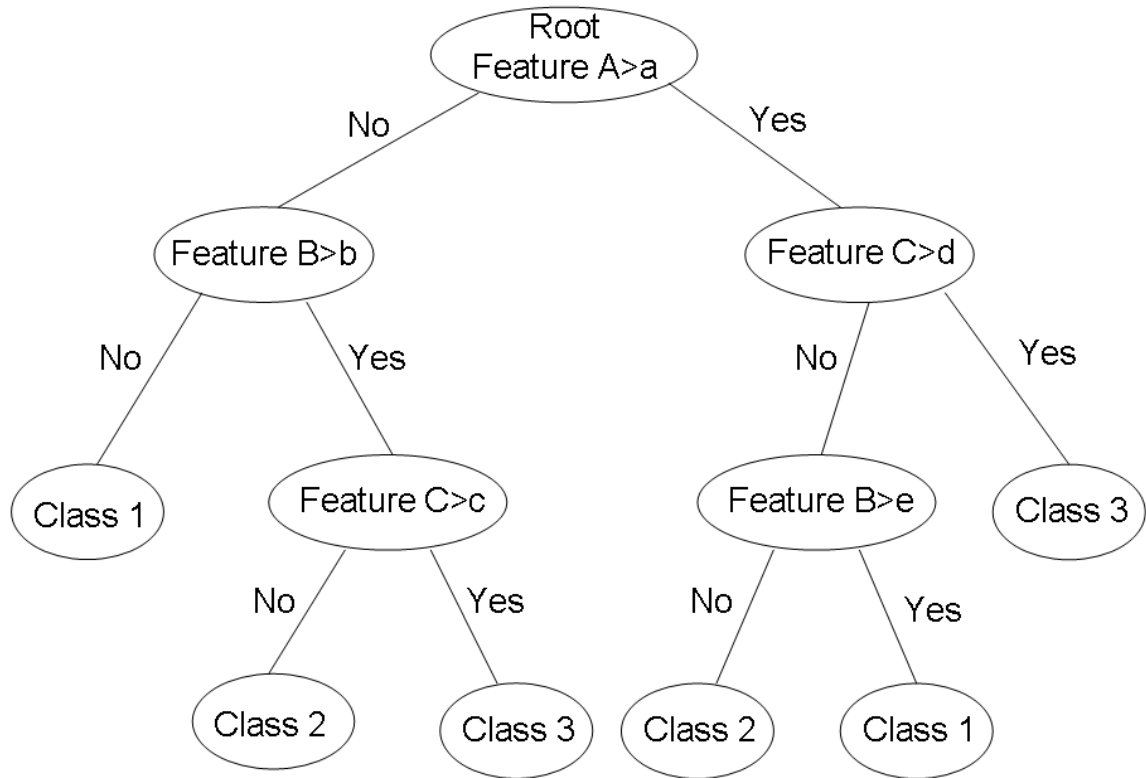


**Figure 4.2** Schematic diagram of the decision tree structure.

#### 4.2.5. Decision tree construction with gain ratio

The proposed decision tree is constructed from a data set  $S$  by the training criteria, *Gain Ratio*, which is a measure of incorporated entropy [98, 103–106]. The procedures of *Gain Ratio* are defined as follows. For simulated MR data, assume that a training data set  $S$  consists of  $C$  class examples. The function  $p(S, r)$  is the ratio for the class number of an MR data set belonging to class  $r$  of the total class number  $|S|$  of an MR data set  $S$ , where  $1 \leq r \leq C$ . The entropy is defined as

$$Entropy(S) = -\sum_{r=1}^C p(S, r) \times \log_2 p(S, r). \quad (4.1)$$

Suppose that  $T$  is a feature whose total partitions are  $v$ . The value  $i$  is any specific value of  $v$ , while  $S_i$  is a subset of the MR data set  $S$  corresponding to the value  $i$  of  $T$ . The information gain,  $Gain(S, T)$ , corresponding to the partitioning of  $S$  from feature  $T$ , is calculated by:

$$Gain(S, T) = Entropy(S) - \sum_{i=1}^v \frac{|S_i|}{|S|} \times Entropy(S_i), \quad (4.2)$$

where  $|S_i|$  is the number of subsets  $S_i$  in the MR data, and  $Entropy(S_i)$  is calculated similarly as  $Entropy(S)$ . In order to obtain a good generation by reducing bias, the gain ratio  $GainRatio(S, T)$  was calculated, wherein the  $SplitInfo$  (Equation 8) is first provided as:

$$SplitInfo(S, T) = -\sum_{i=1}^v \frac{|S_i|}{|S|} \times \log_2 \left( \frac{|S_i|}{|S|} \right). \quad (4.3)$$

The function  $Gain(S, T)$  is very sensitive to the value of  $v$ , so the ratio of information gain is calculated as:

$$GainRatio(S, T) = \frac{Gain(S, T)}{SplitInfo(S, T)}. \quad (4.4)$$

The feature  $T$  satisfies:

$$\Gamma = \arg \max_T (GainRatio(S, T)) \quad (4.5)$$

and is selected as the reference for this step of partitioning. The decision tree is constructed by splitting all of the features and maximizing the gain ratio ( $\Gamma$ ).

#### 4.2.6. Boosting

The addition of boosting to a decision tree as a means to improve prediction accuracy is known as adaptive boosting, and was proposed by Freund and Schapire [98, 100, 107–109]. Adaptive boosting is based on a learning algorithm of a decision tree classifier over a repeated

series of trials:  $t = 1, \dots, T$ . One possible approach is to select a best weight and tree structure from the distribution of weights over the training set. For a training set  $(x_1, y_1) \dots (x_m, y_m)$ ,  $x_i$  belongs to  $X$  and  $y_i$  belongs to label set  $Y$ . This generates the weak hypothesis  $h_t(i) : X \rightarrow \{-1, +1\}$ , as  $D_t(i)$  is the weight distribution on training instance  $i$  at trial  $t$ . The error of the hypothesis is given as

$$\varepsilon_t = \Pr_{i \sim D_t} [h_t(x_i) \neq y_i] = \sum_{i: h_t(x_i) \neq y_i} D_t(i), \quad (4.6)$$

where the  $\Pr_{i \sim D_t}[\cdot]$  is the probability with respect to the distribution  $D_t(i)$  when the weak learner was trained. The parameter of weight will be chosen as

$$\alpha_t = \frac{1}{2} \ln \left( \frac{1 - \varepsilon_t}{\varepsilon_t} \right), \quad (4.7)$$

where  $\alpha_t$  increases when  $\varepsilon_t$  decreases. After updating  $D_t(i)$ , the final hypothesis  $H$  measures the confidence in the boosting prediction, and is given as

$$H(x) = \text{sign} \left( \sum_{t=1}^T \alpha_t h_t(x) \right). \quad (4.8)$$

The final hypothesis  $H$  is a majority vote in  $t = 1 \dots T$ , where  $\alpha_t$  is the weight of  $h_t$ .

Many classifiers are constructed from a single training dataset for boosting. Each classifier is constructed to form a single decision tree structure or a rule set using the training data. New classifications are based on votes from many classifiers, while the predicted and final classes are decided from the votes. The first step of this boosting procedure is to build a single decision tree structure or a rule set from the training data. This classifier will usually contribute to the errors for some cases in the data. The first decision tree structure generates the wrong class for some cases in the training data. Next, the second classifier is constructed with greater attention to correct classification. The second classifier will consequently be different from the first classifier. The third classifier construction step is comparatively even more focused, although it also will make mistakes in some cases. By setting the boost trial number in advance, the boosting process continues iteratively by updating  $D_t(i)$ . The final

step of the boosting process is stopped when the most recent classifier is either extremely accurate or inaccurate.

#### 4.2.7. Fuzzy threshold

In a fuzzy threshold process [98, 100], the threshold for each feature partition is divided into three ranges, including a lower bound,  $lb$ ; an upper bound,  $ub$ ; and a central value,  $t$ . If the feature value (or attribute value of the tree) in a node is below  $lb$  or above  $ub$ , the classification is partitioned using single branches corresponding to the conditions “ $\leq$ ” or “ $>$ ”, respectively. If the feature value is between  $lb$  and  $ub$ , both branches probabilistically decide the partition results. The lower and upper bounds are calculated by approaching the apparent classification sensitivity. The fuzzy threshold can resist the effects of noise and improve the accuracy rate of classification on training and testing.

#### 4.2.8. Pruning

Decision tree construction consists of two phases [97, 98, 110]. The growth phase is generated first, followed by processing in the pruning phase. The pruning phase is used to optimize the decision tree structures. Global pruning was selected in the decision tree algorithm. Subtree replacement is performed in the pruning step when the subtree error rates for the training set are reduced. If the error rate is below the  $CF$  (25%), the nodes of the tree structure are trimmed to replace the subtree by a leaf node. The  $CF$  is the probability of a binary distribution, as defined in Equation (14), and is calculated from the training set. The class label of the leaf node is then defined as a simplified tree consisting of a class of attributes in a subtree. The function of pruning is to reduce the risk of overfitting the tree. Overfitting occurs when the tree is overspecialized to the training set. The pruning phase was developed to improve classification accuracy by removing subtrees that are predicted to have high error rates.

When replacing the leaf node of a tree, statistical analysis is used to obtain confidence by manipulating the posterior probability of misclassification. For example, assume an event happens  $M$  times in  $N$  trials. The estimated probability  $p$  of the event is the ratio  $M/N$ . The confidence limits for  $p$  can then be calculated. For the confidence  $CF$  given in Equation (4.9), the estimated probability  $p$  can be calculated as  $1 - CF$  such that  $p \leq p_r$ . The upper limit  $p_r$  [111] is satisfied as

$$CF = \begin{cases} (1 - p_r)^N, & \text{for } M = 0 \\ \sum_{i=0}^M \binom{N}{i} p_r^i (1 - p_r)^{N-i}, & \text{for } M > 0 \end{cases}, \quad (4.9)$$

where  $CF$ -pruning is set to 25% as default.

#### 4.2.9. Three-dimensional reconstruction

Each segmented image was exported separately as a distinct .mat (MATLAB) file to Amira 4.1 (Mercury Computer Systems Inc., Chelmsford, MA) for surface rendered 3D models. Surface reconstruction from the images yields triangulated surfaces with a stepped structure due to the anisotropy of the voxels. To obtain a superior representation of the true anatomical 3D-shape the labelings are interpolated by inserting intermediate slices between each two consecutive slices of the original image stack, such that the resulting voxel size is nearly isotropic. All these steps are performed with the help of the visualization and modeling software Amira [112] and Amira User's Guide, Reference Manual and Amira Programmer's Guide are available at the Website <http://www.amiravis.com/>.

#### 4.2.10. The evaluation index of segmentation

Two kinds of indexes to evaluate the segmentation performance were mainly used in this Chapter. One is the accuracy rate which is the same as the index in Section 3.2.6 of Chapter 3. The other is the  $k$  index (also called the Dice coefficient) described as below. Another

evaluation indexes referred from other approaches are also used to compare the performance of segmentation from brain MR images.

The  $k$  index as given in Equation (4.10), which is another means of segmentation evaluation, was also used to quantify the performance of segmentation. The  $k$  index is ordinarily used to measure the similarity of two images [41–43, 44, 48, 53, 113]. Given two images,  $S_1$  denotes all tissues of the standard reference image, while  $S_2$  denotes all tissues of the segmented image. The  $k$  index is defined as:

$$k(S_1, S_2) = \frac{2|S_1 \cap S_2|}{|S_1| + |S_2|}, \quad (4.10)$$

where  $|S_1 \cap S_2|$  denotes the intersection area between  $S_1$  and  $S_2$ . The  $k$  index, running from 0 to 1, was applied to compare the segmented image and standard image (manually labeled by an expert).

### 4.3. Experimental results

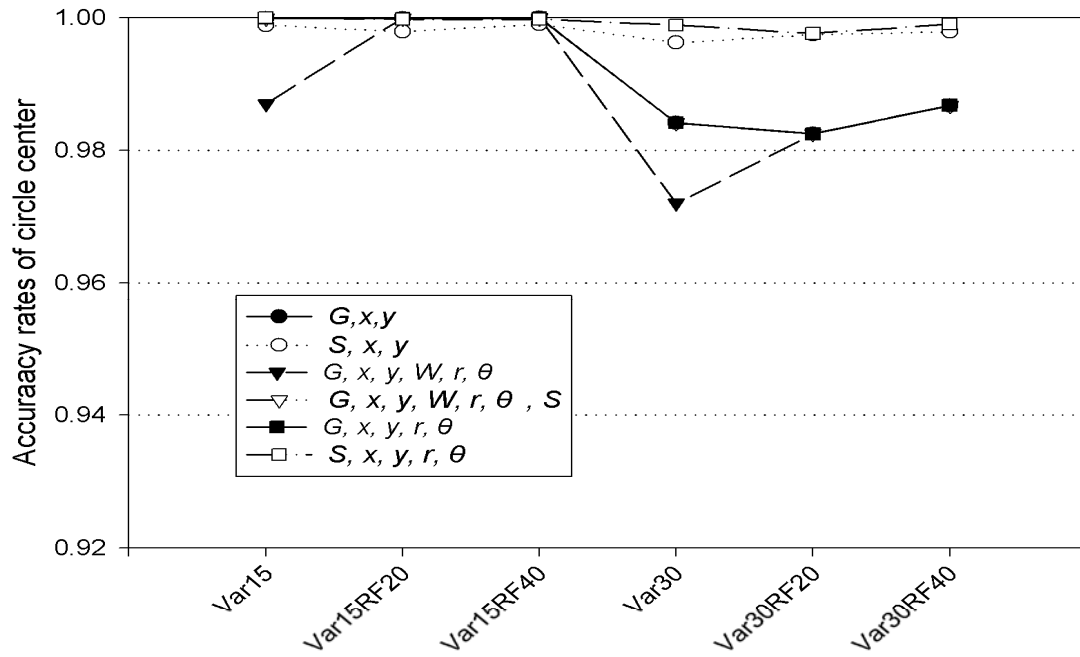
#### 4.3.1. Segmentation of SPMR images

As shown in Figure 4.3, we examined the accuracy rates of SPMR image region segmentation with several levels of noise and inhomogeneities (see Table 3.1) using various spatial features. The accuracy rates of circle center and circle ring segmentation using spatial features  $(G, x, y)$ ,  $(S, x, y)$ ,  $(W, x, y, G, r, \theta)$ ,  $(W, x, y, G, r, \theta, S)$ ,  $(G, x, y, r, \theta)$ , and  $(S, x, y, r, \theta)$  and at different levels of noise and inhomogeneity are shown in Figures 4.3(a)-(b). Using the decision tree algorithm and six spatial features, the accuracy rates for circle center segmentation were greater than 0.9720, while the accuracy rates for circle ring segmentation were greater than 0.9309. The highest accuracy rate came from phantom region segmentation. The lowest accuracy rates were obtained when SPMR images were segmented using this

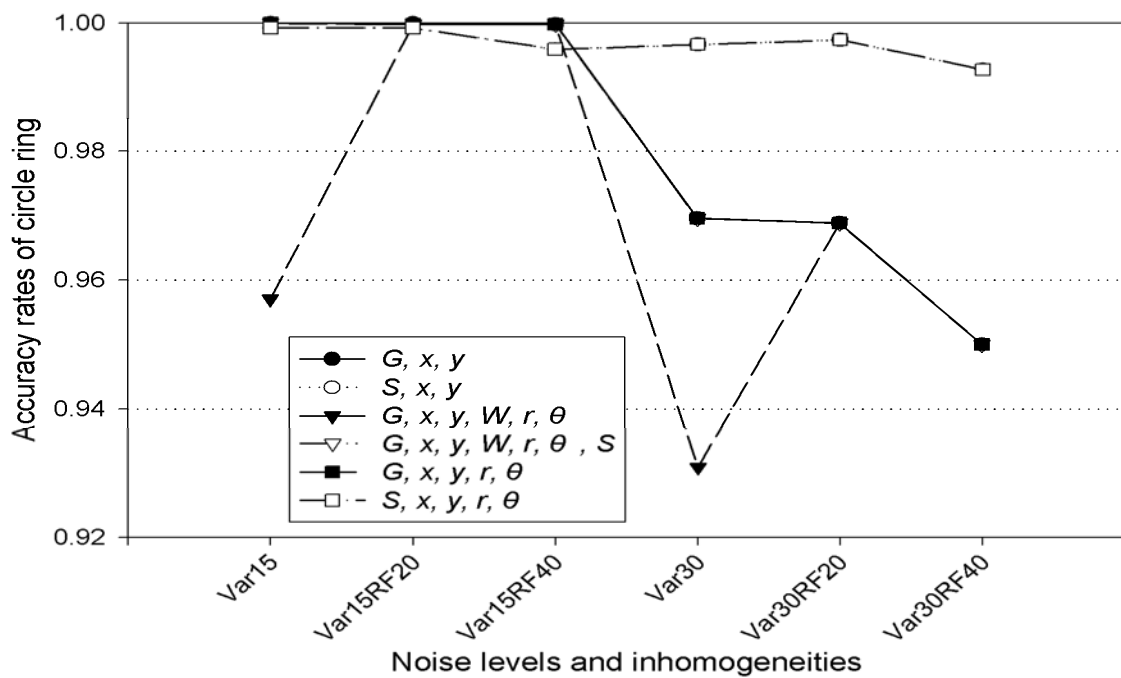


decision tree with spatial features  $(W, x, y, G, r, \theta)$  or  $(W, x, y, G, r, \theta, S)$ . Figure 4.4 shows images segmented using this decision tree algorithm with spatial features  $(G, x, y, r, \theta)$ ,  $(S, x, y, r, \theta)$ ,  $(W, x, y, G, r, \theta)$ , and  $(W, x, y, G, r, \theta, S)$  from SPMR images with noise and inhomogeneity levels of Var15, Var15RF20, Var15RF40, Var30, Var30RF20, and Var30RF40. The segmentation performance was evaluated by averaging the accuracy rates of all the phantom image regions in SPMR images with noise and inhomogeneity levels of Var15, Var15RF20, Var15RF40, Var30, Var30RF20, and Var30RF40, and segmented with spatial features  $(G, x, y, r, \theta)$ , and  $(S, x, y, r, \theta)$ .





(a)



(b)

**Figure 4.3** Accuracy rates of region segmentation obtained using different spatial features from simulated phantom MR images. (a) Accuracy rates of circle center segmentation with different spatial features. (b) Accuracy rates of circle ring segmentation with different spatial features.

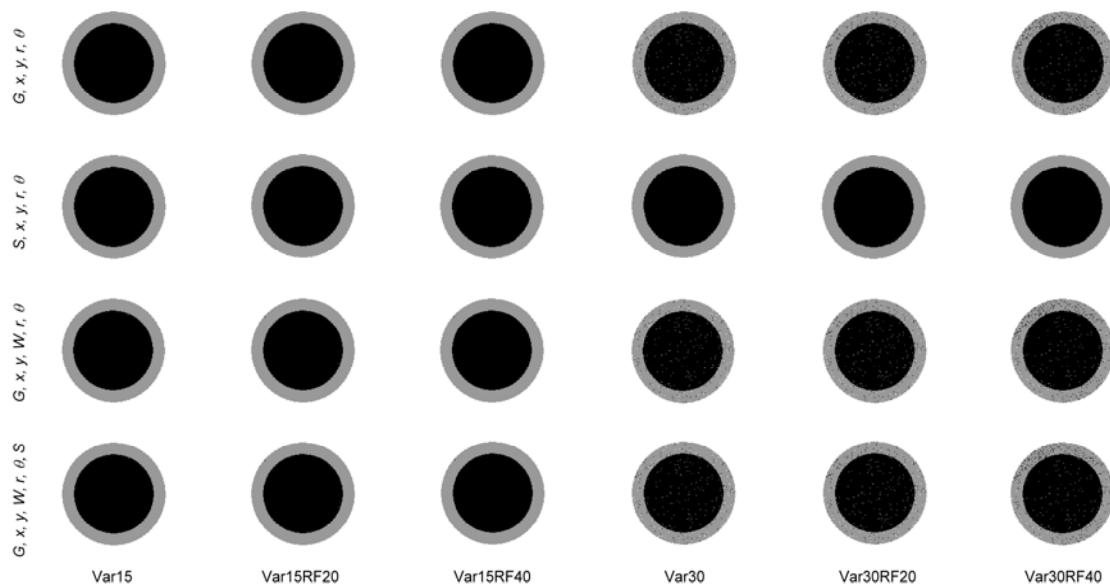
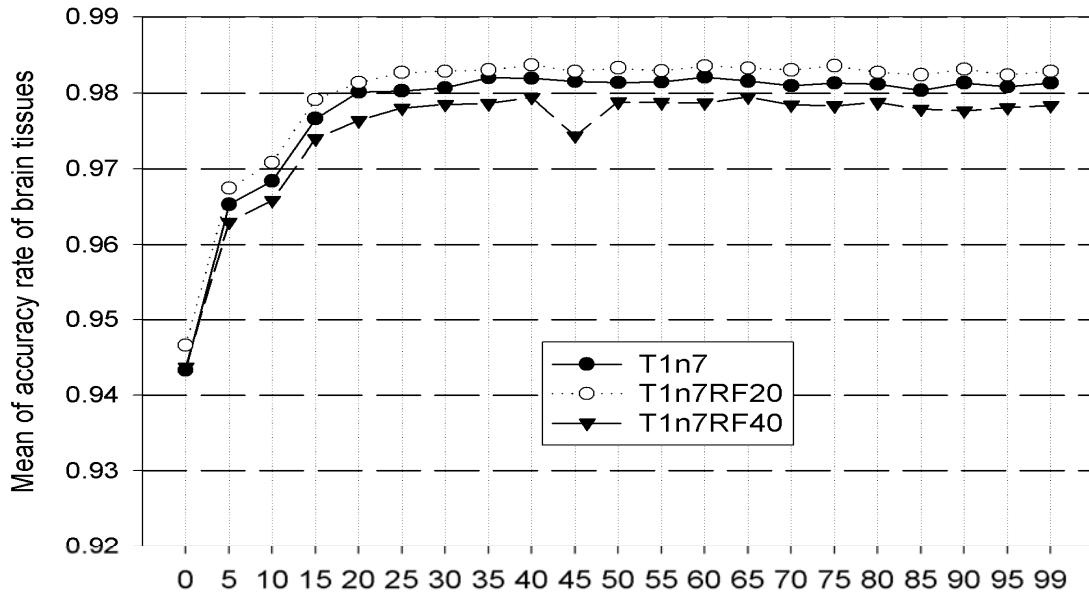


**Figure 4.4** Images segmented from simulated phantom MR images with different spatial features and various noise and inhomogeneity levels.

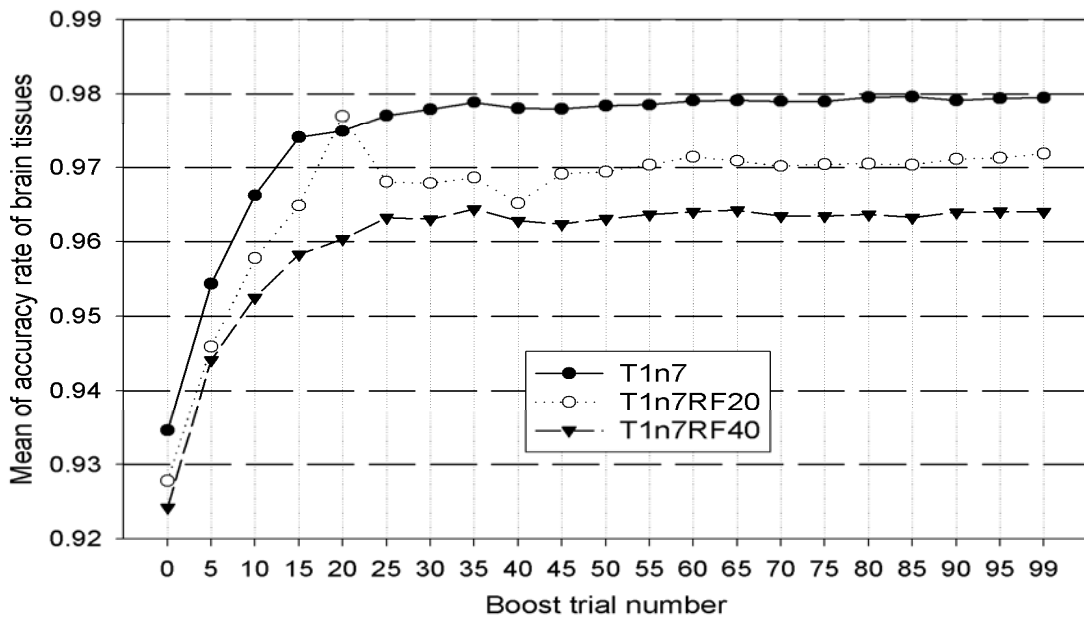
#### 4.3.2. Segmentation of SBMR images

SBMR images with different noise and inhomogeneity levels were segmented using the boosted decision tree algorithm with spatial features  $(G, x, y)$ ,  $(S, x, y)$ ,  $(G, x, y, r, \theta)$ ,  $(S, x, y, r, \theta)$ ,  $(W, x, y, G, r, \theta)$ , and  $(W, x, y, G, r, \theta, S)$ . Image segmentation decision tree performance was best using spatial features  $(G, x, y, r, \theta)$  and  $(S, x, y, r, \theta)$  in SBMR images. Figure 4.5 depicts the average brain tissue segmentation accuracy using the boosted decision tree. Figure 4.5(a) depicts the average segmentation accuracy using spatial feature  $(G, x, y, r, \theta)$  in SBMR images with noise and inhomogeneity levels of T1n7, T1n7RF20, and T1n7RF40. Figure 4.5(b) depicts the average segmentation accuracy with spatial feature  $(S, x, y, r, \theta)$  in SBMR images with noise and inhomogeneity levels of T1n7, T1n7RF20, and T1n7RF40. Critical average accuracy rates were obtained using a decision tree with a boost trial number of 20. Greater boost trials resulted in a longer processing time. Therefore, the decision tree with 20

boost trials was selected to segment all simulated brain MR images, as shown in Figure 4.5. Figures 4.6(a)-(c) show the accuracy of segmenting GM, WM, and CSF, respectively, using spatial feature  $(G, x, y, r, \theta)$  on SBMR images with different noise levels and inhomogeneities. The accuracy decreased for GM, WM, and CSF when segmented with spatial feature  $(G, x, y, r, \theta)$  and combined with noise levels increased from 3% to 9%. Figures 4.6(d)-(f) show the accuracy of segmenting GM, WM, and CSF using spatial feature  $(S, x, y, r, \theta)$  on SBMR images with different noise levels and inhomogeneities. Accuracy rates decreased for GM, WM, and CSF when segmented with  $(G, x, y, r, \theta)$  and including noise levels increased from 3% to 9%. Row 1 in Figure 4.7 depicts a standard image (manually labeled by an expert). The images in column 1 of Figure 4.7 show the original simulated brain MR images using T1n7, T1n7RF20, and T1n7RF40. The images in column 2 of Figure 4.7 show simulated brain MR images segmented with spatial feature  $(G, x, y, r, \theta)$  and noise and inhomogeneity levels of T1n7, T1n7RF20, and T1n7RF40. The images in column 3 of Figure 4.7 show SBMR images segmented with spatial feature  $(S, x, y, r, \theta)$  and noise and inhomogeneity levels of T1n7, T1n7RF20, and T1n7RF40. The boosted decision tree algorithm performed better clarity of brain tissue segmentation than that of original images. The inset images in Figure 4.7 show the original and segmented SBMR images, and illustrate clear distinctions in the three brain tissues. The inset images in rows 1, 2, and 3 are 3x magnifications of boxed-in locations in the original images. These three locations were difficult to segment because of their complexity. The method was also demonstrated to segment a complete coronal SBMR images. Figure 4.8 shows an example of a 3D surface rendering using the segmented image data, as determined by the boosted decision tree from SBMR data with T1n7RF20, consisting of 181 slices. The brain was respectively segmented into white matter hemisphere (labeled in yellow) and gray matter hemisphere (labeled in orange).



(a)



(b)

**Figure 4.5** Mean accuracy rates of tissue segmentation from simulated brain MR images. (a) Mean accuracy rates of tissue segmentation using the decision tree and 20 boost trials with spatial feature ( $G x, y, r, \theta$ ) from simulated MR images with noise and inhomogeneity levels T1n7, T1n7RF20, and T1n7RF40. (b) Mean accuracy rates of tissue segmentation using the decision tree combined with 20 boost trials using spatial feature ( $S x, y, r, \theta$ ) from simulated MR images with noise and inhomogeneity levels T1n7, T1n7RF20, and T1n7RF40.

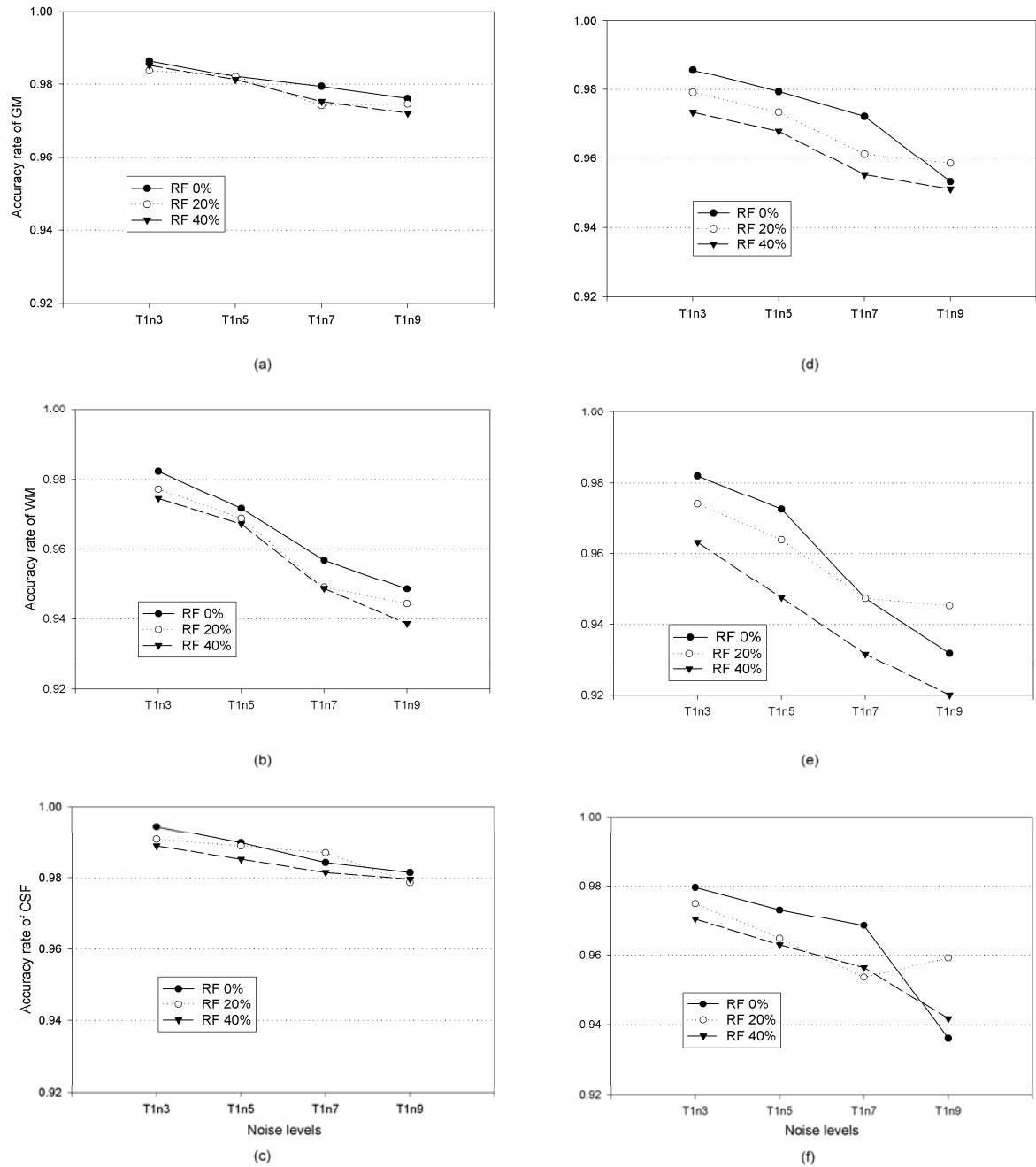


**Figure 4.6** Accuracy rates of tissue segmentation using a boosted decision tree algorithm on simulated brain MR images. (a) Accuracy rates of GM segmentation using spatial feature ( $G x, y, r, \theta$ ). (b) Accuracy rates of WM segmentation using spatial feature ( $G x, y, r, \theta$ ). (c) Accuracy rates of CSF segmentation with spatial feature ( $G x, y, r, \theta$ ). (d) Accuracy rates of GM segmentation with spatial feature ( $S x, y, r, \theta$ ). (e) Accuracy rates of WM segmentation using spatial feature ( $S x, y, r, \theta$ ). (f) Accuracy rates of CSF segmentation using spatial feature ( $S x, y, r, \theta$ ).

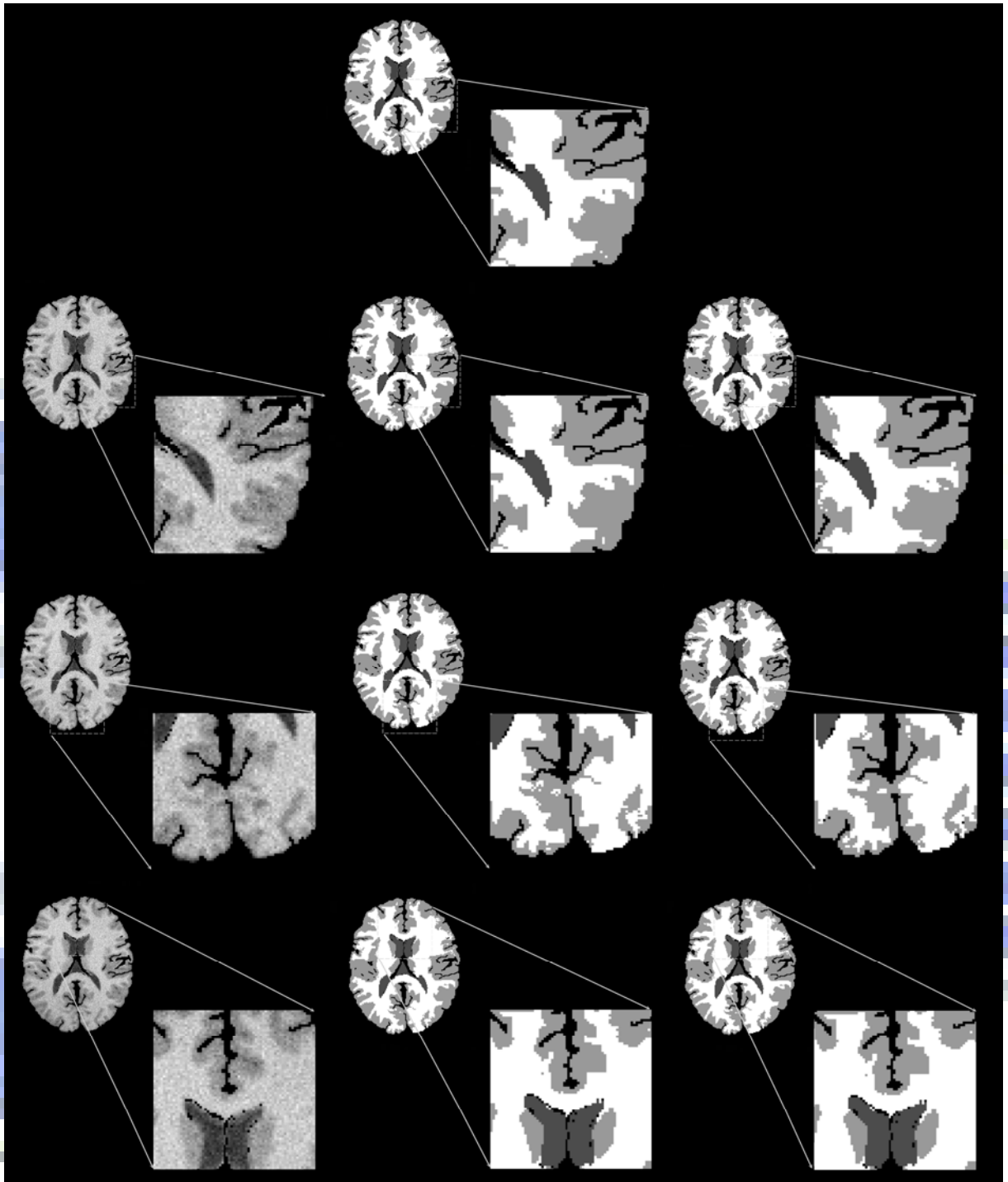


**Figure 4.7** Segmentation of simulated brain MR images from BrainWeb. Row 1 depicts the original, unsegmented image, and rows 2 through 4 show noise and inhomogeneity levels T1n7, T1n7RF20, and T1n7RF40. Images in column 1 are the original images, images in column 2 are segmented with spatial feature  $(G, x, y, r, \theta)$ , and those in column 3 are segmented with spatial feature  $(S, x, y, r, \theta)$ . All blown-up images were taken from the boxed-in region of the shown whole brain horizontal slice and enlarged three times.

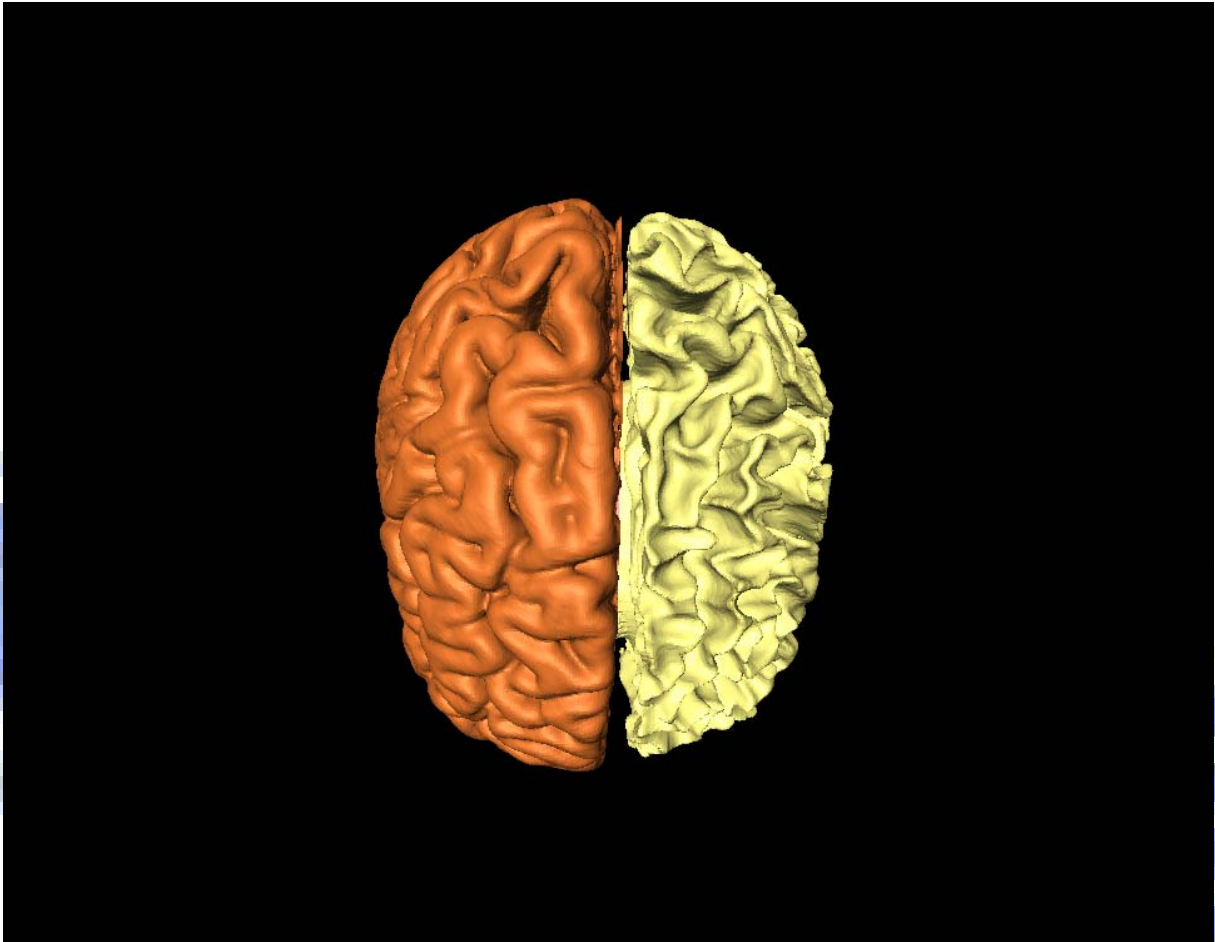


**Figure 4.8** A 3D reconstruction of segmented brain image data in axial view. The brain has been segmented into gray matter (labeled in orange) and white matter (labeled in yellow).

#### **4.3.3. Comparison of segmentation with the other algorithms**

The results of segmentation using the boosted decision tree were also compared with another two segmentation algorithms. One is in the Medical Imaging Interaction Toolkit (MITK, <http://www.mitk.org/>) whose principle is based on a statistical region-growing (SRG) algorithm in Insight Toolkit (ITK, <http://www.itk.org/>) [114]. The other is adaptive segmentation (AS) algorithm for MRI data that uses the knowledge of tissue intensity properties through the expectation maximization (EM) algorithm to more accurately segment brain MR images [115]. Table 4.1 shows the accuracy rates of GM, WM, and CSF segmentation using the boosted decision tree with spatial features ( $G, x, y, r, \theta$ ) and ( $S, x, y, r,$



$\theta$ ), the SRG, and the AS algorithm from SBMR images with different noise levels and inhomogeneities. The accuracy rates of GM, WM, and CSF segmentation using the boosted decision tree with spatial features  $(G, x, y, r, \theta)$  and  $(S, x, y, r, \theta)$  at all noise levels and inhomogeneities were higher than those of SRG and AS algorithm.

The  $k$  index or similarity index was also used to compare segmentation performance. Table 4.2 summarizes the  $k$  indices of segmented GM, WM, and CSF from SBMR images using the boosted decision tree with spatial features  $(G, x, y, r, \theta)$  and  $(S, x, y, r, \theta)$ , the SRG and the AS algorithm from SBMR with different noise levels and inhomogeneities. The  $k$  values of segmented GM, WM, and CSF using the boosted decision tree with spatial features  $(G, x, y, r, \theta)$  and  $(S, x, y, r, \theta)$  were higher than 0.9312, 0.9464, and 0.9547, respectively. The  $k$  indices of GM, WM, and CSF segmentation using the boosted decision tree and a fuzzy threshold were much higher than those using SRG and AS algorithm in several different noise levels and inhomogeneities from SBMR images.

**Table 4.1** Segmentation accuracy rates from SBMR images using the boosted decision tree, the SRG, and the AS algorithm.

	GM				WM				CSF			
	$(G, x, y, r, \theta)$	$(S, x, y, r, \theta)$	SRG	AS	$(G, x, y, r, \theta)$	$(S, x, y, r, \theta)$	SRG	AS	$(G, x, y, r, \theta)$	$(S, x, y, r, \theta)$	SRG	AS
T1n3	0.9865	0.9857	0.6577	0.9349	0.9822	0.9819	0.9726	0.8329	0.9944	0.9796	0.6958	0.8148
T1n5	0.9822	0.9794	0.7999	0.8873	0.9715	0.9724	0.9386	0.8576	0.9898	0.9731	0.7370	0.8250
T1n7	0.9794	0.9722	0.9051	0.8254	0.9568	0.9609	0.8250	0.8325	0.9842	0.9685	0.7610	0.8407
T1n9	0.9760	0.9532	0.9125	0.8099	0.9485	0.9319	0.5909	0.7033	0.9814	0.9361	0.7824	0.8407
T1n3RF20	0.9839	0.9791	0.7448	0.9329	0.9771	0.9739	0.9636	0.8314	0.9907	0.9750	0.7169	0.7972
T1n5 RF20	0.9822	0.9734	0.7885	0.8986	0.9687	0.9638	0.9296	0.8535	0.9888	0.9648	0.7301	0.8000
T1n7 RF20	0.9742	0.9613	0.9026	0.8178	0.9490	0.9472	0.8357	0.8503	0.9870	0.9537	0.7625	0.8222
T1n9 RF20	0.9746	0.9585	0.9625	0.8182	0.9443	0.9452	0.3962	0.6364	0.9787	0.9592	0.7959	0.8463
T1n3RF40	0.9853	0.9734	0.7761	0.9514	0.9743	0.9631	0.9471	0.7438	0.9888	0.9703	0.7112	0.7630
T1n5 RF40	0.9812	0.9679	0.8705	0.8786	0.9671	0.9474	0.8908	0.8374	0.9851	0.9629	0.7424	0.8056
T1n7 RF40	0.9753	0.9552	0.9470	0.8319	0.9486	0.9316	0.6601	0.7433	0.9814	0.9564	0.7698	0.8333
T1n9 RF40	0.9721	0.9511	0.9593	0.8077	0.9386	0.9201	0.4859	0.6591	0.9796	0.9416	0.7925	0.8333

**Table 4.2** The segmentation  $k$  indexes from SBMR images using the boosted decision tree, the SRG, and the AS algorithm.

	GM				WM				CSF			
	$(G, x, y, r, \theta)$	$(S, x, y, r, \theta)$	SRG	AS	$(G, x, y, r, \theta)$	$(S, x, y, r, \theta)$	SRG	AS	$(G, x, y, r, \theta)$	$(S, x, y, r, \theta)$	SRG	AS
T1n3	0.9839	0.9814	0.7620	0.8680	0.9850	0.9863	0.8671	0.8948	0.9898	0.9828	0.8192	0.7917
T1n5	0.9757	0.9728	0.8405	0.8556	0.9775	0.9797	0.9032	0.8941	0.9861	0.9790	0.8458	0.7661
T1n7	0.9663	0.9632	0.8495	0.8107	0.9683	0.9721	0.8767	0.8666	0.9815	0.9725	0.7427	0.7028
T1n9	0.9602	0.9384	0.7973	0.7455	0.9624	0.9522	0.7348	0.7909	0.9774	0.9546	0.7571	0.6442
T1n3RF20	0.9797	0.9738	0.8174	0.8654	0.9811	0.9806	0.8921	0.8921	0.9879	0.9804	0.8342	0.7863
T1n5 RF20	0.9742	0.9740	0.8357	0.8585	0.9759	0.9651	0.9072	0.8929	0.9852	0.9742	0.8408	0.7721
T1n7 RF20	0.9834	0.9503	0.8557	0.8137	0.9667	0.9628	0.8846	0.8761	0.9691	0.9662	0.7474	0.6815
T1n9 RF20	0.9572	0.9476	0.7729	0.7252	0.9594	0.9610	0.5650	0.7570	0.9759	0.9709	0.8745	0.5995
T1n3RF40	0.9787	0.9648	0.8297	0.8332	0.9801	0.9738	0.8943	0.8404	0.9879	0.9757	0.8294	0.8000
T1n5 RF40	0.9745	0.9542	0.8613	0.8405	0.9726	0.9648	0.8963	0.8801	0.9847	0.9733	0.8498	0.7449
T1n7 RF40	0.9597	0.9390	0.8222	0.7745	0.9621	0.9544	0.7819	0.8275	0.9787	0.9672	0.7505	0.6329
T1n9 RF40	0.9528	0.9312	0.7804	0.7270	0.9554	0.9464	0.6494	0.7699	0.9769	0.9594	0.7634	0.5927

#### 4.3.4. Segmentation of real data in brain MR images

The boosted decision tree, SRG, and AS algorithm were also used to segment real data from brain MR images. Two subjects (A and B) of brain MR images were segmented for this experiment. Table 4.3 summarizes the results in terms of the accuracy rate and  $k$  index for a real data experiment. The accuracies of GM, WM, and CSF from subject A segmented using the boosted decision tree with  $(G, x, y, r, \theta)$ ,  $(S, x, y, r, \theta)$ ,  $(W, x, y, G, r, \theta)$ , and  $(W, x, y, G, r, \theta, S)$  were higher than 0.9973, 0.9979, and 0.9913, respectively. The  $k$  indices of the segmented GM, WM, and CSF from subject A using the boosted decision tree with  $(G, x, y, r, \theta)$ ,  $(S, x, y, r, \theta)$ ,  $(W, x, y, G, r, \theta)$ , and  $(W, x, y, G, r, \theta, S)$  were higher than 0.9942, 0.9978, and 0.9932, respectively. The accuracy rates of segmented GM, WM, and CSF from subject B using the boosted decision tree with  $(G, x, y, r, \theta)$ ,  $(S, x, y, r, \theta)$ ,  $(W, x, y, G, r, \theta)$ , and  $(W, x, y, G, r, \theta, S)$  were higher than 0.9967, 0.9987, and 0.9922, respectively. The  $k$  indices of segmented GM, WM, and CSF from subject B using the boosted decision tree with  $(G, x, y, r, \theta)$ ,  $(S, x, y, r, \theta)$ ,  $(W, x, y, G, r, \theta)$ , and  $(W, x, y, G, r, \theta, S)$  were higher than 0.9963, 0.9984, and 0.9942, respectively. The accuracy rates and  $k$  indices of segmented GM, WM, and CSF using the boosted decision tree with  $(G, x, y, r, \theta)$ ,  $(S, x, y, r, \theta)$ ,  $(W, x, y, G, r, \theta)$ , and  $(W, x, y, G, r, \theta, S)$  exhibited much higher performance than those using SRG and AS segmentation algorithm from real data.

Figure 4.9 depicts segmented images using the boosted decision tree and the other segmentation algorithm. Images in rows 1 and 2 of Figure 4.9 were obtained from subjects A and B. Images in column 1 of Figure 4.9 show the original MR images from subjects A and B. Images in column 2 of Figure 4.9 show images corresponding to column 1 that were segmented using the boosted decision tree with spatial features  $(G, x, y, r, \theta)$ . Images in column 3 of Figure 4.9 show images segmented with the SRG algorithm. Images in column 4 of Figure 4.9 show images segmented with the AS algorithm. Clear tissue regions were identified from real segmented brain image data using the boosted decision tree, whereas

unclear regions and artifacts existed in the original images and those segmented with the SRG and AS algorithm. It is, therefore, clear that visually apparent artifacts in MR images of real brains are reduced when using the boosted decision tree.



**Table 4.3** Segmentation of MR images from two real subjects using the boosted decision tree, the SRG, and the AS method.

Subject	Spatial feature	GM	WM	CSF	
Subject A	Accuracy	$(G, x, y, r, \theta)$	0.9974	0.9979	0.9913
		$(S, x, y, r, \theta)$	0.9973	0.9987	0.9897
		$(W, x, y, G, r, \theta)$	0.9984	0.9989	0.9968
		$(W, x, y, G, r, \theta, S)$	0.9982	0.9988	0.9963
	SRG	0.7407	0.8624	0.1508	
	AS	0.6364	0.9169	0.6224	
	$k$	$(G, x, y, r, \theta)$	0.9957	0.9978	0.9944
		$(S, x, y, r, \theta)$	0.9942	0.9979	0.9932
		$(W, x, y, G, r, \theta)$	0.9983	0.9987	0.9977
		$(W, x, y, G, r, \theta, S)$	0.9980	0.9986	0.9975
SRG		0.6735	0.8004	0.2615	
AS		0.6889	0.7811	0.7432	
Subject B	Accuracy	$(G, x, y, r, \theta)$	0.9973	0.9987	0.9955
		$(S, x, y, r, \theta)$	0.9967	0.9988	0.9922
		$(W, x, y, G, r, \theta)$	0.9969	0.9992	0.9977
		$(W, x, y, G, r, \theta, S)$	0.9972	0.9994	0.9980
	SRG	0.6635	0.9085	0.1579	
	AS	0.5432	0.9564	0.6223	
	$k$	$(G, x, y, r, \theta)$	0.9973	0.9987	0.9966
		$(S, x, y, r, \theta)$	0.9963	0.9984	0.9942
		$(W, x, y, G, r, \theta)$	0.9984	0.9987	0.9979
		$(W, x, y, G, r, \theta, S)$	0.9988	0.9989	0.9982
SRG		0.6195	0.8400	0.2725	
AS		0.6231	0.8259	0.7434	

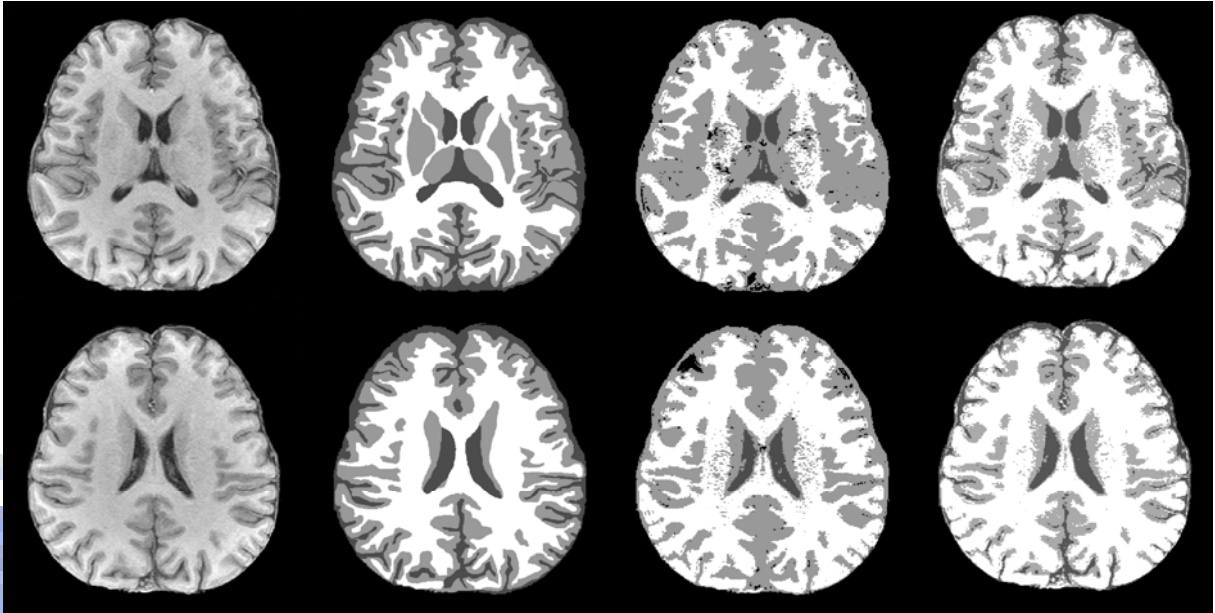


**Figure 4.9** Segmentation of real brain MR imaging data. Images in column 1 show the original brain MR images of subjects A and B. Images in column 2 correspond to those in column 1 and were segmented using the boost decision tree with spatial feature  $(G, x, y, r, \theta)$ . Images in column 3 correspond to those in column 1 and were segmented with the SRG algorithm. Images in column 4 correspond to those in column 1 and were segmented with the AS algorithm.

#### 4.4. Discussions

We found better separation of intensity distributions for each region when using the decision tree than in the original SPMR images, indicating increased accuracy. Moreover, similar accuracies were found when SPMR images were segmented using decision trees with and without boost trials (data not shown). In all regions, accuracies of segmentation from SPMR images using decision tree algorithms with spatial features  $(G, x, y, r, \theta)$ , and  $(S, x, y, r, \theta)$  as well as Var15, Var15RF20, Var15RF40, Var30, Var30RF20, Var30RF40 were the highest (Figure 4.3). These two spatial features were, therefore, used to segment the SBMR images. The lowest accuracy rates were obtained with spatial features  $(W, x, y, G, r, \theta)$ , and  $(W, x, y, G, r, \theta, S)$  because the overlapping intensity of each region was greater when spatial feature  $(W)$

was included (Figure 3.1). Segmentation was poorest when using the decision tree algorithm on SPMR images with Var30, Var30RF20, and Var30RF40 due to larger noise variations in phantom images thus leading to increased overlap of image intensity.

The intensity distribution of each tissue in the SBMR images overlapped more and was more complex than in the SPMR images. The increased noise levels or RF inhomogeneities of SBMR images often cause greater image intensity distribution overlap. The SBMR images were more difficult to correctly segment, and as such, the boosted decision tree was proposed. The accuracy rates of SBMR tissue segmentation increased when the boost trial numbers were increased, but at the expense of a longer process, as depicted in Figure 4.5. In order to limit time consumption, we elected to use 20 boost trial numbers in the decision tree algorithm to improve the accuracy of SBMR image tissue segmentation (Figure 4.5). The spatial features  $(G, x, y, r, \theta)$  and  $(S, x, y, r, \theta)$  were selected as inputs to the segmentation algorithm since they provided greater accuracy when tested in SPMR images (Figure 4.3). The accuracy rates of segmented brain tissues using spatial feature  $(G, x, y, r, \theta)$  were higher than those using spatial feature  $(S, x, y, r, \theta)$  since the general gray level ( $G$ ) had less overlap in the intensity distribution for each tissue compared to the spatial gray level ( $S$ ). The local area of spatial feature ( $S$ ) was also larger than that of spatial feature ( $G$ ), as shown in Figure 3.1. Thus, the segmentation accuracy rates were lowest when the spatial features included wavelet transform ( $W$ ). The segmentation accuracy rates using the boosted decision tree algorithm with spatial features  $(G, x, y, r, \theta)$  and  $(S, x, y, r, \theta)$  decreased when the noise levels in brain MR images increased (Figure 4.6). The accuracy rates also decreased when the noise levels increased in conjunction with 20% or 40% RF inhomogeneities. There was no significant difference in accuracy between SBMR images with 20% or 40% inhomogeneity since the overlap in the intensity distribution was less affected by inhomogeneities. The decrease in accuracy caused by increased noise was greater than that caused by inhomogeneities.

More complicated statistical analyses or parameter adjustments are often implemented to



further enhance accuracy. Several studies have examined the accuracy of MR segmentation [42, 43, 48, 53, 94]. Marroquin *et al.* [42] studied automatic segmentation of brain MR images. Their validation was only performed on GM and WM. Archibald *et al.* [53] stressed the importance of improving the accuracy evaluated by the  $k$  index; however, their validation of brain MR was also limited to WM and GM. Anbeek *et al.* [48] performed probability segmentation of brain tissue on MR imaging with similarity indices of 0.893 for WM, 0.830 for GM, and 0.819 for CSF. Greenspan *et al.* [43] performed automatic segmentation of brain MR images from BrainWeb. The validation of segmentation was performed with maximum Dice coefficients of 0.889 for GM, 0.920 for WM, and 0.742 for CSF on T1-weighted MR imaging with a noise level of 9%. Yu *et al.* [94] segmented brain MR images from BrainWeb that had been validated with an average overlap metric (AOM) of 0.9 for WM on T1-weighted imaging with a noise level of 3% and RF of 0%. These studies addressed the importance of improving tissue segmentation accuracy in MR images. In the present study, segmentation errors were observed to decrease when the boost number was increased, while correct segmentation was not impacted by noise effects on the fuzzy threshold. The boosted decision tree algorithm combined with a fuzzy threshold performed well and accurately for SBMR image segmentation. The accuracy rates of GM, WM, and CSF segmentation using the boosted decision tree with spatial features  $(G, x, y, r, \theta)$  at all noise levels and inhomogeneities were higher than 0.9721, 0.9386, and 0.9787, respectively (Table 4.1). The highest accuracy rates were obtained when  $(G, x, y, r, \theta)$  was used to classify the SBMR images. Increased boost trials provided more accurate results for SBMR imaging. Higher values of the accuracy were obtained in SBMR images when using the boosted decision tree combined with a fuzzy threshold as compared to SRG and AS for other research methods (Table 4.1). Thus, the boosted decision tree algorithm demonstrates improved tissue (GM, WM, and CSF) segmentation performance in SBMR images, and significantly improves the accuracy therein.

The  $k$  values of segmented GM, WM, and CSF using the boosted decision tree with

spatial features ( $G, x, y, r, \theta$ ) were higher than 0.9528, 0.9554, and 0.9769, respectively (Table 4.2). The  $k$  index and accuracy rate were both used to evaluate the performance of the decision tree combined with boosting and a fuzzy threshold against SRG and AS algorithm. Higher values of the  $k$  index were obtained using the boosted decision tree compared to using the SRG and AS algorithm (Table 4.2). The observed decrease of these values in the presence of increased SBMR noise was greater for the SRG and AS method than for the boosted decision tree algorithm. Noise levels and inhomogeneities did not appreciably impact brain tissue segmentation using the decision tree combined with boost trials and a fuzzy threshold. As a real application, brain MR images from two subjects were segmented using the boosted decision tree, the SRG and AS algorithm. The values of the  $k$  index and accuracy of segmented GM, WM, and CSF from a real data using the boosted decision tree with ( $G, x, y, r, \theta$ ), ( $S, x, y, r, \theta$ ), ( $W, x, y, G, r, \theta$ ), and ( $W, x, y, G, r, \theta, S$ ) were greater than 0.99. Higher values of the  $k$  index and accuracy were produced by the boosted decision tree in comparison to the SRG and AS method on real data (Table 4.3). The boosted decision tree successfully segmented the tissues in MR-imaged real brains, and exhibited enhanced clarity of brain tissue (Figure 3.10). Thus, the boosted decision tree algorithm is equally suitable for brain tissue (GM, WM, and CSF) segmentation in real MR images with improved accuracy.

In conclusion, the present work have demonstrated an automatic method, boosted decision tree algorithm, for segmenting MR images. We presented a supervised approach to classification-created MR images, wherein structures of interest are precisely addressed by a decision tree combined with boost trials and a fuzzy threshold.

The decision tree successfully segmented the SPMR images, and the boosted decision tree algorithm improved the accuracy of tissue segmentation from SBMR images. Furthermore, the spatial features ( $G, x, y, r, \theta$ ) and ( $S, x, y, r, \theta$ ) were used to combine the general gray level and spatial gray level with Euclidean coordinates ( $x, y$ ) or polar coordinates ( $r, \theta$ ) for image preprocessing. The highest accuracy rates and  $k$  indices of brain tissue

segmentation were obtained when the spatial feature  $(G, x, y, r, \theta)$  was used to classify the SBMR images. The appreciated boost trials were demonstrated to obtain more accurate results on SBMR images. The boosted decision tree algorithm also improved the accuracy of tissue segmentation from a real data. Therefore, the boosted decision tree algorithm is suitable for tissue (GM, WM, CSF) segmentation of brain MR images and provides improved accuracy for brain tissue segmentation.



## **Chapter 5    Improving Segmentation of Brain MR images Based on a Boosted Decision Tree through Preprocessing by the Multiscale Retinex Algorithm**

### **5.1. Introduction**

To improve clinical diagnosis, it is both very important to increase the segmentation accuracy of brain MR image and achieve high quality of segmentation. In this Chapter, we will propose a segmentation method combined MSR and BDT algorithm through preprocessing by the intensity inhomogeneity correction to increase the segmentation accuracy of the GM, WM, and CSF in brain MR images and to achieve the high quality of segmentation for anatomical structures.

We have successfully corrected brain MR images from phantom and animal data in Chapter 2 and have successfully improved the segmentation accuracy of brain tissues of MR image from SPMR images, SBMR images, and a real data in Chapter 3 and Chapter 4. Therefore, we proposed a BDT algorithm combined with preprocessing by the MSR algorithm MSR algorithm to classify brain tissues as GM, WM, and CSF with the goal of improving accuracy rates of brain MR image segmentation.

### **5.2. Materials and methods**

#### **5.2.1. MR data in this experiment**

All the experimental simulated MR data sets are the same as those in Chapter 3 and Chapter 4. About the brain MR images, we choose T1-weighted brain MR image with matrix size of  $181 \times 217$  from SBMR images with T1n3, T1n5, T1n7, T1n9, T1n3RF20, T1n5RF20, T1n7RF20, T1n9RF20, T1n3RF40, T1n5RF40, T1n7RF40, and T1n9RF40.

## 5.2.2. Methods

### 1) Image segmentation procedure

Figure 5.1 shows the image processing procedures that are image preprocessing and image segmentation. The image preprocessing includes two ways: one is RF inhomogeneity correction by multiscale retinex and then to extract the spatial features from the MR images, the other is to extract spatial features only. The multiscale retinex algorithm in the image preprocessing step was applied to enhance tissue contrast of the MR image by correcting the inhomogeneity for improving the brain tissue segmentation. The segmentation algorithm, the decision trees (CART or BDT), were then used to segment MR images in this study. The decision tree was trained from a standard image (an expert manually identified) and then used to predict the classes of brain tissues.

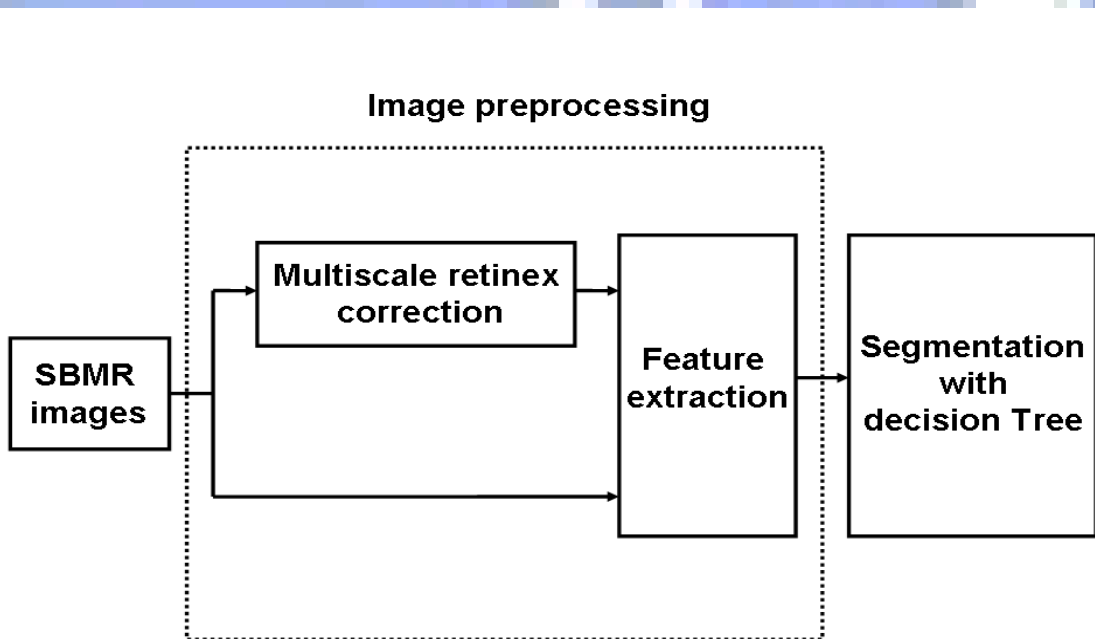


**Figure 5.1** Image processing procedures in this experiment.

## 2) Multiscale retinex (MSR) correction

The multiscale retinex (MSR) algorithm was used to correct the intensity inhomogeneity from SBMR images in this experiment. The MSR algorithm is the same as the method in Chapter 3. It was used to reduce the effect of RF inhomogeneity and noise for improving the accuracy of segmentation.

## 3) Feature extraction

Feature extraction step is the same as image preprocessing in Chapter 3 and Chapter 4. Spatial features were extracted from every MR image pixel location and used as the input for the segmentation algorithm for image preprocessing. The spatial features used in the present study were:  $G$ ,  $S$ ,  $W$ ,  $x$ ,  $y$ ,  $r$ , and  $\theta$ , where  $G$  represents the gray level intensity of every pixel,  $S$  the spatial gray level of every pixel,  $W$  the coefficients of the wavelet transform,  $(x, y)$  Euclidean coordinates, and  $(r, \theta)$  polar coordinates.

## 4) Segmentation with decision tree

Two kinds of decision tree were used to segment SBMR images in this experiment which are classification and regression tree (CART) and boosted decision tree (BDT). The CART decision tree is the same as the segmentation method in Chapter 3 and the BDT decision tree is the same as the segmentation method in Chapter 4.

## 5.3. Experimental results

### 5.3.1. Results of SBMR images

In order to find the appropriate boost trial number of the decision tree, the SBMR images with T1n9 were tested by using the boosted decision tree with trial number from 0 to 50 but the MSR was not used for image preprocessing. Figure 5.2 shows the average accuracy rates of segmentation using BDT with spatial feature  $(G, x, y, r, \theta)$  and  $(S, x, y, r, \theta)$  from SBMR images with T1n9. The more boost trial numbers were applied, the more time was consumed.

But the lower boost trial numbers were applied, the lower accuracy rates was segmented. The critical average accuracy rates of brain tissue segmentation (GM, WM, and CSF) were obtained using the decision tree with boost trial number of 20. Therefore, the decision tree combined with 20 boost trials were selected as the BDT to segment all SBMR images, as shown in Figure 5.2.

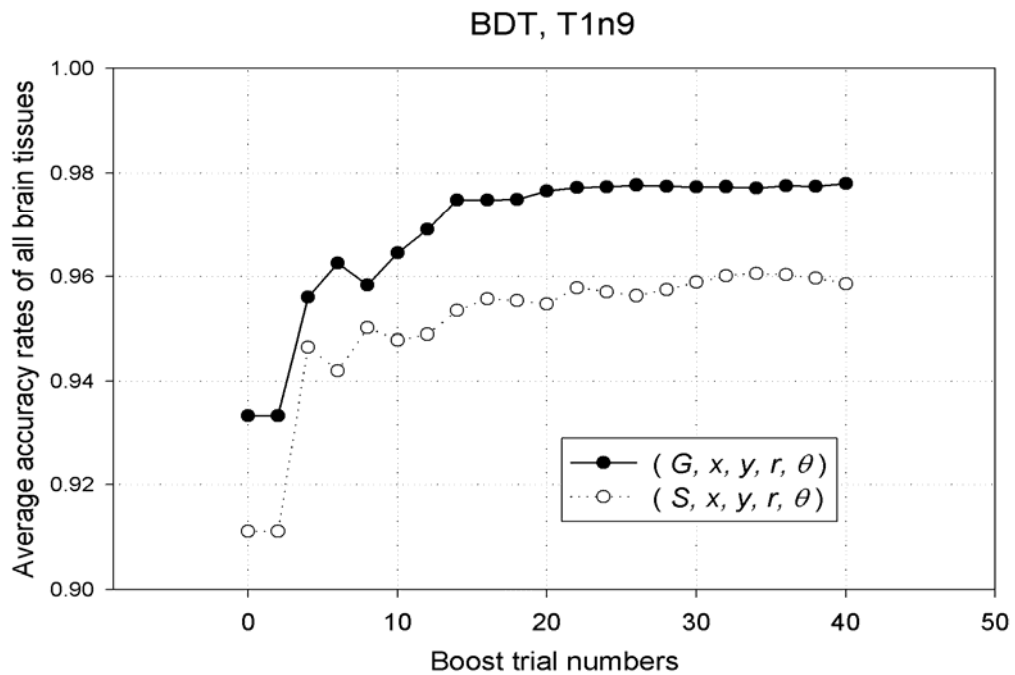


**Figure 5.2** Average accuracy rates of all brain tissues segmented using BDT with spatial feature  $(G, x, y, r, \theta)$  and  $(S, x, y, r, \theta)$  for different boost trial numbers.

Images in row 1 and 2 of Figure 5.3 are T1n3RF20 and T1n9RF40 of SBMR images, respectively. Images in column 1 of Figure 5.3 display the original images. Images in column 2 of Figure 5.3 show the images corrected with MSR algorithm. The corrected images performed more brightness and contrast of brain tissue than the original images. In this present study, the weight  $\omega_n$  and scale of MSR were combined with 15-pixel small-scale SSR weightings of  $\omega_1 = 1/3$ ; 80-pixel moderate-scale SSR weightings of  $\omega_2 = 1/3$ ; and 250-pixel large-scale SSR weightings of  $\omega_3 = 1/3$  [77–82]. Images in column 3 of Figure 5.3 show the images segmented from the corrected images in column 2. The segmented images

clearly performed the brain tissues (GM, WM, and CSF) using the BDT combined with MSR algorithm.

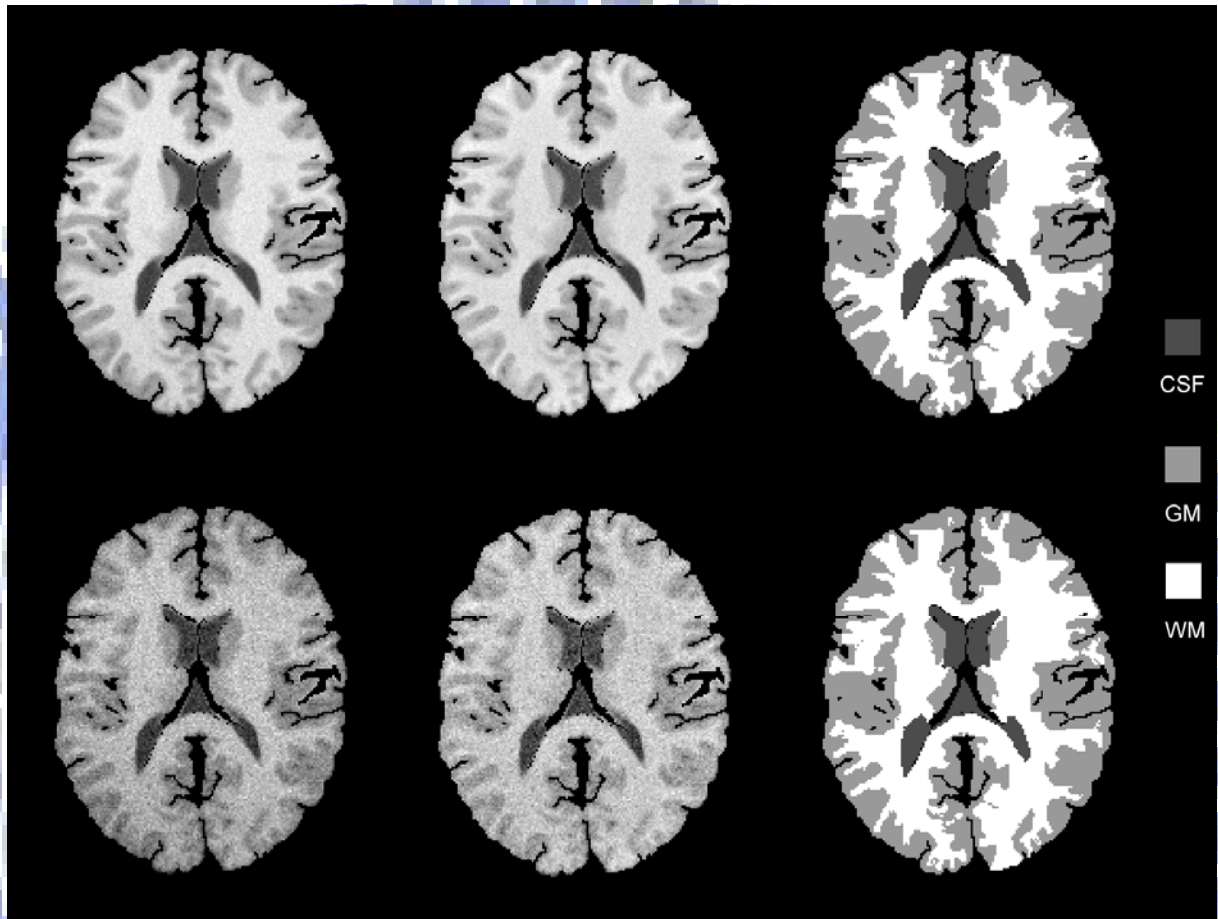


**Figure 5.3** Images from original, corrected using MSR, and segmented using BDT from SBMR with T1n3RF20 and T1n9RF40.

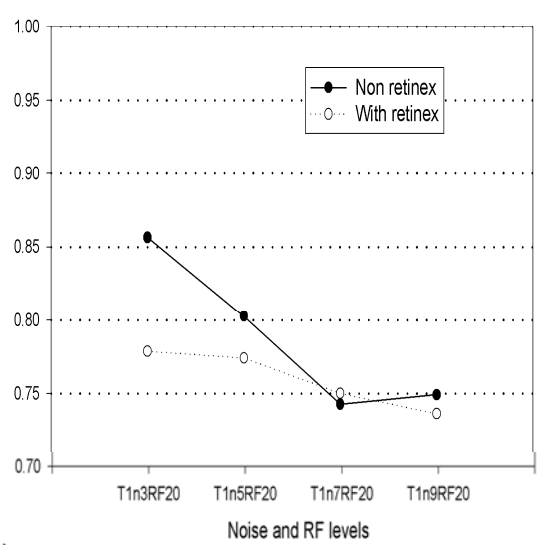
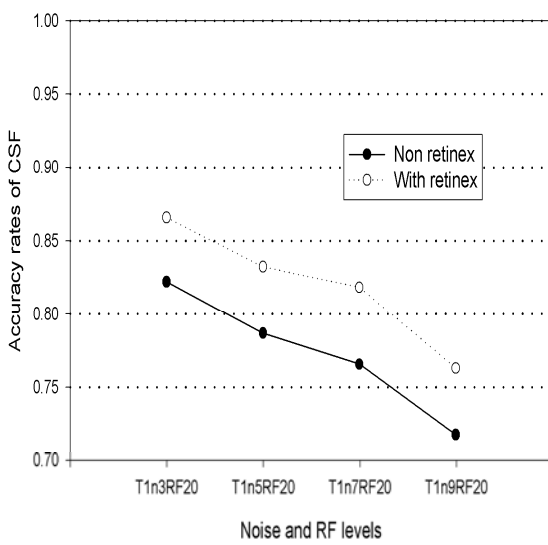
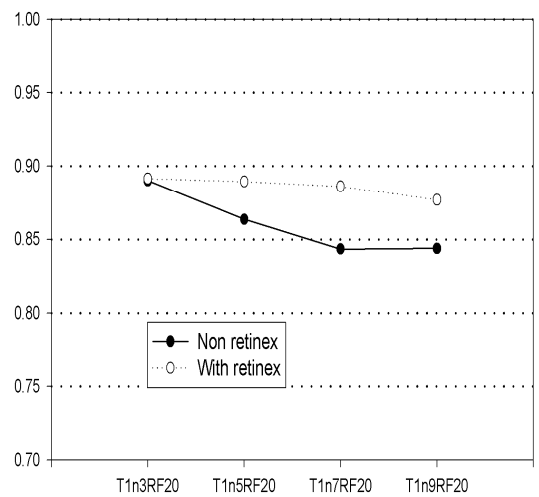
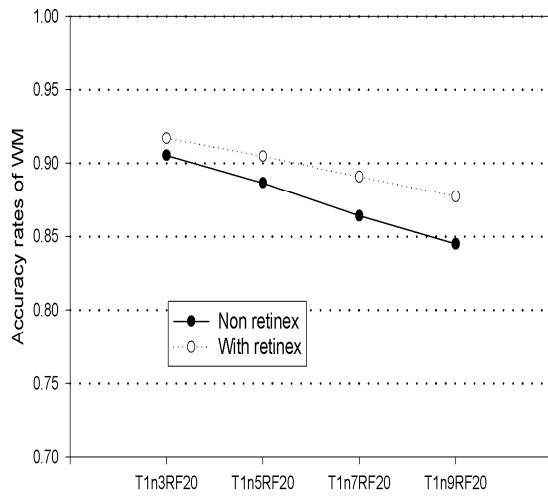
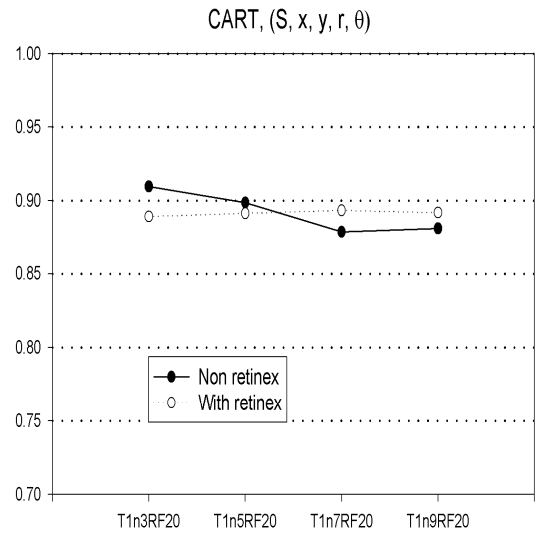
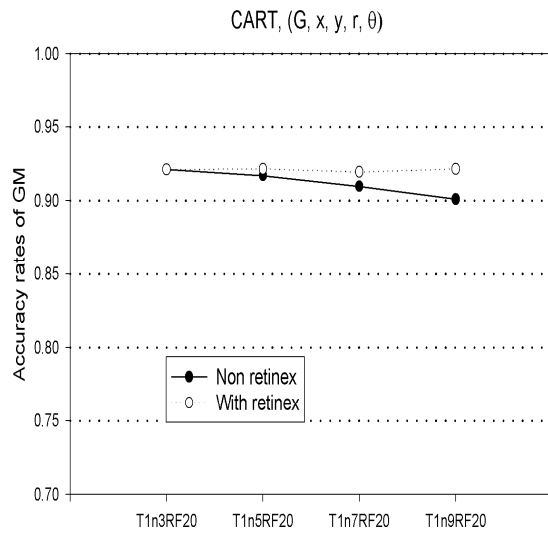
### 5.3.2. Segmentation of SBMR images

Figure 5.4 shows the results of segmentation using CART and BDT from SBMR images with T1n3RF20, T1n5RF20, T1n7RF20, and T1n9RF20. The spatial features  $(G, x, y, r, \theta)$  and  $(S, x, y, r, \theta)$  for feature extraction combined with MSR or non MSR were used for image preprocessing in this study. Curve plots in row 1, 2, and 3 of Figure 5.4(a) show the accuracy rates of GM, WM, and CSF from SBMR images. Curve plots in column 1 and 2 of Figure

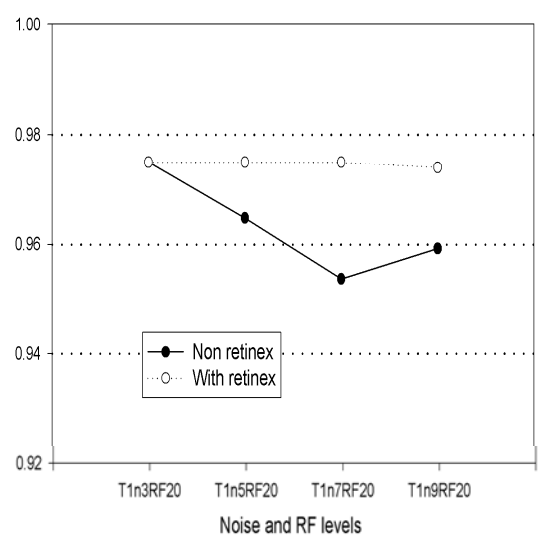
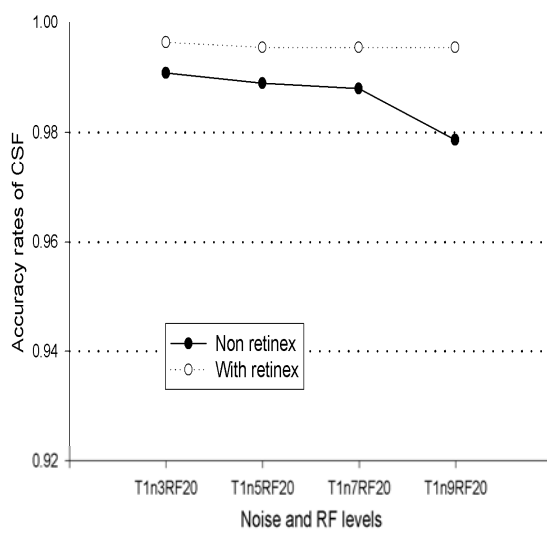
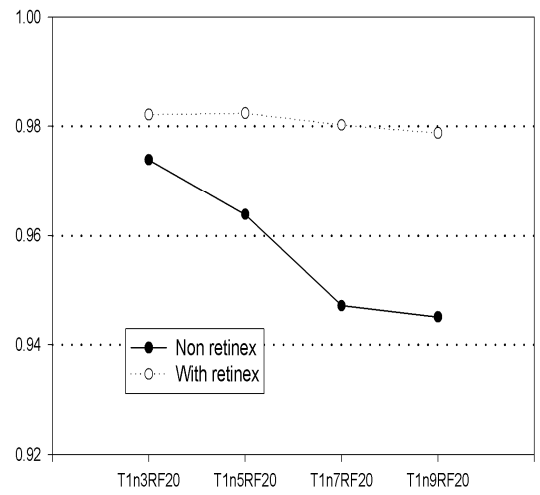
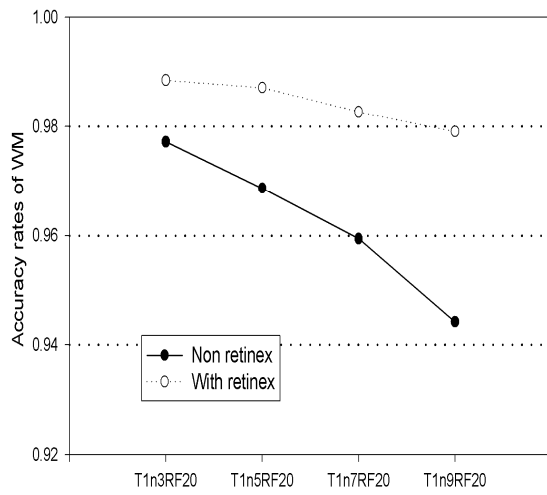
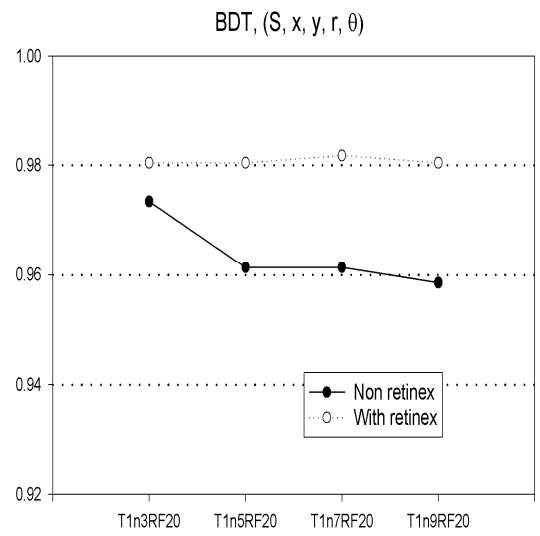
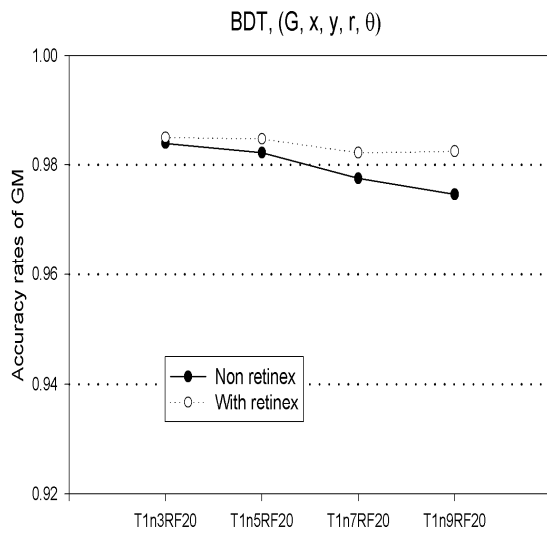


5.4(a) show the results of brain tissue segmentation using CART with spatial feature  $(G, x, y, r, \theta)$  and  $(S, x, y, r, \theta)$ , respectively. Curve plots in row 1, 2, and 3 of Figure 5.4(b) show the accuracy rates of GM, WM, and CSF from SBMR images. Curve plots in column 1 and 2 of Figure 5.4(b) show the results of brain tissue segmentation using BDT with spatial feature  $(G, x, y, r, \theta)$  and  $(S, x, y, r, \theta)$ , respectively.





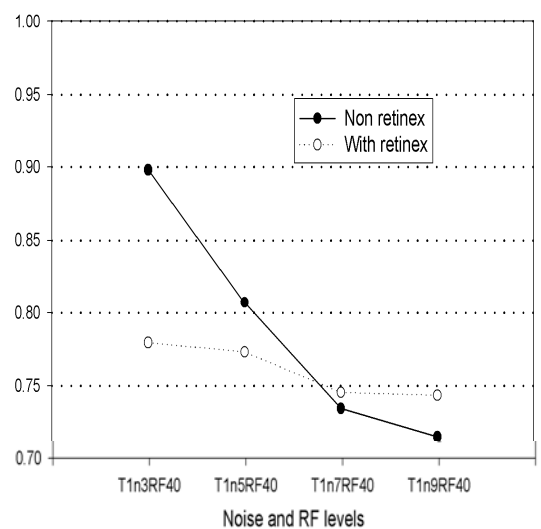
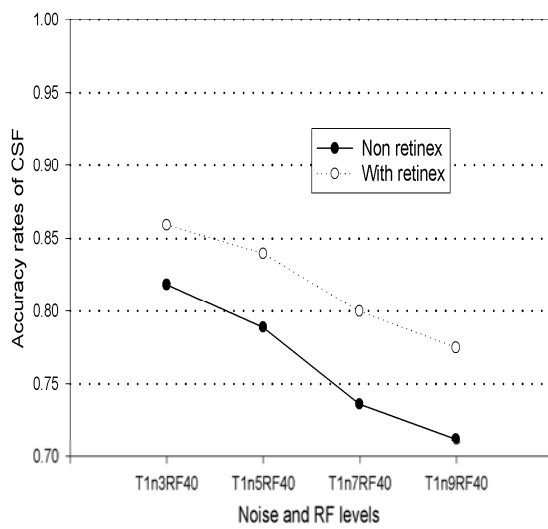
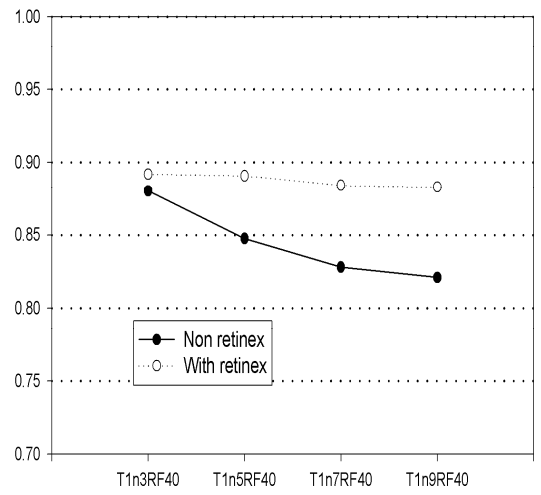
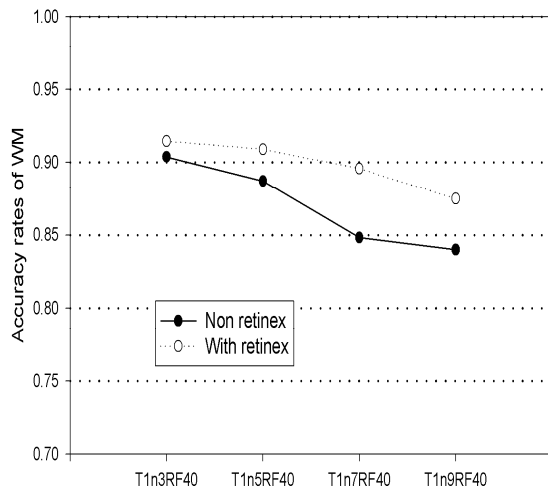
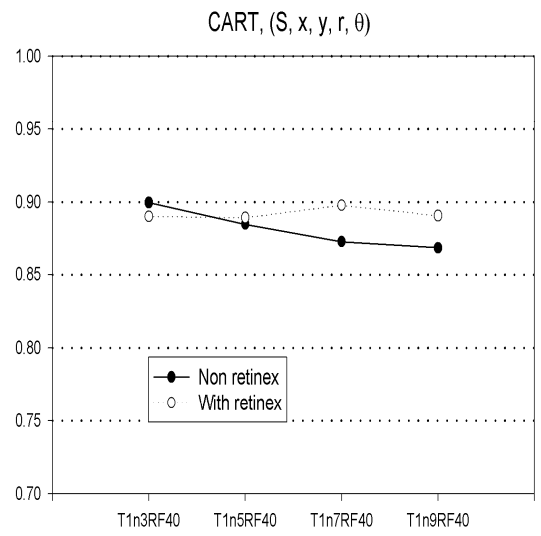
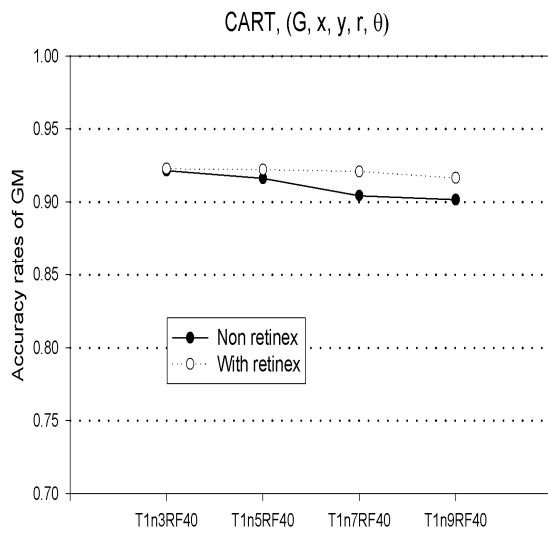
(a)



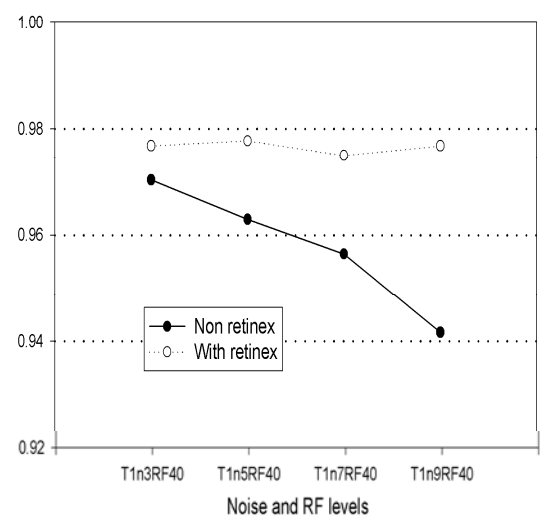
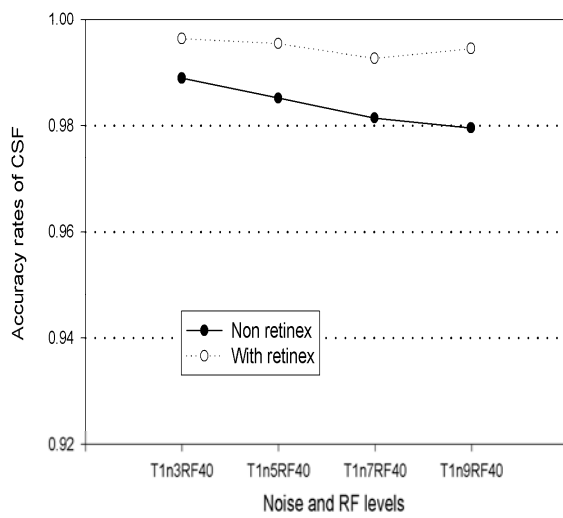
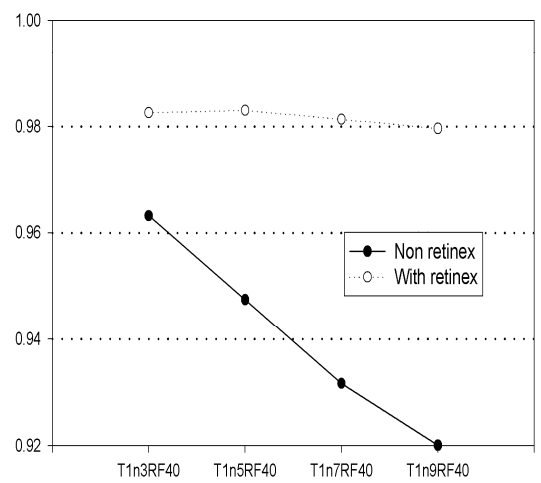
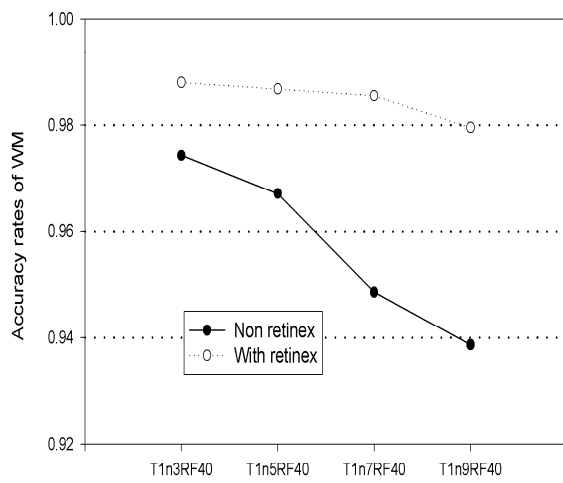
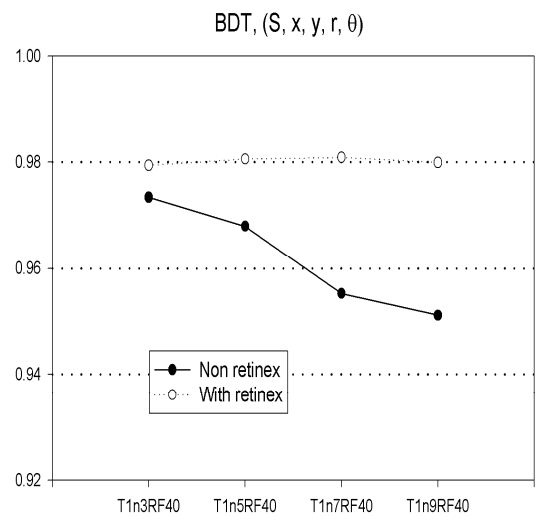
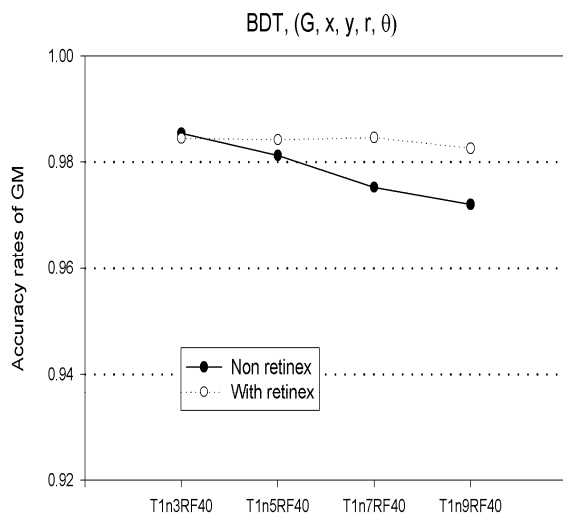
(b)

**Figure 5.4** Accuracy rates of tissue segmentation using a BDT algorithm on SBMR images with T1n3RF20, T1n5RF20, T1n7RF20, and T1n9RF20. (a) Row 1, Accuracy rates of GM. Row 2, Accuracy rates of WM. Row 2, Accuracy rates of CSF. Column 1, segmentation using CART with spatial feature  $(G, x, y, r, \theta)$ . Column 2, segmentation using CART with spatial feature  $(S, x, y, r, \theta)$ . (b) Row 1, Accuracy rates of GM. Row 2, Accuracy rates of WM. Row 2, Accuracy rates of CSF. Column 1, segmentation using BDT with spatial feature  $(G, x, y, r, \theta)$ . Column 2, segmentation using BDT with spatial feature  $(S, x, y, r, \theta)$ .

Figure 5.5 shows the results of segmentation using CART and BDT from SBMR images with T1n3RF40, T1n5RF40, T1n7RF40, and T1n9RF40. The spatial features  $(G, x, y, r, \theta)$  and  $(S, x, y, r, \theta)$  for feature extraction combined with MSR or non MSR were used for image preprocessing in this study. Curve plots in row 1, 2, and 3 of Figure 5.5(a) show the accuracy rates of GM, WM, and CSF from SBMR images with T1n3RF40, T1n5RF40, T1n7RF40, and T1n9RF40. Curve plots in column 1 and 2 of Figure 5.5 show the results of brain tissue segmentation using CART with spatial feature  $(G, x, y, r, \theta)$  and  $(S, x, y, r, \theta)$ , respectively. Curve plots in row 1, 2, and 3 of Figure 5.5(b) show the accuracy rates of GM, WM, and CSF from SBMR images with T1n3RF40, T1n5RF40, T1n7RF40, and T1n9RF40. Curve plots in column 1 and 2 of Figure 5.5(b) show the results of brain tissue segmentation using BDT with spatial feature  $(G, x, y, r, \theta)$  and  $(S, x, y, r, \theta)$ , respectively.



(a)



(b)

**Figure 5.5** Accuracy rates of tissue segmentation using a BDT algorithm on SBMR images with T1n3RF40, T1n5RF40, T1n7RF40, and T1n9RF40. (a) Row 1, Accuracy rates of GM. Row 2, Accuracy rates of WM. Row 2, Accuracy rates of CSF. Column 1, segmentation using CART with spatial feature  $(G, x, y, r, \theta)$ . Column 2, segmentation using CART with spatial feature  $(S, x, y, r, \theta)$ . (b) Row 1, Accuracy rates of GM. Row 2, Accuracy rates of WM. Row 2, Accuracy rates of CSF. Column 1, segmentation using BDT with spatial feature  $(G, x, y, r, \theta)$ . Column 2, segmentation using BDT with spatial feature  $(S, x, y, r, \theta)$ .

## 5.4. Discussions

The appropriate boost trial number 20 was selected to successfully construct the BDT segmentation algorithm with spatial features  $(G, x, y, r, \theta)$  and  $(S, x, y, r, \theta)$  for a series test (trial number 0 to 40) from a SBMR with T1n9 (Figure 5.2). Greater image intensity distribution overlap is often caused by increased noise levels or RF inhomogeneities of SBMR images. The SBMR images were more difficult to be correctly segmented; therefore the BDT combined with preprocessing by MSR algorithm for correcting intensity inhomogeneity was proposed. The accuracy rates obtained from brain tissue segmentation with spatial feature  $(G, x, y, r, \theta)$  were slightly higher than those of segmentation with spatial feature  $(S, x, y, r, \theta)$  because the general gray level ( $G$ ) had less overlap in intensity distribution for each tissue than that of spatial gray level ( $S$ ). The accuracy rates of segmentation through preprocessing by MSR were not greatly decreasing when the noise levels, combined with 20% or 40% RF inhomogeneities, were increased (Figure 5.4, Figure 5.5). There was also no significant difference of accuracy rate of segmentation of SBMR images with 20% or 40% inhomogeneity since the overlap in intensity distribution was less affected by inhomogeneities (Figure 5.4, Figure 5.5). Compared with the results of several studies [42, 43, 48, 53, 94], the importance of improving brain tissue segmentation accuracy is increasing in MR images, the segmentation errors of brain tissue from MR images were

much more decreased when the BDT is combined with preprocessing by MSR algorithm. In considering the time-consuming, the processing time of segmentation by using CART is very less than that of by using BDT from SBMR images. The CART is the better for little processing time of segmentation and the BDT is better for higher accuracy of segmentation.

In conclusion, the highest accuracy rates of brain tissue segmentation were obtained when the spatial features  $(G, x, y, r, \theta)$  and  $(S, x, y, r, \theta)$  were used to classify the SBMR images and when the BDT is combined with preprocessing by MSR algorithm. Both of the processes greatly improve the accuracy rates of brain tissue segmentation from SBMR images to achieve high quality of segmentation.





## Chapter 6 The Summary and Future Works

In this dissertation, we presented a multiscale retinex (MSR) algorithm to successfully correct the intensity inhomogeneity of brain MR images to obtain clearer deep brain structures and better image quality. The performance of intensity inhomogeneity correction was also evaluated by PSNR and CNR. Next, we proposed two decision trees (CART and BDT) with a supervised method and an automatic segmentation to successfully achieve the brain tissue segmentation on brain MR images to obtain better brain structures for neuroanatomical applications. The results of segmentation were also evaluated with two more indexes (accuracy rate,  $k$  index, and other published indexes). Finally, we achieved the high quality of segmentation with greatly improved accuracy based on BDT through preprocessing by the MSR algorithm from SBMR images. The experimental results of a number of simulated and *in vivo* MR data demonstrate that the proposed methods are valuable for brain MR image segmentation in neurological applications.

Although the experimental results are very promising, some aspects are needed to be addressed for further improving the performance and other applications.

- 1) The retinex algorithm could also be used to increase the SNR and dynamic-range compression in other types of medical image, such as those captured by computerized tomography (CT), digital X-ray systems, and digital mammography.
- 2) These algorithms can be also applied to process the images of other organs such as abdomen, chest, and also T2-weight, or PD-weighted MR images.
- 3) The method used in this research, together with 3D reconstruction method, might be applied for the tissue volume measurements of brain MR image to improve the diagnosis in clinical application. It is worth further studies.
- 4) A more sophisticated method for a group of experts to construct gold-standard image, which might improve the accuracy of segmentation is also an interest research

category.

- 5) Owing to the complex of brain edge on MR images, the background removing research and more tissue classes of brain MR image are worth studying issues.



## References

- [1] F. Bloch, "Nuclear induction," *Phys Rev*, vol. 70, pp. 460–474, 1946.
- [2] F. Bloch, W. W. Hansen, and M. Packard, "The nuclear induction experiment," *Phys Rev*, vol. 70, pp. 474–485, 1946.
- [3] F. Bloch, W. W. Hansen, and M. Packard, "Nuclear induction," *Phys Rev*, vol. 69, pp. 127–127, 1946.
- [4] E. M. Purcell, H. C. Torrey, and R. V. Pound, "Resonance absorption by nuclear magnetic moments in a solid," *Phys Rev*, vol. 69, pp. 37–38, 1946.
- [5] R. R. Edelman, et al., "Surface coil MR imaging of abdominal viscera. Part 1: theory, technique, and initial results," *Radiology*, vol. 157, pp. 425–430, 1985.
- [6] E. B. Boskamp, "Improved surface coil imaging in MR: decoupling of the excitation and receiver coils," *Radiology*, vol. 157, pp. 449–452, 1985.
- [7] Z. Cho, J. P. Jones and M. Singh, *Foundations of medical imaging*, New York: John Wiley and Sons, 1993.
- [8] M. L. Wood, M. J. Shivji and P. L. Stanchev, "Planar motion correction with use of k-space data acquired in Fourier MR imaging," *J Magn Reson Imaging*, vol. 5, pp. 57–64, 1995.
- [9] R. A. Zoroofi, Y. Sato, S. Tamura, H. Naito and L. Tang. "An improved L method for MRI artifact correction due to translational motion in the imaging plane," *IEEE Trans Med Imag*, vol. 14, pp. 471–479, 1995.
- [10] E. A. Vokurka, N. A. Watson, Y. Watson, NA Thacker and A. Jackson, "Improved high resolution MR imaging for surface coils using automated intensity non-uniformity correction: feasibility study in the Orbit," *J Magn Reson Imaging*, vol. 14, pp. 540–546, 2001.
- [11] C. Haiguang, H. Avram, L. Kaufman, J. Hale, and D. Kramer, "T2 restoration and noise

suppression of hybrid MR images using Wiener and linear prediction techniques,” *IEEE Trans Med Imag*, vol. 13, pp. 667–676, 1994.

- [12] H. S. Zadeh, J. P. Windham, D. J. Peck, and A. E. Yagle, “A comparative analysis of several transforms for enhancement and segmentation of magnetic resonance image scene sequences,” *IEEE Trans Med Imag*, vol. 11, pp.302–318, 1992.
- [13] J. G. Sled, A. P. Zijdenbos, and A. C. Evans, “A nonparametric method for automatic correction of intensity nonuniformity in MRI data,” *IEEE Trans Med Imag*, vol. 17, pp. 87–97, 1998.
- [14] C. B. Ahn, Y. C. Song and D. J. Park, “Adaptive template filtering for signal-to-noise ratio enhancement in magnetic resonance imaging,” *IEEE Trans Med Imag*, vol. 18, pp. 549–556, 1999.
- [15] M. Styner, C. Brechbuhler, G. Szekely, and G. Gerig, “Parametric estimate of intensity inhomogeneities applied to MRI,” *IEEE Trans Med Imag*, vol. 19, pp. 153–165, 2000.
- [16] B. Likar, M. A. Viergever and F. Pernus, “Restrospective correction of MR intensity inhomogeneity by information minimization,” *IEEE Trans Med Imag*, vol. 20, pp. 1398–1410, 2001.
- [17] F. H. Lin, Y. J. Chen, J. W. Belliveau and L. L. Wald, “A wavelet-based approximation of surface coil sensitivity profile for correction of image intensity inhomogeneity and parallel imaging reconstruction,” *Human Brain Mapp*, vol. 19, pp.96–111, 2003.
- [18] C. Han, T. S. Hatsukami and C. Yuan, “A multi-scale method for automatic correction of intensity non-uniformity in MR images,” *J Magn Reson Imaging*, vol. 13, pp.428–436, 2001.
- [19] Z. Hou, “A review on MR image intensity inhomogeneity correction,” *International Journal of Biomedical Imaging*, vol. 2006, pp. 1–11, 2006
- [20] J. Luo, Y. Zhu, P. Clarysse, and I. Magnin, “Correction of bias field in MR images using singularity function analysis,” *IEEE Trans Med Imag*, vol. 24, pp. 1067–1085, 2005.

- [21] M. Julien and Z. Yue-Min, "Model-based intensity nonuniformity correction in brain MRI," *Proceedings ICSP '04. 2004 7th International Conference on Signal Processing*, vol. 2, pp. 982–985, 2004.
- [22] O. Salvado, C. Hillenbrand, and D. L. Wilson, "Correction of intensity inhomogeneity in MR images of vascular disease," *Proceedings of the 2005 IEEE Engineering in Medicine and Biology 27th Annual International Conference*, pp. 4302–4305, Sep. 2005.
- [23] O. Salvado, C. Hillenbrand, Z. Shaoxiang, and D. L. Wilson, "Method to correct intensity inhomogeneity in MR images for atherosclerosis characterization," *IEEE Transactions on Medical Imaging*, vol. 25, pp. 539–552, 2006.
- [24] K. Van Leemput, F. Maes, D. Vandermeulen, and P. Suetens, "Automated model-based bias field correction of MR images of the brain," *IEEE Trans Med Imag*, vol. 18, pp. 885–896, 1999.
- [25] P. Maji, S. Dasgupta, B. Chanda, and M. K. Kundu, "Deformation correction in brain MRI using mutual information and genetic algorithm," *Proceedings of International Conference on Computing: Theory and Applications (ICCTA'07)* pp. 372–376, 2007.
- [26] R. A. Zoroofi, T. Nishii, Y. Sato, N. Sugano, H. Yoshikawa, and S. Tamura, "Segmentation of a vascular necrosis of the femoral head using 3D MR images," *Comput Med Imaging Graph*, vol. 25, pp. 511–521, 2001
- [27] R. A. Zoroofi, Y. Sato, T. Nishii, N. Sugano, H. Yoshikawa, and S. Tamura, "Automated segmentation of necrotic femoral head from 3D MR data," *Comput Med Imaging Graph*, vol. 28, pp. 267–278, 2004.
- [28] J. Liu, J. K. Udupa, D. Odhner, D. Hacney, and G. Moonis "A system for brain tumor volume estimation via MR imaging and fuzzy connectedness," *Comput Med Imaging Graph*, vol. 29, pp. 21–34, 2005.
- [29] S. Behrens, H. Laue, M. Althias, T. Boehler, B. Kuemmerlan, H. K. Hahn, and H. O.

- Peitgen, "Computer assistance for MR based diagnosis of breast cancer: present and future challenges," *Comput Med Imaging Graph*, vol. 31, pp. 236–247, 2007.
- [30] H. E. Cline, C. L. Doumulin, H. R. Hart, W. E. Lorensen, and S. Ludke, "3-D reconstruction of the brain from magnetic resonance images using a connectivity algorithm," *Magn Reson Imaging*, vol. 5, pp. 345–352, 1987.
- [31] M. Joliot, and B. M. Majoyer, "Three dimensional segmentation and interpolation of magnetic resonance brain images," *IEEE Trans Med Imag*; vol. 12, pp. 269–277, 1993.
- [32] T. Schiemann, U. Tiede, and K. H. Hohne, "Segmentation of visible human for high quality volume-based visualization," *Med Imag Anal*, vol. 1, pp. 263–270, 1996.
- [33] Z. Y. Shan, Q. Ji, A. Gajjar, and E. Reddick, "A knowledge-guided active contour method of segmentation of cerebella on MR images of pediatric patients with medulloblastoma," *Magn Reson Imaging*, vol. 21, pp. 1–11, 2005.
- [34] A. H. Andersen, Z. Zhang, M. J. Avison, and D. M. Gash, "Automated segmentation of multispectral brain MR images," *J Neurosci Methods* vol. 122, pp. 13–23, 2002.
- [35] U. Amato, M. Larobina, A. Antoniadis, and B. Alfano, "Segmentation of magnetic resonance brain images through discriminant analysis," *J Neurosci Methods*, vol. 131, pp. 65–74, 2003.
- [36] A. A. Ali, A. M. Dale, A. Badaea, and G. A. Johnson, "Automatic segmentation of neuroanatomical structures in multispectral MR microscopy of the mouse brain," *NeuroImage*, vol. 27, pp. 425–435, 2005.
- [37] J. Mohr, A. Hess, M. Scholz, and K. Obermayer, "A method for automatic segmentation of autoradiographic image stacks and spatial normalization of functional cortical activity patterns," *J Neurosci Methods*, vol. 134, pp. 45–58, 2004.
- [38] J. Sharma, M. P. Sanfilippo, R. H. B. Benedict, B. Weinstock-Guttman, F. E. Munschauer, and R. Bakshi, "Whole-brain atrophy in multiple sclerosis measured by automated

versus semiautomated MR imaging segmentation,” *Am J Neuroradiol*, vol. 25, pp. 985–996, 2004.

- [39] F. Admiraal-Behloul, D. M. J. Van Den Heuvel, O. M. J. P. Van Osch, J. Van Der Grond, M. A. Van Buchem, and J. H. C. Reiber, “Fully automatic segmentation of white matter hyperintensities in MR images of the elderly,” *NeuroImage*, vol. 28, pp. 607–617, 2005.
- [40] M. Prastawa, J. H. Gilmore, W. Lin, and G. Gerig, “Automatic segmentation of MR images of the developing newborn brain,” *Med Imag Analysis*, vol. 9, pp. 457–466, 2005.
- [41] Y. Xia, K. Bettinger, L. Shen, and A. Reiss, “Automatic segmentation of the caudate nucleus from human brain MR images,” *IEEE Trans Med Imag*, vol. 26, pp. 509–517, 2007.
- [42] J. L. Marroquin, B. C. Vemuri, S. Botello, F. Calderon, and A. Fernandez-Bouzas, “An accurate and efficient Bayesian method for automatic segmentation of brain MRI,” *IEEE Trans Med Imag*, vol. 21, pp. 934–945, 2002.
- [43] H. Greenspan, A. Ruf, and J. Goldberger, “Constrained Gaussian mixture model framework for automatic segmentation of MR brain images,” *IEEE Trans Med Imag*, vol. 25, pp. 1233–1245, 2006.
- [44] P. Anbeek, K. L. Vincken, M. J. P. Van Osch, R. H. C. Bisschops, and J. Van Der Grond, “Probabilistic segmentation of white matter lesions in MR imaging,” *NeuroImage*, vol. 21, pp. 1037–1044, 2004.
- [45] W. B. Dou, S. Ruan, Y. P. Chen, D. Bloyet, and J. M. Constans, “A framework of fuzzy information fusion for the segmentation of brain tumor tissues on MR images,” *Image and Vision Computing*, vol. 25, pp. 164–171, 2007.
- [46] L. Q. Zhou, Y. M. Zhu, C. Bergot, A. M. Laval-Jeantet, V. Bousson, and J. D. Laredo, “A method of radio-frequency inhomogeneity for brain tissue segmentation in MRI,” *Comput Med Imaging Graph*, vol. 25, pp. 379–789, 2001.

- [47] Y. Gu, L. O. Hall, D. Goldgof, P. M. Kanade, and F. R. Murtagh, "Sequence tolerant segmentation system of brain MRI," *Proceedings of the IEEE International Conference on System, Man and Cybernetics*, Hawaii October 10-12, 2005.
- [48] P. Anbeek, K. L. Vincken, G. S. Van Bochove, M. J. P. Van Osch, R. H. C. Bisschops, and J. Van Der Grond, "Probabilistic segmentation of brain tissue in MR imaging," *NeuroImage*, vol. 27, pp. 795–804, 2005.
- [49] V. Barra, and J-Y. Boire, "Tissue segmentation on MR images of the brain by possibilistic clustering on a 3D wavelet representation," *J Magn Reson Imaging*, vol. 11, pp. 267–278, 2000.
- [50] Z. Xue, D. Shen, and C. Davatzikos, "Determining correspondence in 3-D MR brain images using attribute vectors as morphological signatures of voxels," *IEEE Trans Med Imag*, vol. 23, pp. 1276–1291, 2004.
- [51] H. Tang, E. X. Wu, Y. O. Ma, D. Gallagher, G. M. Perera, and T. Zhuang, "MRI brain image segmentation by multi-resolution edge detection and region selection," *Comput Med Imaging Graph*, vol. 24, pp. 349–357, 2000.
- [52] S-S. Yoo, C-U. Lee, B. G. Choi, and P. Saiviroonporn, "Interactive 3-dimensional segmentation of MRI data in personal computer environment," *J Neurosci Methods*, vol. 112, pp. 75–82, 2001.
- [53] R. Archibald, K. Chen, A. Gelb, and R. Renaut, "Improving tissue segmentation of human brain MRI through preprocessing by the Gegenbauer reconstruction method," *NeuroImage*, vol. 20, pp. 489–502, 2003.
- [54] P. Andrey, and Y. Maurin, "Free-D: an integrated environment for three-dimensional reconstruction from serial sections," *J Neurosci Methods*, vol. 145, pp. 233–244, 2005.
- [55] R. He, B. R. Sajja, and P. A. Narayana, "Implementation of high-dimensional feature map for segmentation of MR images," *Annals Biomed Eng*, vol. 33, pp. 1439–148, 2005.



- [56] M. Noulhiane, S. Samson, S. Clemenceau, D. Dormont, B. Baulac, and D. Hasboun, "A volumetric MRI study of the hippocampus and the parahippocampal region after unilateral medial temporal lobe resection," *J Neurosci Methods*, vol. 156, pp. 293–304, 2006.
- [57] R. B. Lufkin, et al., "Dynamic-range compression in surface-coil MRI," *Am J Nueroradiol*, vol. 147, pp. 379–382, 1986.
- [58] R. B. Lufkin, *The MRI manual*, California: Mosby, Inc., 1998.
- [59] B. H. Suits, and A. N. Garroway, "Optimizing surface coils and the self-shielded gradiometer," *J Appl Phys* vol. 94, pp. 4170–4178, 2003.
- [60] D. Gensanne, G. Josse, J. M. Lagarde, and D. Vincensini, "High spatial resolution quantitative MR images: an experimental study of dedicated surface coils," *Phys Med Biol*; vol. 51, pp. 2843–2855, 2006.
- [61] D. T. Chard, G. J. M. Parker, C. M. B. Griffin, A. J. Thompson, and D. H. Miller, "The reproducibility and sensitivity of brain tissue volume measurements derived from an SPM-based segmentation methodology," *J Magn Reson Imaging*, vol. 15, pp. 259–267, 2002.
- [62] W. Shufeng, Y. Wenhui, and H. Lili, "A background removing method of MR images and its application in the intensity nonuniformity correction methods," *Proceedings of 2008 International Conference on Technology and Applications in Biomedicine( ITAB 2008)*, pp. 175–178, 2008.
- [63] W. Chen and M. L. Giger, "A fuzzy c-means (FCM) based algorithm for intensity inhomogeneity correction and segmentation of MR images," *Proceedings of 2004 IEEE International Symposium on Biomedical Imaging*, vol. 2, pp. 1307–1310, 2004.
- [64] L. Pan, Y. Yong, Z. Chong-Xun, and G. Jian-Wen, "An efficient automatic framework for segmentation of MRI brain image," *Proceedings of the Fourth International Conference on Computer and Information Technology (CIT '04)*, pp. 896–900, 2004.

- [65] X. Li and S. Luo, "Bias field correction-based tissue classification of MR images of brain," *Proceedings of 1998 Fourth International Conference on Signal Processing Proceedings ( ICSP '98)*, vol.2, pp. 948–950, 1998.
- [66] B. M. Dawant, A. P. Zijdenbos, and R. A. Margolin, "Correction of intensity variations in MR images for computer-aided tissue classification," *IEEE Trans Med Imag*, vol. 12, pp. 770–781, 1993.
- [67] B. Johnston, B. Johnston, M. S. Atkins, B. Mackiewicz, and M. A. A. M. Anderson, "Segmentation of multiple sclerosis lesions in intensity corrected multispectral MRI," *IEEE Transactions on Medical Imaging*, vol. 15, pp. 154–169, 1996.
- [68] R. Guillemaud, "Uniformity correction with homomorphic filtering on region of interest," *Proceedings of 1998 International Conference on Image Processing ( ICIP 98)*, vol. 2, pp. 872–875, 1998.
- [69] R. C. Gonzalez, and R. E. Woods, *Digital image processing*, 2nd ed., New Jersey: Prentice Hall, Inc., 2002.
- [70] S. D. Chen, and A. R. Ramli, "Preserving brightness in histogram equalization based contrast enhancement techniques," *Digit Sig Proc*, vol. 14, pp. 413–428, 2004.
- [71] V. Caselles, J. L. Lisani, J. M. Morel and G. Sapiro, "Shape preserving local histogram modification," *IEEE Trans Imag Proc*, vol. 8, pp. 220–230, 1999.
- [72] H. D. Cheng, and X. J. Shi, "A simple and effective histogram equalization approach to image enhancement," *Digit Sig Proc*, vol. 14, pp. 158–170, 2004
- [73] Y. Sun, and D. Parker, "Small vessel enhancement in MRA images using local maximum mean processing," *IEEE Trans Imag Proc*, vol. 10, pp. 1687–1699, 2001.
- [74] J. Y. Kim, L. S. Kim, and S. H. Hwang, "An advanced contrast enhancement using partially overlapped sub-block histogram equalization," *IEEE Trans Cir & Sys for Video Tech*, vol. 11, pp. 475–484, 2001.

- [75] J. Tang, E. Peli and S Acton, "Image enhancement using a contrast measure in compressed domain," *IEEE Sig Proc Letters*, vol. 10, pp. 289–292, 2003.
- [76] M. Eramian, and D. Mould. "Histogram equalization using neighborhood metrics," *Proceedings of the 2nd Canadian Conference on Computer and Robot Vision*, pp. 397–404, 2005.
- [77] E. Land, "An alternative technique for the computation of the designator in the retinex theory of color vision," *Proc Natl Acad Sci U S A.*, vol. 83, pp. 3078–3080, 1986.
- [78] A. Moore, J. Allman, and R. M. Goodman, "A real-time neural system for color constancy," *IEEE Trans Neural Networks*, vol. 2, pp. 237–247, 1991.
- [79] A. Moore, G. Fox, J. Allman and R. M. Goodman, "A VLSI neural network for color constancy," in *Advances in Neural Information Processing 3*". D. S. Touretzky, R. Lippman and E. S. Mateo, CA: Morgan Kaufmann, pp. 370–376, 1991.
- [80] A. C. Hurlbert, and T. Poggio, "Synthesizing a color algorithm from examples," *Science*, vol. 239, pp. 482–485, 1988.
- [81] A. C. Hurlbert, *The computation of color*, PhD dissertation, Mass. Inst. Technol., Cambridge, MA, 1989.
- [82] D. J. Jobson, Z. Rahman and G. A. Woodell, "Properties and performance of a center/surround retinex," *IEEE Trans Imag Proc*, vol. 6, pp. 451–462, 1997.
- [83] B. R. Conway, and M. S. Livingstone, "Spatial and temporal properties of cone signals in alert macaque primary visual cortex," *J Neuroscience*, vol. 26, pp. 10826–10846, 2006.
- [84] B. R. Conway, "Spatial structure of cone inputs to color cells in alert macaque primary visual cortex," *J Neuroscience*, vol. 21, pp. 2768–2783, 2001.
- [85] D. J. Jobson, Z. Rahman and G. A. Woodell, "A multiscale retinex for bridging the gap between color images and the human observation of scenes," *IEEE Trans Imag Proc*, vol. 6, pp. 965–976, 1997.

- [86] D. E. Bowker, R. E. Davis, D. L. Myrick, K. Stacy and W. L. Jones, "Spectral reflectances of natural targets for use in remote sensing studies," *NASA Ref Pub*, 1985.
- [87] D. H. Brainard, and B. A. Wandell, "An analysis of the retinex theory of color vision," *J Opt Soc Amer A*, vol. 3, pp. 1651–1661, 1986.
- [88] G. W. Wei, "Generalized perona malik-equation for image restoration," *IEEE Sig Proc Letters*, vol. 6, pp. 165–167, 1999.
- [89] K. A. Grajski, L. Breiman, G. V. Di Prisco, and W. J. Freeman, "Classification of EEG spatial patterns with a tree structured methodology: CART," *IEEE Trans Biomed Eng*, vol. BME-33, pp. 1076–86, 1986.
- [90] H. R. Bittencourt, and R. T. Clarke, "Use of classification and regression trees (CART) to classify remotely-sensed digital images," *Proceedings of the IEEE International Geoscience and Remote Sensing Symposium IGARSS '03*, vol. 6, pp. 3751–3753, 2003.
- [91] L. Breiman, J. H. Friedman, R. A. Olshen, and C. J. Stone, *Classification and regression trees*, CA: Wadsworth International, 1984.
- [92] R. O. Duda, P. E. Hart, and D. G. Stork, *Pattern Classification*, New York: Wiley, 2001.
- [93] B. Wang, P. K. Saha, J. K. Udupa, M. A. Ferrante, J. Baumgardner, D. A. Roberts, and R. R. Rizi, "3D airway segmentation via hyperpolarized  $^3\text{He}$  gas MRI by using scale-based fuzzy connectedness," *Comput Med Imaging Graph*, vol.28, pp. 77–86, 2004.
- [94] Z. Q. Yu, Y. Zhu, J. Yang, and Y. M. Zhu, "A hybrid region-boundary model for cerebral cortical segmentation in MRI," *Comput Med Imaging Graph*, vol. 30, pp. 197–208, 2006.
- [95] S. K. Warfield, K. H. Zou, and W. M. Wells, "Validation of image segmentation and expert quality with an expectation-maximization algorithm," *Proceeding of MICCAI, of lecture notes in computer science*, vol. 2488, pp. 298–306, 2002.

- [96] S. Hautaniemi, S. Kharait, A. Iwabu, A. Wells, and D. A. Lauffenburger, "Modeling of signal-response cascades using decision tree analysis," *Bioinformatics*, vol. pp. 2027–2035, 2005.
- [97] J. R. Quinlan, "Induction of decision tree," *Machine Learning*, vol. 1, pp. 81–106, 1986.
- [98] J. R. Quinlan, *C4.5: programs for machine learning*, San Mateo, CA: Morgan Kaufmann, 1993.
- [99] J. R. Quinlan, "Improved use of continuous attributes in C4.5," *Journal of Artificial Intelligence Research*, vol. 4, pp.77–90, 1996.
- [100] J. R. Quinlan, *Data mining tools See5 and C5.0*, Austria: RuleQuest Research, <http://www.rulequest.com/see5-info.html>. 2003.
- [101] Y. R. Shiue, and R. S. Guh, "The optimization of attribute selection in decision tree-based production control systems," *Int J Adv Manuf Technol*, vol. 28, pp. 737–746, 2006.
- [102] J. Macek, "Incremental learning of ensemble classifiers on ECG data," *Proceedings of the 18<sup>th</sup> IEEE Symposium on Computer-Based Medical System (CBMS'05)*, 2005.
- [103] J. Dombi, and A. Zsiros, "Learning multicriteria classification models from examples: decision rules in continuous space," *Eur J Oper Res*, vol. 160, pp. 663–675, 2005.
- [104] L. Frey, and D. Fisher, "Identifying Markov blankets with decision tree induction," *Proceeding of the Third IEEE International Conference on Data Mining*, pp. 59–66, 2003.
- [105] J. Ranilla, O. Luaces, and A. Bahamonde, "A heuristic for learning decision trees and pruning them into classification rules," *AI Communications*, vol. 16, pp. 71–87, 2003.
- [106] W. Hu, O. Wu O, Z. Chen, Z. Fu, and S. Maybank, "Recognition of pornographic web pages by classifying texts and images," *IEEE Trans Pattern Analysis and Machine Intelligence*, vol. 29 pp. 1019–1034, 2007.

- [107] Y. Freund, and R. E. Schapire, “Experiments with a new boosting algorithm,” *Proceeding of the 13<sup>th</sup> international conference on Artificial Intelligence: Machine Learning. International Machine Learning Society*, Bari, Italy, pp. 148–156, 1996.
- [108] Y. Freund, and R. E. Schapire, “A short introduction to boosting,” *J Jpn Soc Artif Intell*, vol. 14, pp. 148–156, 1999.
- [109] D. Arditi, and T. Pulket, “Predicting the outcome of construction litigation using boosted decision trees,” *J Comp in Civ Engrg*, vol. 19, pp. 387–393, 2005.
- [110] K. Kirchner, K. H. Tölle, and J. Krieter, “Optimization of the decision tree technique applied to simulated sow herd datasets,” *Comput Electron Agric*, vol. 50, pp. 15–24, 2006.
- [111] K. Diem, et al., *Documenta Geigy Scientific Tables*, Geigy Pharmaceuticals, 1962.
- [112] D. Stalling, M. Westerhoff, and H. C. Hege, *Amira - an object oriented system for visual data analysis*, In C. R. Johnson & C. D. Hansen (Eds.), *Visualization Handbook: Academic Press*, 2005.
- [113] L. R. Dice, “Measures of the amount of ecologic association between species,” *Ecology*, vol. 26, pp. 297–302, 1945.
- [114] I. Wolf, M. Vetter, I. Wegner, T. Böttger, M. Nolden, M. Schöbinger, et al., “The medical imaging interaction toolkit,” *Medical Image Analysis*, vol. 9, pp. 594–604, 2005.
- [115] W. M. Wells, W. E. L. Grimson, R. Kikinis, and F. A. Jolesz, “Adaptive segmentation of MRI data,” *IEEE Trans. Medical Imaging*, vol. 15, pp.429–442, 1996.

## Curriculum Vitae

ID No.	L120443672	Renewed Date: 2008/08/28		
Chinese Name	趙文鴻	English Name	Chao, Wen-Hung	
			(Last Name)	(First Name)
Nationality	Republic of China	Gender	Male	Birth Date Sep. 30, 1966
Address	No. 306, Yuanpei St., Hsinchu, Taiwan 300, R.O.C.			
Tel. No.	(Office) 886-3-5381183 ext 8626		(Home) 886-3-5619435	
Fax No.	886-3-6102347	Email	wenhong@mail.ypu.edu.tw	
Education				
University	Nation	Major	Degree	Period(Y/M)
National Cheng Kung University	Taiwan, R. O. C.	Biomedical	M. S.	From 1994/09 to 1996/06
National Chiao Tung University	Taiwan, R. O. C.	Electrical & Control	Ph.D.	From 2002/09 to 2008/-
Licence				
Biomedical Engineer, Biomedical Engineering Society of the R. O. C.				
Experience				
From 1990/08 to 1992/11	R&D Engineer, Truth Instruments Co., Ltd.			
From 1992/06 to 1993/09	R&D Engineer, Genemax Medical Products Industry Corp.			
From 1996/08 to 2008/-	Lecturer, Department of Biomedical Engineering, Yuanpei University			
Publications				
International Journal				
1. <u>Wen-Hung Chao</u> , Chien-Wen Cho, Yen-Yu Shih, You-Yin Chen, Chen Chang, “Correction of inhomogeneous MR images using multiscale retinex,” <i>International of Image Processing</i> , vol. 1, pp. 1–16, 2007.				

2. Chien-Wen Cho, Wen-Hung Chao, You-Yin Chen, "A linear-discriminant-analysis-based approach to enhance the performance of fuzzy c-means clustering in spike sorting with low-SNR data," *International Journal of Biometric and Bioinformatics*, vol. 1, pp. 1–13, 2007.
3. Wen-Hung Chao, Chien-Wen Cho, Yen-Yu I Shih, Sheng-Huang Lin, You-Yin Chen, "Improving segmentation accuracy for magnetic resonance imaging using a boosted decision tree," *Journal of Neuroscience Methods* (Accepted)
4. Wen-Hung Chao, Chien-Wen Cho, Sheng-Huang Lin, You-Yin Chen, "A vision-based analysis system for gait recognition in patients with parkinson's disease," *Expert Systems With Applications*. (Accepted)
5. Wen-Hung Chao, Chien-Wen Cho, Yen-Yu I. Shih, You-Yin Chen, "Automatic segmentation of magnetic resonance image using decision tree with spatial information," *Computerized Medical Imaging and Graphics*. (Revised)
6. You-Yin Chen, Hsin-Yi Lai, Sheng-Huang Lin, Wen-Hung Chao, Chia-Hsin Liao, Siny Tsang, "Design and fabrication of polyimide-based microelectrode array: application in neural recording and repeatable electrolytic lesion in rat brain," *Journal of Neuroscience Methods*. (Revised)

#### Conference

1. Shing-Hong Liu, Chin-Teng Lin, and Wen-Hung Chao, "The short-time fractal scaling of heart rate variability to estimate the mental stress of driver," *The Proceedings of 2004 IEEE ICNSC International conference*, Taipei, Taiwan, pp. 829-833, Mar 2004.
2. Sheng-Fu Liang, Chin-Teng Lin, Ruei-Cheng Wu, Teng-Yi Huang, and Wen-Hung Chao, "Classification of driver's cognitive responses from EEG analysis," *The Proceedings of 2005 IEEE International Symposium on Circuits and Systems*, Kobe, Japan, pp.156-159, May 2005.
3. Chin-Teng Lin, Wen-Hung Chao, and, Sheng-Fu Liang "A single-trial event-related potential-based fuzzy neural network for the recognition of driver's cognitive response," *The Proceedings of The 12th International Conference on Neural Information*, Taipei, Taiwan, pp. 253-258, Oct 2005.
4. Chin-Teng Lin, Wen-Hung Chao, Yu-Chieh Chen, and Sheng-Fu Liang, "Adaptive feature extractions in an EEG-based alertness estimation system," *The Proceedings IEEE SMC 2005 Conference*, Hawaii, U. S. A., pp. 2096-2101, Oct 2005.
5. Chang Shen Hsien, Wen-Hung Chao, Chien-Wen Cho, You Yin Chen, "The development of electroencephalogram measurement and display system," *The*



*Proceedings of 2006 International Symposium on Biomedical Engineering (2006 ISOBME)*, Taipei, Taiwan, R. O. C., pp. 126-126, Dec 2006.

6. Wen-Hung Chao, Wang-Lung Wu, Mei-Hua Liao, “A simple electroencephalogram real-time display system,” *The Proceedings of 2007 Conference on Health and Management*, Yuanpei University, Hsinchu, Taiwan, pp. 66, Nov 2007.
7. Wen-Hung Chao, Pei-Tsz Chen, Hsiang-Jui Huang, Sih-Yi Kuo, Yi-Chen Li, “Designing an electromyogram real-time display system,” *The Proceedings of 2007 Conference on Health and Management*, Yuanpei University, Hsinchu, Taiwan, pp.67, Nov 2007.
8. Hsuo-Jen Hsu, Shih-Wei Chen, Hsin-Hsien Wu, Wan-Ya Chen, You-Yin Chen, Wen-Hung Chao, “ZigBee-based wireless sensor network for real-time transmission of wavelet compression of ECG signals from multiple users,” *The Proceedings of 2007 Annual Symposium on Biomedical Engineering and Technology*, Taichung, Taiwan, pp. 65, Dec 2007.
9. May-Hua Liao, Shin-Yi Cheng, Ming-Li Liou, Wen-Hung Chao, Hsiao-Hung Pu, “The effectiveness of percussion stimulation on preventing skeletal muscle degeneration,” *The Proceedings of 2007 Annual Symposium on Biomedical Engineering and Technology*, Taichung, Taiwan, pp. 154, Dec 2007.